

**Towards pesticide identification in open fields by
Surface-enhanced Raman spectroscopy:
A preparative, spectroscopic, and quantum
chemical route**

Dissertation

zur Erlangung des akademischen Grades
Doktor der Naturwissenschaften
– Dr. rer. nat. –

vorgelegt von
Andrea Hermsen
geboren in
Düsseldorf

am Institut für Physikalische Chemie
der Universität Duisburg-Essen

2024

DuEPublico

Duisburg-Essen Publications online

UNIVERSITÄT
DUISBURG
ESSEN

Offen im Denken

ub | universitäts
bibliothek

Diese Dissertation wird via DuEPublico, dem Dokumenten- und Publikationsserver der Universität Duisburg-Essen, zur Verfügung gestellt und liegt auch als Print-Version vor.

DOI: 10.17185/duepublico/82768

URN: urn:nbn:de:hbz:465-20241217-124113-5

Alle Rechte vorbehalten.

Die vorliegende Arbeit wurde als kooperative Promotion der Universität Duisburg-Essen und der Hochschule Niederrhein im Zeitraum von September 2017 bis Februar 2022 im Arbeitskreis von Herrn Prof. Dr. Martin Jäger, Fachbereich Chemie der Hochschule Niederrhein, in Zusammenarbeit mit Herrn Prof. Dr. Christian Mayer, Institut für Physikalische Chemie der Universität Duisburg-Essen, durchgeführt.

Tag der Disputation: 10.12.2024

Gutachter: Prof. Dr. Christian Mayer
Prof. Dr. Martin Jäger

Vorsitzende: PD Dr. Ursula Telgheder

Kurzfassung

Pestizide werden weltweit in der Landwirtschaft eingesetzt. Aufgrund ihres gefährlichen Potenzials wird der Einsatz von Pestiziden überwacht. Eine Methode die als analytische Methode eingesetzt wird ist die Surface-Enhanced Raman Spektroskopie (SERS). Die SERS Technik basiert auf einer Verstärkung des Ramansignals durch elektrische Felder, welche durch Nanopartikel hervorgerufen werden. Das hervorgerufene SERS Signal ist dabei um mehrere Größenordnungen intensiver als ein Raman Signal, dies ermöglicht auch einen Nachweis im Spurenbereich. Zur Identifizierung der Pestizide Imidacloprid, Thiram und Paraquat wurden unterschiedliche SERS-Methoden entwickelt, welche mit portablen Raman-Spektrometern angewendet werden.

Zunächst wurde eine Methode entwickelt bei der Imidacoprid direkt auf dem Feld mit einem Raman-Handheld Spektrometer nachgewiesen werden kann. Dabei wurden verschiedene Agglomerationsmittel untersucht, unter anderem Salzsäure sowie diverse Salze, um durch Agglomeration das SERS-Signal zu erhöhen. Es zeigte sich im Rahmen der Untersuchungen, dass Salzsäure deutlich besser als die Salze zur Agglomeration geeignet ist und auch eine bessere Verstärkung des SERS-Signals hervorruft. Ebenso wurden untersucht ob sich Filterpapier und Polylactid -Gewebe als SERS-Substrat Grundlagen eignen. Dabei zeigte sich, dass Polylactid aufgrund seiner hydrophoben Wirkung besser als SERS-Substrat Grundlage geeignet ist. Desweiteren wurde noch eine Modellrechnungen durchgeführt, welche zeigt, dass es zu potenziellen Pestizidrückständen von etwa 300 mg/kg in landwirtschaftlich genutzten Böden kommen kann.

In einer weiterführenden Studie wurden der Aspekt der SERS-Substrat Grundlage erneut aufgegriffen und Polylactid- und Polyethylenterephthalat/Polyamid-Textilien als Trägermaterialien für die SERS-Substrate untersucht, wobei sich Polyethylenterephthalat/Polyamid als am geeignetsten erwiesen hat. Im Rahmen dieser Studie wurden die Methode auf die Pestizide Thiram und Paraquat erweitert. Es konnten Nachweisgrenzen ermittelt werden die im Nano- bis Pikogrammbereich liegen. Durch den Vergleich mit der Modellrechnung aus der ersten Studie zeigte sich, dass die Nachweisgrenzen somit in einem relevanten Bereich liegen, nämlich unterhalb der ausgebrachten Menge, wodurch auch Pestizidrückstände nachgewiesen werden können.

In einer weiteren Studie wurde die entwickelte Methode auf Silbernanopartikel als aktive SERS-Substrate ausgeweitet und hinsichtlich ihrer unterschiedlichen Verstärkung im Vergleich zu Goldnanopartikeln untersucht. Dabei hat sich gezeigt, dass Thiram bei Gold- und Silbernanopartikeln gleich verstärkt wird und ähnliche SERS-Spektren liefert. Paraquat hingegen ruft unterschiedliche SERS-Spektren mit Gold- und Silbernanopartikeln hervor. Dies lässt eine unterschiedliche Orientierung des Paraquat Moleküls an den Nanopartikeloberflächen vermuten.

In einer weiteren Studie die anhand von Computersimulationen mittels DFT Berechnungen durchgeführt wurde, konnten weitere Orientierungen untersucht werden. Dabei wurde ein Goldcluster, bestehend aus 20 Goldatomen, zur Hilfe genommen sowie ein Goldeinkristall, bestehend aus 256 Goldatomen. Der Vergleich der unterschiedlichen Berechnungen mit experimentell aufgenommenen Spektren hat gezeigt, dass es bei Goldnanopartikeln und Paraquat vermutlich zu einer planaren Orientierung des Paraquat Moleküls zur Goldnanopartikeloberfläche kommt. In weiteren Studien könnten in der Zukunft noch weitere Geometrien durch Berechnungen untersucht werden, sowie eine ergänzende Untersuchung der SERS-Substrat Grundlagen.

Abstract

Pesticides are used in agriculture worldwide. The use of pesticides is monitored due to their hazardous potential. One method that is used as an analytical method is Surface-Enhanced Raman Spectroscopy (SERS). The SERS technique is based on the enhancement of the Raman signal by electric fields induced by nanoparticles. The resulting SERS signal is several orders of magnitude more intense than a Raman signal, which also enables detection in the trace range. Different SERS methods have been developed to identify the pesticides imidacloprid, thiram and paraquat, which are used with portable Raman spectrometers.

Firstly, a method was developed in which imidacloprid can be detected directly in the field using a Raman handheld spectrometer. Various agglomeration agents were analysed, including hydrochloric acid and various salts, in order to increase the SERS signal through agglomeration. The investigations showed that hydrochloric acid is significantly more suitable for agglomeration than the salts and also produces a better amplification of the SERS signal. It was also investigated whether filter paper and polylactide fabric are suitable as SERS substrates. It was found that polylactide is better suited as a SERS substrate base due to its hydrophobic effect. Furthermore, a model calculation was carried out which shows that potential pesticide residues of around 300 mg/kg can occur in agricultural soils.

In a further study, the aspect of the SERS substrate basis was taken up again and polylactide and polyethylene terephthalate/polyamide textiles were investigated as carrier materials for the SERS substrates, with polyethylene terephthalate/polyamide proving to be the most suitable. As part of this study, the method was extended to the pesticides thiram and paraquat. Detection limits in the nanogram to picogram range were determined. The comparison with the model calculation from the first study showed that the detection limits are therefore in a relevant range, namely below the quantity applied, which means that pesticide residues can also be detected.

In a further study, the developed method was extended to silver nanoparticles as active SERS substrates and analysed with regard to their different amplification compared to gold nanoparticles. It was shown that thiram is equally amplified by gold and silver nanoparticles and produces similar SERS spectra. Paraquat, on the other hand, produces different SERS spectra with gold and silver nanoparticles. This suggests a different orientation of the paraquat molecule on the nanoparticle surfaces. In a further study, which was carried out using computer simulations with DFT calculations, further orientations were investigated. A gold cluster consisting of 20 gold atoms and a gold single crystal consisting of 256 gold atoms were used. The comparison of the different calculations with experimentally recorded spectra showed that gold nanoparticles and paraquat probably have a planar orientation of the paraquat molecule to the gold nanoparticle surface. In future studies, further geometries could be investigated by calculations, as well as a supplementary investigation of the SERS substrate fundamentals.

Declaration of Scientific Contributions

This thesis includes articles that have been published in journals before. The articles have been published in cooperation with co-authors, with my own contributions declared as follows:

Chapter 3: *Andrea Hermsen, David Lamers, Justus Schoettl, Christian Mayer & Martin Jaeger (2021) In-Field Detection Method for Imidacloprid by Surface Enhanced Raman Spectroscopy, Toxicological & Environmental Chemistry, DOI: 10.1080/02772248.2021.1991929*

The literature research for this study was performed by Andrea Hermsen. The experiments were performed by Andrea Hermsen, David Lamers and Justus Schöttl. The manuscript was written and revised by Andrea Hermsen, while Martin Jäger and Christian Mayer supervised the study. The submission was handled by Andrea Hermsen and Martin Jäger.

Chapter 4: *Andrea Hermsen, Justus Schoettl, Florian Hertel, Matthias Cerullo, Adrian Schlueter, Christian Lehmann, Christian Mayer & Martin Jaeger (2022) Green Textile Materials for Surface Enhanced Raman Spectroscopy Identification of Pesticides Using a Raman Handheld Spectrometer for In-Field Detection, Applied Spectroscopy, DOI: 10.1177/00037028221097130*

The literature research for this study was performed by Andrea Hermsen. The Raman and SERS experiments were performed by Justus Schöttl, Florian Hertel and Matthias Cerullo. The TEM experiments were supervised by Christian Lehmann and performed by Adrian Schlüter. The manuscript was written and revised by Andrea Hermsen, while Martin Jäger and Christian Mayer supervised the study. The submission was handled by Andrea Hermsen and Martin Jäger.

Chapter 5: *Andrea Hermsen, Florian Hertel, Dominik Wilbert, Till Gronau, Christian Mayer & Martin Jaeger (2023) Pesticide Identification Using Surface-Enhanced Raman Spectroscopy and Density Functional Theory Calculations: From Structural Insights to On-Site Detection, Applied Spectroscopy, DOI: 10.1177/00037028241236501*

The literature research for this study was performed by Andrea Hermsen. The Raman and SERS experiments were performed by Florian Hertel and Dominik Wilbert. The quantum calculations were performed by Andrea Hermsen and Till Gronau. The manuscript was written and revised by Andrea Hermsen, while Martin Jäger and Christian Mayer supervised the study. The submission was handled by Andrea Hermsen and Martin Jäger.

Chapter 6: *Andrea Hermsen, Florian Hertel, Dominik Wilbert, Christian Mayer & Martin Jaeger (2024) MD and DFT Calculations to Analyze Raman and SERS Spectra of Paraquat—From Computer Aided Spectra Interpretation to Pesticide Identification, Applied Research, DOI: <https://doi.org/10.1002/appl.202400182>*

The literature research for this study was performed by Andrea Hermsen. The Raman and SERS experiments were performed by Florian Hertel and Dominik Wilbert. The quantum calculations were performed by Andrea Hermsen. The manuscript was written and revised by Andrea Hermsen, while Martin Jäger and Christian Mayer supervised the study. The submission was handled by Andrea Hermsen and Martin Jäger.

Table of Contents

1	Motivation and Research Goals	1
1.1	Motivation	1
1.2	Research Goals	4
2	Introduction and State-of-the-Art	9
2.1	Raman Spectroscopy	9
2.1.1	Quantum Theory Description	9
2.1.2	Classical Theory Description	11
2.2	Surface-Enhanced Raman Spectroscopy	12
2.2.1	Electromagnetic & Chemical Enhancement	12
2.2.2	Mathematical Description	13
2.3	Nanoparticles	15
2.3.1	Production of Nanoparticles	15
2.3.2	Plasmonic Properties	16
2.3.3	Agglomeration of Nanoparticles and Hot-Spots	17
2.4	Computational Chemistry	19
2.4.1	Hartree-Fock	20
2.4.2	Configuration Interaction & Coupled Cluster	23
2.4.3	Density Functional Theory	24
2.5	State-of-the-Art	26
2.5.1	Pesticides	26
2.5.2	Methods of Pesticide Analytics	27
2.5.3	SERS Substrates	29
3	In-Field Detection Method for Imidacloprid by Surface-Enhanced Raman Spectroscopy	39
3.1	Abstract	40
3.2	Introduction	40
3.3	Materials & Methods	42
3.4	Results & Discussion	44
3.5	Conclusion	51
4	Green Textile Materials for Surface-Enhanced Raman Spectroscopy Identification of Pesticides Using a Raman Handheld Spectrometer for In-Field Detection	55
4.1	Abstract	56
4.2	Introduction	56
4.3	Materials & Methods	57
4.4	Results & Discussion	59

4.5	Conclusion	69
4.6	Supplemental Information	70
5	Pesticide Identification Using Surface-Enhanced Raman Spectroscopy and Density Functional Theory Calculations: From Structural Insights to On-Site Detection	79
5.1	Abstract	80
5.2	Introduction	80
5.3	Materials & Methods	81
5.4	Results & Discussion	83
5.5	Conclusion	92
5.6	Supplemental Information	93
6	MD and DFT Calculations to Analyze Raman and SERS Spectra of Paraquat—From Computer Aided Spectra Interpretation to Pesticide Identification	105
6.1	Abstract	106
6.2	Introduction	106
6.3	Materials & Methods	107
6.4	Results & Discussion	109
6.5	Conclusion	113
6.6	Supplemental Information	114
7	Concluding Remarks and Outlook	119
7.1	Conclusion	119
7.2	Outlook	121
	Appendix	123
	List of Publications	124
	Curriculum Vitae	125
	Affidavit of affirmation	126
	Acknowledgements	126

1 Motivation and Research Goals

1.1 Motivation

Global food production is facing major challenges: We need to combat hunger in the world and fight the alarming decline in bee colonies, known as bee mortality, because without bees, pollination of certain plants and fruits is not possible. These two issues are interconnected and significantly affect ecosystems, human health, and global food security.¹⁻³

The world hunger problem is multifaceted, affecting millions of people and carrying far-reaching social, economic, and environmental consequences. Farmers rely on pesticides to meet the growing food demands of an expanding global population. While these chemicals safeguard crops from pests and weeds, boosting yields, their extensive use leads to unintended side effects.^{4,5}

One particularly concerning repercussion is bee mortality, primarily attributed to the toxic effects of pesticides. Bees are pivotal in pollinating crops, fruit trees and wild plants, which are crucial for food security and biodiversity, cf. Fig. 1.1. The steep decline in bee populations jeopardizes not only food production but also ecosystem stability worldwide.^{1,6,7}

Integrated crop protection is advocated, employing ecologically sustainable methods such as mechanical, physical, agronomic, biological, genetic engineering, and chemical approaches, sensibly coordinated and combined, cf. Fig 1.2.⁸ Chemical plant protection, albeit a component of these



Figure 1.1 – Collage of five different scenes from agriculture and nature that represent the motivational aspects of this work.

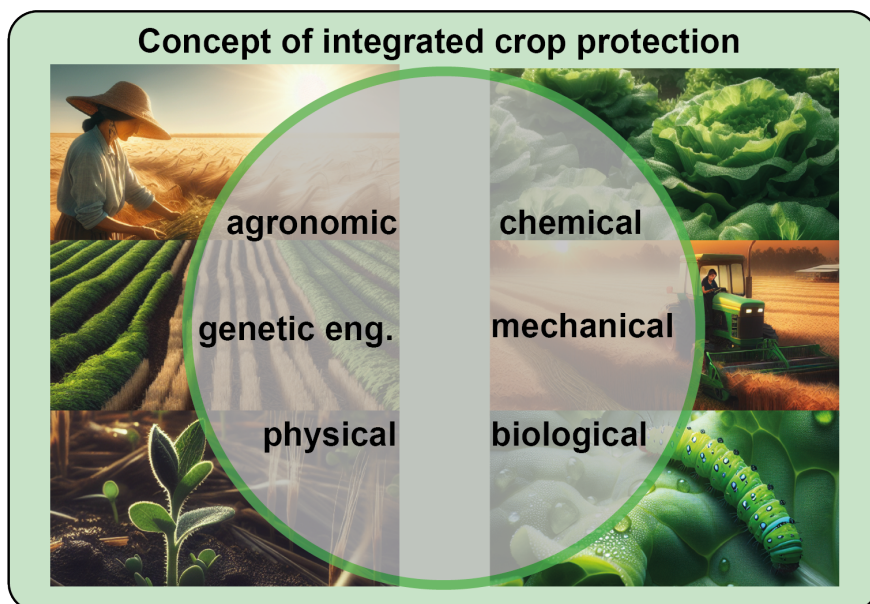


Figure 1.2 – Schematic presentation of the concept of integrated crop protection. With agronomic, genetic engineering, physical, chemical, mechanical, and biological crop protection.

methods, is subject to stringent criteria, with demand for high effectiveness, prolonged action, minimal application quantity, and associated low environmental impact.⁸

Recent discourse increasingly focuses on the environmental impact of pesticides, particularly their effects on insects crucial for ecosystem integrity.⁹ Studies unequivocally demonstrate the adverse effects of neonicotinoids, a subgroup of pesticides, on bees.¹⁰⁻¹³

In 2003, Thompson's study revealed the adverse impact of neonicotinoids and other chemicals, observing an attractant effect on bees contaminated with imidacloprid.¹⁰ Subsequent research by Henry et al. in 2012 indicated that thiamethoxam exposure impairs bee navigation.¹⁴ Pilling et al. found in their 2013 study bees transferring pesticides to nectar and pollen, attributing it to declining bee populations.¹¹ Similarly, Pettis et al. in 2013 demonstrated the broader impact of neonicotinoids on bees, even without direct contact.¹² Kessler et al. study from 2015 showed bees' preference for neonicotinoid-laced sucrose solutions, corroborating Thompson's findings.¹³ Recent studies reaffirm the negative impact of neonicotinoids on bees.^{15,16}

Moreover, Migdal et al. 2018 highlighted thiram's harmful impact of manufacturer-recommended doses on bee foraging.¹⁷ Hladik et al. questioned in 2018 the purported lower risks of neonicotinoids from seed coatings, emphasizing their widespread environmental presence and questioning their economic benefits.¹⁸ Gradish et al. comparative analysis revealed differing pesticide exposure risks between honey bees and bumble bees.¹⁹

Furthermore, Ostiguy et al. study showed prevalent insecticide contamination in bee products, stressing the urgent need for measures to mitigate long-term pesticide residue effects on bee colonies.²⁰ The investigation of Tome et al. demonstrated the detrimental effects of pesticide exposure on various aspects of bee development.²¹ The study in 2021 from Traynor et al. underscored the correlation between pesticide exposure and bee colony health decline in the US.²²

In 2022, Schuhmann et al. investigated neonicotinoid effects on honey and forest bees, emphasizing bees' contamination and subsequent presence in bee products.²³ Cousin et al. demonstrated

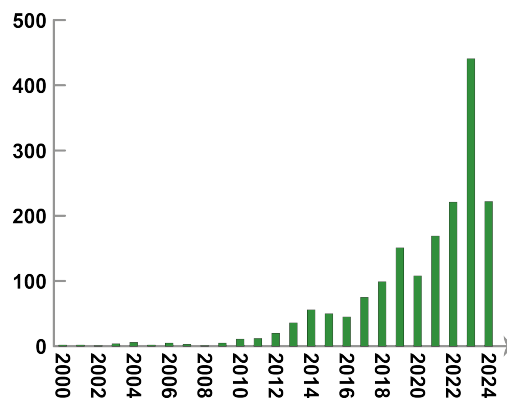


Figure 1.3 – Bar chart showing the annual publications for the keywords: "SERS, pesticides" between 2000 and 2024. Determined using the SciFinder database.

paraquat's adverse impact on honey bee larvae.²⁴ O'Reilly and Stanley's studies highlighted non-neonicotinoid pesticides' significant sublethal effects on bees, affecting their activity and pollination performance.^{25,26}

The study by Mueller et al. in 2024 underscored the unequal pesticide risks domesticated and wild honey bees face during apple pollination.²⁷ Angral et al. and Shepherd et al. published both in 2024 studies which further illustrated the adverse effects of neonicotinoids and other agrochemicals on bee foraging behavior, population dynamics, and colony activity.^{28,29}

Detection methods for pesticides have been established, such as gas chromatography-mass spectrometry (GC-MS) and liquid chromatography-mass spectrometry (LC-MS).^{30,31} Initially, GC and GC-MS methods were established at the beginning of pesticide analysis. However, pesticide analysis has changed significantly over the last two decades. Multi-residue analysis, the simultaneous detection of hundreds of pesticides, is now possible.³² The use of high-resolution mass spectroscopy has also led to the establishment of non-target screening. This technique enables the identification of compounds that have not previously been explicitly searched for.³³ Databases and automation have also made a significant contribution to the further development of pesticide analysis by significantly simplifying and speeding up the evaluation process with appropriate software solutions. Increasingly stringent regulations and bans have also further advanced the monitoring of pesticides.^{34,35} The HPLC and GC methods mentioned above have become particularly well established. However, despite all their advantages, these methods still require a laboratory environment and trained laboratory staff to operate these instruments.

Surface-enhanced Raman spectroscopy (SERS) has emerged as a promising tool for pesticide analysis, offering rapid, simple, and cost-effective detection.^{36,37} SERS enables the detection of pesticides in various matrices without sample preparation, supporting mobile spectrometers for field analysis.³⁸⁻⁴⁰ Continued research aims to enhance SERS substrates' sensitivity, selectivity, and reproducibility, widening its application range.^{36,41-46} SERS facilitates in-situ pesticide analysis directly on plant surfaces, offering the potential for field applications.⁴⁷

The number of scientific publications on the detection of pesticides using surface-enhanced Raman spectroscopy has increased significantly between 2000 and 2024, cf. Fig 1.3. It continued to rise steadily in 2023, and the figures for 2024 indicate that a new high level of publications on the detection of pesticides using SERS will be reached again.

1.2 Research Goals

Due to the aforementioned reasons outlined in the preceding section, this dissertation aims to develop a comprehensive approach to explore the application of surface-enhanced Raman scattering for the detection of pesticides. In the first part, a novel workflow is established to enable the acquisition of SERS spectra of imidacloprid as a model pesticide using gold nanoparticles and a handheld Raman spectrometer. Various agglomerating agents are investigated in solution to achieve optimal conditions for the SERS experiments. Solid SERS substrates such as filter paper and textiles are analyzed for their suitability, with a particular focus on sustainable textiles. The substrates are evaluated based on various aspects, including the amplification of the Raman signal, the background signal of the substrate, and intra- and inter-reproducibility.

Furthermore, the investigations include the pesticides imidacloprid, thiram and paraquat. An important focus is examining the possibility of transferring pesticides from vegetable samples to SERS substrates and obtaining SERS spectra of the pesticides.

The second part of the dissertation deals with quantum chemical calculations to development a spectrum prediction and interpretation method with which the substances can then be identified and detected. This is done via the identification of the vibrational modes amplified by the SERS effect in paraquat and thiram. SERS experiments are performed with gold and silver nanoparticles to analyze the molecules' interactions with the surfaces of the noble metals.

Finally, the orientation of the paraquat molecule on a gold nanoparticle is investigated in more detail. This is done by comparing experimental and simulated spectra and the corresponding modes for different orientations to gain a deeper understanding of the molecular interactions. This multidisciplinary research will contribute to further developing SERS technology for the detection of pesticides.

References

1. Li, X., Yadav, R. & Siddique, K. H. M. Neglected and Underutilized Crop Species: The Key to Improving Dietary Diversity and Fighting Hunger and Malnutrition in Asia and the Pacific. *Frontiers in Nutrition* **7**, e0136928 (2020).
2. Uddin, M. E. & Kebreab, E. Review: Impact of Food and Climate Change on Pastoral Industries. *Frontiers in Sustainable Food Systems* **4**, 386 (2020).
3. Sridhar, A., Balakrishnan, A., Jacob, M. M., Sillanpaa, M. & Dayanandan, N. Global impact of COVID-19 on agriculture: role of sustainable agriculture and digital farming. *Environmental Science and Pollution Research* **30**, 42509–42525 (2023).
4. Wood, T. J. & Goulson, D. The environmental risks of neonicotinoid pesticides: a review of the evidence post 2013. *Environmental Science and Pollution Research* **24**, 17285–17325 (2017).
5. Pawlak, K. & Kolodziejczak, M. The Role of Agriculture in Ensuring Food Security in Developing Countries: Considerations in the Context of the Problem of Sustainable Food Production. *Sustainability* **12**, 5488 (2020).

6. Lundin, O., Rundlof, M., Smith, H. G., Fries, I. & Bommarco, R. Neonicotinoid Insecticides and Their Impacts on Bees: A Systematic Review of Research Approaches and Identification of Knowledge Gaps. *PLOS ONE* **10**, e0136928 (2015).
7. Mukherjee, D. Food Security Under The Era Of Climate Change Threat. *Journal of Advanced Agriculture* **1**, 1–4 (2021).
8. Pretty, J. Agricultural sustainability: concepts, principles and evidence. *Philosophical Transactions of the Royal Society B: Biological Sciences* **363**, 447–465 (2007).
9. Tooming, E., Merivee, E., Must, A., *et al.* Behavioural effects of the neonicotinoid insecticide thiamethoxam on the predatory insect *Platynus assimilis*. *Ecotoxicology* **26**, 902–913 (2017).
10. Thompson, H. M. Behavioural Effects of Pesticides in Bees–Their Potential for Use in Risk Assessment. *Ecotoxicology* **12**, 317–330 (2003).
11. Pilling, E., Campbell, P., Coulson, M., Ruddle, N. & Tornier, I. A Four-Year Field Program Investigating Long-Term Effects of Repeated Exposure of Honey Bee Colonies to Flowering Crops Treated with Thiamethoxam. *PLOS ONE* **8**, e77193 (2013).
12. Pettis, J. S., Lichtenberg, E. M., Andree, M., *et al.* Crop Pollination Exposes Honey Bees to Pesticides Which Alters Their Susceptibility to the Gut Pathogen *Nosema ceranae*. *PLOS ONE* **8**, e70182 (2013).
13. Kessler, S. C., Tiedecken, E. J., Simcock, K. L., *et al.* Bees prefer foods containing neonicotinoid pesticides. *Nature* **521**, 74–76 (2015).
14. Henry, M., Beguin, M., Requier, F., *et al.* A Common Pesticide Decreases Foraging Success and Survival in Honey Bees. *Science* **336**, 348–350 (2012).
15. Woodcock, B. A., Bullock, J. M., Shore, R. F., *et al.* Country-specific effects of neonicotinoid pesticides on honey bees and wild bees. *Science* **356**, 1393–1395 (2017).
16. Tsvetkov, N., Samson-Robert, O., Sood, K., *et al.* Chronic exposure to neonicotinoids reduces honey bee health near corn crops. *Science* **356**, 1395–1397 (2017).
17. Migdal, P., Roman, A., Popiela-Pleban, E., Kowalska-Goralska, M. & Opalinski, S. The Impact of Selected Pesticides on Honey Bees. *Polish Journal of Environmental Studies* **27**, 787–792 (2018).
18. Hladik, M. L., Main, A. R. & Goulson, D. Environmental Risks and Challenges Associated with Neonicotinoid Insecticides. *Environmental Science & Technology* **52**, 3329–3335 (2018).
19. Gradish, A. E., van der Steen, J., Scott-Dupree, C. D., *et al.* Comparison of Pesticide Exposure in Honey Bees (Hymenoptera: Apidae) and Bumble Bees (Hymenoptera: Apidae): Implications for Risk Assessments. *Environmental Entomology* **48**, 12–21 (2018).
20. Ostiguy, N., Drummond, F. A., Aronstein, K., *et al.* Honey Bee Exposure to Pesticides: A Four-Year Nationwide Study. *Insects* **10**, 13 (2019).
21. Tome, H. V. V., Schmehl, D. R., Wedde, A. E., *et al.* Frequently encountered pesticides can cause multiple disorders in developing worker honey bees. *Environmental Pollution* **256**, 113420 (2020).
22. Traynor, K. S., Tosi, S., Rennich, K., *et al.* Pesticides in honey bee colonies: Establishing a baseline for real world exposure over seven years in the USA. *Environmental Pollution* **279**, 116566 (2021).

23. Schuhmann, A., Schmid, A. P., Manzer, S., Schulte, J. & Scheiner, R. Interaction of Insecticides and Fungicides in Bees. *Frontiers in Insect Science* **1**, 129 (2022).
24. Cousin, M., Silva-Zacarin, E., Kretzschmar, A., *et al.* Size Changes in Honey Bee Larvae Oenocytes Induced by Exposure to Paraquat at Very Low Concentrations. *PLOS ONE* **8**, e65693 (2013).
25. O'Reilly, A. D. & Stanley, D. A. Non-neonicotinoid pesticides impact bumblebee activity and pollen provisioning. *Journal of Applied Ecology* **60**, 1673–1683 (2023).
26. O'Reilly, A. D. & Stanley, D. A. Solitary bee behaviour and pollination service delivery is differentially impacted by neonicotinoid and pyrethroid insecticides. *Science of The Total Environment* **894**, 164399 (2023).
27. Mueller, T. G., Baert, N., Muniz, P. A., *et al.* Pesticide risk during commercial apple pollination is greater for honeybees than other managed and wild bees. *Journal of Applied Ecology* **61**, 1289–1300 (2024).
28. Angral, P. & Bandral, R. S. Effect of Thiacloprid Exposure on Honey Bees *Apis mellifera* F. *Indian Journal of Entomology* **86**, 118–122 (2024).
29. Shepherd, S., Park, Y.-g. & Krupke, C. H. Effects of common co-occurring pesticides (a neonicotinoid and fungicide) on honey bee colony health in a semi-field study. *Heliyon* **10**, e29886 (2024).
30. Alder, L., Greulich, K., Kempe, G. & Vieth, B. Residue analysis of 500 high priority pesticides: Better by GC–MS or LC–MS/MS? *Mass Spectrometry Reviews* **25**, 838–865 (2006).
31. Hogenboom A. C. and Niessen, W. M. A. & Brinkman, U. A. T. The role of column liquid chromatography-mass spectrometry in environmental trace-level analysis. Determination and identification of pesticides in water. *Journal of Separation Science* **24**, 331–354 (2001).
32. Roesch, A., Wettstein, F. E., Wächter, D., *et al.* A multi-residue method for trace analysis of pesticides in soils with special emphasis on rigorous quality control. *Analytical and Bioanalytical Chemistry* **415**, 6009–6025 (2023).
33. Manz, K. E., Feerick, A., Braun, J. M., *et al.* Non-targeted analysis (NTA) and suspect screening analysis (SSA): a review of examining the chemical exposome. *Journal of Exposure Science & Environmental Epidemiology* **33**, 524–536 (2023).
34. Agency, U. E. P. Guidance for Assessing Pesticide Risks to Bees. *Health Canada Pest Management Regulatory Agency (PMRA), and California Department of Pesticide Regulation* (2014).
35. Authority, E. F. S. Evaluation of the data on clothianidin, imidacloprid and thiamethoxam for the updated risk assessment to bees for seed treatments and granules in the EU. *EFSA Supporting Publications* **15**, 1378E (2018).
36. Kneipp, K., Wang, Y., Kneipp, H., *et al.* Single Molecule Detection Using Surface-Enhanced Raman Scattering (SERS). *Physical Review Letters* **78**, 1667–1670 (1997).
37. Moskovits, M. Surface-enhanced Raman spectroscopy: a brief retrospective. *Journal of Raman Spectroscopy* **36**, 485–496 (2005).
38. Yu, W. W. & White, I. M. Inkjet-printed paper-based SERS dipsticks and swabs for trace chemical detection. *Analyst* **138**, 1020–1025 (2013).

39. Lee, C. H., Tian, L. & Singamaneni, S. Paper-Based SERS Swab for Rapid Trace Detection on Real-World Surfaces. *ACS Applied Materials & Interfaces* **2**, 3429–3435 (2010).
40. Zheng, J., Pang, S., Labuza, T. P. & He, L. Semi-quantification of surface-enhanced Raman scattering using a handheld Raman spectrometer: a feasibility study. *Analyst* **138**, 7075–7078 (2013).
41. Zhao, J., Pinchuk, A. O., McMahon, J. M., *et al.* Methods for Describing the Electromagnetic Properties of Silver and Gold Nanoparticles. *Accounts of Chemical Research* **41**, 1710–1720 (2008).
42. Liu, H., Zhang, L., Lang, X., *et al.* Single molecule detection from a large-scale SERS-active Au79Ag21 substrate. *Scientific Reports* **1**, 112 (2011).
43. Le Ru, E. C. & Etchegoin, P. G. Single-Molecule Surface-Enhanced Raman Spectroscopy. *Annual Review of Physical Chemistry* **63**, 65–87 (2012).
44. Bell, S. E. J. & McCourt, M. R. SERS enhancement by aggregated Au colloids: effect of particle size. *Physical Chemistry Chemical Physics* **11**, 7455–7462 (2009).
45. Bao, L., Mahurin, S. M., Haire, R. G. & Dai, S. Silver-Doped Sol-Gel Film as a Surface-Enhanced Raman Scattering Substrate for Detection of Uranyl and Neptunyl Ions. *Analytical Chemistry* **75**, 6614–6620 (2003).
46. Hou, R., Pang, S. & He, L. In situ SERS detection of multi-class insecticides on plant surfaces. *Analytical Methods* **7**, 6325–6330 (2015).
47. Pang, S., Yang, T. & He, L. Review of surface enhanced Raman spectroscopic (SERS) detection of synthetic chemical pesticides. *Trends in Analytical Chemistry* **85**, 73–82 (2016).

2 Introduction and State-of-the-Art

First, the theoretical basics of Raman spectroscopy will be explained as they form the foundation of this work. Then, surface-enhanced Raman spectroscopy, derived from conventional Raman spectroscopy, will be discussed. Also, the properties of nanoparticles, which are essential for the SERS method, will be analyzed, focusing on the properties upon which the mechanisms of surface enhancement are based. Finally, a part of the area of computational chemistry will be reviewed. The necessary mathematical models used in quantum chemical calculations will be explained. Special attention is given to Hartree-Fock, the basis of almost all computational algorithms, and density functional theory, which is used in a wide range of chemistry today. Finally, the state of the art with regard to the pesticides imidacloprid, thiram and paraquat is explained, and different methods of pesticide analysis and SERS substrates used for pesticide detection are discussed.

2.1 Raman Spectroscopy

In 1928, the Indian physicist C. V. Raman experimentally demonstrated the Raman effect, which had already been predicted five years earlier by A. Smekal.¹ In his experiments, Raman showed that the wavelength of a small part of the scattered radiation emitted by a molecule differs from the incident radiation. Moreover, he showed that this shift in wavelength depends on the structure of the scattering molecules. For this work, Raman was awarded the Nobel Prize in 1931.² The following fundamentals of Raman spectroscopy are based on the textbook by Goepel and Ziegler.³

Two explanations are possible for Raman spectroscopy. First, we will examine the quantum theory description of the Raman effect, and second, we will explain the Raman effect with classical mechanics.

2.1.1 Quantum Theory Description

In Raman spectroscopy, the spectral excitation is usually caused by radiation of a wavelength that is not absorbed by the analyte, but instead scattered. The energy level diagram, in Fig. 2.1, shows the causes of Rayleigh and Raman scattering. Three different scattering processes are possible when a molecule interacts with a quantum of incident radiation. Stokes scattering is shown on the left of the figure. Here, the molecule absorbs energy from the light quanta of the radiation. The opposite case is shown on the right side of the figure. Here, a quantum of light from the molecule, which has been already excited, is emitted the photon has higher energy than before the interaction with the molecule. This is called anti-Stokes scattering. Stokes and anti-Stokes scattering are inelastic collision or collision processes. If there is no energy transfer between the radiation and the molecule, i.e., if the collision process is elastic, it is called Rayleigh scattering, Fig. 2.1, center.

In the quantum theoretical interpretation, the excitation light beam consists of photons of the energy $h\nu_0$, scattered by collisions of the photons with molecules. In the case of the collisions of

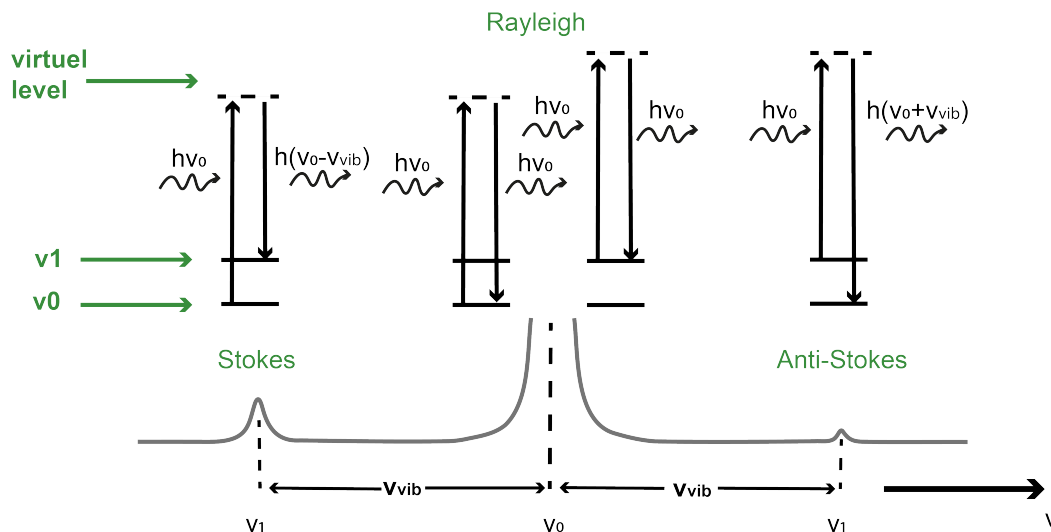


Figure 2.1 – Schematic depiction of the scattering process of Rayleigh- and Raman scattering. Modified from Goepel & Ziegler.³

photons with molecules, two different collision processes must be distinguished in principle. On the one hand, the elastic collision is called Rayleigh scattering. In this kind of collision, the energy remains constant, and the scattered radiation has the same frequency as the excitation radiation, $\nu_i = \nu_0$.

Rayleigh scattering occurs in all molecules. To be distinguished from this are the inelastic collisions, which are accompanied by a change in energy. Therefore, they have a frequency different from the excitation radiation. This type of scattering is called Stokes or anti-Stokes scattering. For Stokes scattering $\nu_i < \nu_0$ and for anti-Stokes scattering $\nu_i > \nu_0$. This type of scattering only occurs in molecules where the polarizability changes as a function of time. In Rayleigh scattering, the elastic collision, the molecule goes from the ground state ν_0 , or an excited state ν_i , to a much higher, instationary state. This state is called a virtual level. The molecule immediately falls back to the initial level. A photon with the original energy is emitted, which can be detected as a Rayleigh band.

During the collision, a small number of the molecules enters the virtual level and then the first excited vibrational state, $\nu = 1$. In this case, a photon is emitted with energy reduced by the energy of the corresponding transition, $\nu = 0 \rightarrow \nu = 1$. In the Raman spectrum, this becomes clear when the Stokes line shifts to lower frequencies. The result is a redshift. The reverse case is also possible, in which the molecule relaxes from an excited state via the virtual state to the ground state by the collision with a photon. In this case, a photon with increased energy is emitted, and a blue shift occurs since the anti-Stokes line is now shifted to higher frequencies in the Raman spectrum. However, since molecules are usually in the ground state at room temperature, anti-Stokes collisions much less frequently occur.

It should be emphasized that the virtual state is not a stationary vibrational or electron state but a solution of the time-dependent Schrödinger equation. Thus, Raman spectroscopy is a two-photon process in which a photon *A* with energy *a* is first annihilated, then a photon *B* with energy *b* is created. The virtual state, therefore, exists only for a short time, and the transitions must not be confused with the regular absorption and emission processes, which are a one-photon process

in which photon A and energy A are absorbed or emitted. This process takes place only between stationary states but not in scattering processes.

2.1.2 Classical Theory Description

The classical mechanical interpretation starts from the wave theory of light and postulates for electrons, which are in an electromagnetic field, forced oscillations of the frequency ν_0 , which are modeled by the natural frequency ν_{vib} of the molecule to $\nu_0 + \nu_{vib}$. If a monochromatic beam of light ν_0 impinges on a molecule, the electric field \vec{E} of this radiation can be described according to Eq. 2.1.

$$\vec{E} = -\vec{E}_0 \cos(2\pi\nu_0 t) \quad (2.1)$$

In this process, the oscillating electric field vector \vec{E}_0 periodically pushes the easily movable negative charge of the outer electron shell against the positive atomic trunks. How easily the electrons of a molecule can be set into oscillation depends on the polarizability α of the molecule itself. Thus, an oscillating dipole is $\vec{\mu}_{ind}$ induced by the interaction of the electric field \vec{E} with the electrons of the molecule. If the molecule oscillates with the frequency ν_{vib} , the normal coordinate q_i of the oscillation changes according to equation 2.2.

$$\vec{\mu}_{ind} = -\alpha \vec{E} = -\alpha \vec{E}_0 \cos(2\pi\nu_0 t) \quad (2.2)$$

This molecule oscillation can also change the polarizability α , and how easily the molecule's electrons can be set to oscillation depends also on the polarizability. This polarizability can be described as an average polarizability in the equilibrium position α_0 and a part of the change during the oscillation as follows:

$$q_i = -q_{i,max} \cos(2\pi\nu_{vib,i} t) \quad (2.3)$$

If the molecule starts to oscillate due to the interaction with the light, the frequency changes from ν to $\nu_{vib,i}$. Also, the normal coordinate q_i changes, which becomes $q_{i,max}$ at the place of maximum deflection of the oscillation.

$$\alpha_i = \alpha_0 + \frac{\partial \alpha}{\partial q_i} q_i \dots \quad (2.4)$$

Since the molecule is now in oscillation, the polarizability of the electrons must also change depending on the spatial coordinate. Here, α_0 denotes the average polarizability in the equilibrium position. Thus, the total polarizability is a sum of the polarizability of the equilibrium position and the parts that consider the change during the shift α_i and q_i .

If we now insert the equations 2.3 and 2.4 into equation 2.2 and take into account the trigonometric relationship $\cos(\alpha) \times \cos(\beta) = \frac{1}{2} [\cos(\alpha - \beta) + \cos(\alpha + \beta)]$, we obtain Eq. 2.5.

$$\vec{\mu}_{ind} = -\alpha_0 \vec{E}_0 \cos(2\pi\nu_0 t) + \frac{\vec{E}_0 q_{i,max}}{2} \frac{\partial \alpha}{\partial q_i} [\cos 2\pi(\nu_0 - \nu_{vib,i})t + \cos 2\pi(\nu_0 + \nu_{vib,i})t] \quad (2.5)$$

From Eq. 2.5, it can be deduced that the induced dipole moment $\vec{\mu}_{ind}$ oscillates with the three superimposed frequencies ν_0 , $\nu_0 - \nu_{vib,i}$, and $\nu_0 + \nu_{vib,i}$, respectively. From Eq. 2.4, it can also be

deduced that Raman scattering only occurs when the derivative of the polarizability concerning the spatial coordinate is not equal to zero ($\frac{\partial \alpha}{\partial q_i} \neq 0$). It is, therefore, a necessary condition of Raman spectroscopy is that the polarizability must change in the course of the molecular vibration. It was also shown in Eq. 2.2 that the change of the polarizability causes an oscillating dipole and, from this, the condition for the emission of electromagnetic radiation.

2.2 Surface-Enhanced Raman Spectroscopy

Surface-enhanced Raman spectroscopy is now widely utilized across scientific fields, permeating chemistry, environmental science, biochemistry, materials science, and medicine.⁴ The SERS effect was first observed by Fleischmann and colleagues in 1974 as they investigated pyridine on roughened silver surfaces.⁵ However, it wasn't until three years later that Jeanmaire and van Duyne, along with Albrecht and Creighton independently, recognized that the amplification of the electromagnetic field of nanoparticles is the cause of the SERS effect.^{6,7} In 1978, Moskovits was the first to explain the connection between nanoparticles and signal amplification in SERS experiments.⁸

Thus, the SERS effect could be attributed to two different mechanisms. As can be seen in eq. 2.2, the dipole moment μ_{ind} depends on the electric field E and the polarizability α . From this it can be deduced that an enhancement must occur if either one of these or both are increased simultaneously. If there is an increase in the electric field, this is referred to as electromagnetic enhancement, also known as em theory. If there is an increase in the polarizability is called chemical enhancement.⁹ A SERS-active substrate is always required for the SERS technique. In the simplest case, this can be a colloidal nanoparticle solution. The nanoparticles commonly used in SERS experiments are typically made of gold, silver, or copper. However, precipitated SERS-active substrates made of rubidium, platinum, or rhodium are also known, as well as elements from the 1st to the 3rd main groups of the periodic table of elements. However, much more complex substrates with gold nanoparticles can also be produced.⁴

2.2.1 Electromagnetic & Chemical Enhancement

The electromagnetic enhancement is a feature dependent on the SERS substrate. Depending on the potency of the SERS substrate, electromagnetic enhancement can yield a SERS amplification of 10^{10} .¹⁰ To achieve optimal amplification, the substrate should be designed so that the distance between the analyte molecule and the nanoparticle falls within the range of 1-10 nm. Additionally, the electromagnetic effect depends on the type of the analyte molecule. A higher amplification can be expected for highly symmetrical molecules, as they have higher signal intensities due to a higher amplification depending on their position and orientation in relation to the nanoparticle.^{4,11}

The electromagnetic effect can be subdivided into the near field and re-radiation amplification. Near-field amplification produces "hot spots" where the spectral pattern affects the molecule's polarizability with a much stronger electric field than that generated by a single nanoparticle.¹² Re-radiation amplification results from a change in the molecule's environment, as the molecule itself is a dipole and the radiation of a dipole relies on its surroundings.⁴

In contrast to electromagnetic amplification, chemical amplification is independent of the SERS substrate but relies on the nature of the analyte molecule. Due to the chemical effect, amplifications

of up to $10^2 - 10^4$ are achievable. Moreover, the distance between the molecule and the nanoparticle must be much smaller, with direct contact between them or a distance no more than a few angstroms. The chemical effect also determines the SERS spectrum's pattern by affecting the molecule's polarizability, which changes upon bonding with the nanoparticle. The chemical effect can be traced back to physical adsorption or chemical absorption.¹³ These processes differ in the interaction enthalpy released; for instance, the interaction enthalpy must be less negative than -25 kJ/mol for physical adsorption and more negative than -40 kJ/mol for chemical adsorption.^{8,10,14}

2.2.2 Mathematical Description

The mathematical description is based on the work by Joseph.¹⁵

The electric field that directly influences the area around the nanoparticle can be described using Mie theory by solving Maxwell's equations.¹⁶ When the condition applies for a spherical nanoparticle, namely that its radius r is significantly smaller than the wavelength of the exciting light, the strength of the electric field remains constant, and Maxwell's equations can be solved using a quasi-stationary approach.¹⁷ This solution yields equation 2.6, which describes the electric field on the nanoparticle, E_{NP} .

$$E_{NP} = \frac{\varepsilon - \varepsilon_0}{\varepsilon + 2\varepsilon_0} \cdot \left(\frac{r}{r+d}\right)^3 \cdot E_0 \quad (2.6)$$

Here, ε and ε_0 represent the dielectric constants of the nanoparticle and the surrounding medium, respectively, r denotes the radius of the nanoparticle, and E_0 stands for the electric field of the exciting radiation. When the analyte molecule is within a distance d from the nanoparticle, the total field E_{local} acting on the nanoparticle can be expressed as the sum of the exciting radiation field E_0 and the nanoparticle's field E_{NP} , as shown in equation 2.7:

$$E_{local} = E_0 + E_{NP} \quad (2.7)$$

Substituting eq. 2.6 into eq. 2.7 gives eq. 2.8

$$E_{local} = \left(1 + \frac{\varepsilon - \varepsilon_0}{\varepsilon + 2\varepsilon_0} \cdot \left(\frac{r}{r+d}\right)^3\right) \cdot E_0 \quad (2.8)$$

Since $\frac{\varepsilon - \varepsilon_0}{\varepsilon + 2\varepsilon_0} \cdot \left(\frac{r}{r+d}\right)^3 \gg 1$ applies in the vicinity of $Re(\varepsilon) = -2\varepsilon_0$, $E_{loc} \approx E_{NP}$ follows according to the formulation of Metiu and Das.¹⁸

Equation 2.8 is then utilized to formulate the field amplification factor $A(\nu)$, as described in equation 2.9.

$$A(\nu) = \frac{E_{local}}{E_0} \sim \left(\frac{\varepsilon - \varepsilon_0}{\varepsilon + 2\varepsilon_0}\right) \cdot \left(\frac{r}{r+d}\right)^3 \quad (2.9)$$

This field amplification factor can now be formulated for the amplification of the electric field, which is caused on the one hand by the frequency of the laser radiation $A(\nu_l)$ and on the other hand by the scattered radiation emitted by the molecule with the frequency $A(\nu_s)$. The latter is known as the antenna effect. This results in equations 2.10 and 2.11.

$$A(\nu_l) = \frac{\varepsilon(\nu_l) - \varepsilon_0}{\varepsilon(\nu_l) + 2\varepsilon_0} \cdot \left(\frac{r}{r+d}\right)^3 \quad (2.10)$$

as well as

$$A(\nu_s) = \frac{\varepsilon(\nu_s) - \varepsilon_0}{\varepsilon(\nu_s) + 2\varepsilon_0} \cdot \left(\frac{r}{r+d}\right)^3 \quad (2.11)$$

As eq. 2.10 and 2.11 show, a correspondingly large amplification can only occur if the denominator $\varepsilon(\nu) + 2\varepsilon_0$ is minimal. This occurs due to the dielectric function of gold and silver. Since the intensity of an electromagnetic field depends on the square of the transition moment and the square of the magnitude of the field strength, the field amplification factors $A(\nu)$ are squared. Eq. 2.10 and eq. 2.11 thus become eq. 2.12 and eq. 2.13.

$$|A(\nu_l)|^2 = \left| \frac{\varepsilon(\nu_l) - \varepsilon_0}{\varepsilon(\nu_l) + 2\varepsilon_0} \right|^2 \cdot \left(\frac{r}{r+d}\right)^6 \quad (2.12)$$

as well as

$$|A(\nu_s)|^2 = \left| \frac{\varepsilon(\nu_s) - \varepsilon_0}{\varepsilon(\nu_s) + 2\varepsilon_0} \right|^2 \cdot \left(\frac{r}{r+d}\right)^6 \quad (2.13)$$

To describe the total local gain, the product of eq. 2.12 and eq. 2.13 is formed and designated as the local gain g^{SERS} according to eq. 2.14.

$$g^{SERS} = |A(\nu_l)|^2 \cdot |A(\nu_s)|^2 = \left| \frac{\varepsilon(\nu_l) - \varepsilon_0}{\varepsilon(\nu_l) + 2\varepsilon_0} \right|^2 \cdot \left| \frac{\varepsilon(\nu_s) - \varepsilon_0}{\varepsilon(\nu_s) + 2\varepsilon_0} \right|^2 \cdot \left(\frac{r}{r+d}\right)^{12} \quad (2.14)$$

If eq. 2.6 is reformulated as eq. 2.15

$$\frac{E_{NP}}{E_0} = \frac{\varepsilon - \varepsilon_0}{\varepsilon + 2\varepsilon_0} \cdot \left(\frac{r}{r+d}\right)^3 \quad (2.15)$$

and replaces E_{NP} with the respective induced field on the nanoparticle $E(\nu_l)$ and $E(\nu_s)$, and uses these two equations, eq. 2.12 and eq. 2.13, into eq. 2.14, the equation 2.16 is formed and gives the total amplification G^{SERS} .

$$G^{SERS} = \frac{|E(\nu_l)|^2 \cdot |E(\nu_s)|^2}{|E_0|^2} \quad (2.16)$$

Here, the terms $|E(\nu_l)|^2$ and $|E(\nu_s)|^2$ are summarized as the locally acting field responsible for the amplification $E_{(local,SERS)}$. Finally, equation 2.16 can be reformulated in squared form as shown in equation 2.17:

$$G^{SERS} = \frac{|E_{loc,SERS}|^2}{|E_0|^2} \quad (2.17)$$

In their publication, Kerker et al. also show the squared form of eq. 2.17, shown in eq. 2.18.^{19,20}

$$G^{SERS} = \left(\frac{|E_{loc,SERS}|^2}{|E_0|^2} \right)^2 \quad (2.18)$$

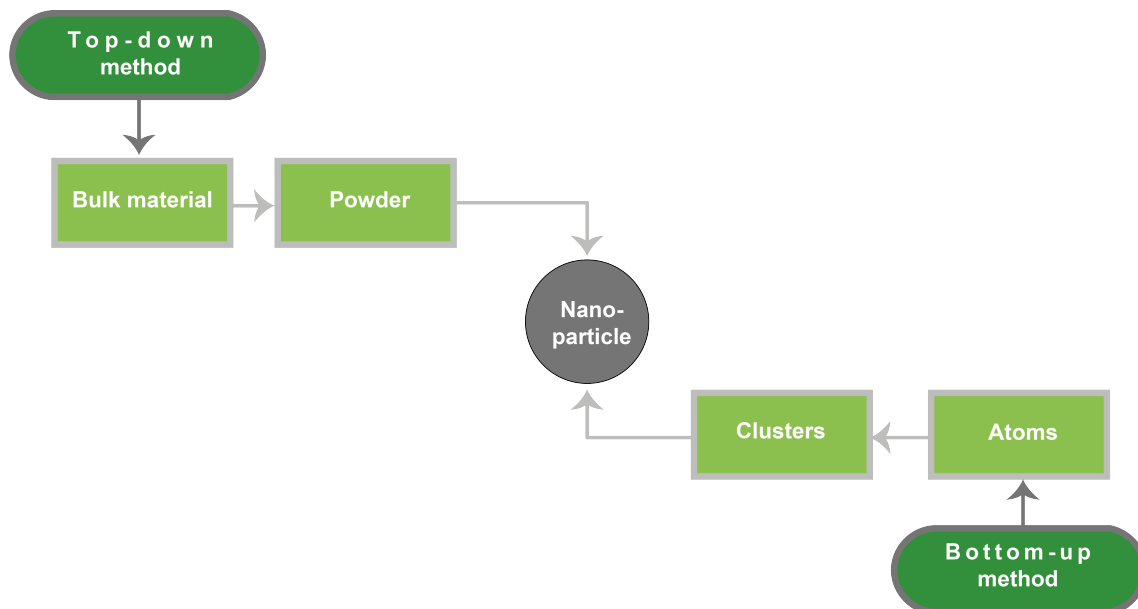


Figure 2.2 – Scheme of different processes for the preparation of nanoparticles

However, the eq. 2.17 is usually used to calculate the enhancement factor.¹⁵ However, when comparing enhancement factors, it is important to check which formula was used to calculate them in order to ensure comparability.

2.3 Nanoparticles

The first person to predict nanotechnology was Nobel laureate Richard P. Feynman. Feynman presented ideas on how technology can work at the microscopic level in his lecture “There’s Plenty of Room at the Bottom” at the California Institute of Technology in 1959. The critical points of this lecture were the possibilities of data storage, the need for better electron microscopes, the advantages of miniaturized computers, the construction of microscopic machines, and physical molecule manipulation.²¹ From then until today, much progress has occurred in nanotechnology. One is the development of nanoparticles. Nanoparticles can now be found in a wide variety of applications. These include chemical and biological sensing, drug delivery, CO₂ capturing, and bioimaging applications.²²⁻²⁷

2.3.1 Production of Nanoparticles

Due to the wide range of nanoparticle applications, they are also produced from an equally wide range of materials. The materials of production can be roughly divided into metal-, carbon-based-, ceramic-, semiconductor-, polymer- and lipid-based nanoparticles.²⁸ There are two main ways: cf. Fig. 2.2 in which nanoparticles can be produced, the top-down and the bottom-up process. The top-down method is primarily used in physics or electrical engineering. In this process, larger compound pieces are processed into nanoscale structures by milling, etching, or other mechanical methods. The bottom-up process is applied in the fields of chemistry and biology. Here, nanostructures are synthesized from atomic or molecular components.²⁹ The top-down method can be roughly divided into two different processes. On the one hand, there is the evaporation & condensation method.

This method can produce tiny nanoparticles ranging from 3 to 5 nm. To achieve this, a piece of metal or a powder of the same metal is first placed in a furnace. The metal is then heated so that its top layer transitions to a gaseous state, and a gas stream carries away the individual metal atoms. The required temperature varies depending on the metal in question. For gold, for example, with a melting temperature of 1065 °C, the furnace is heated to approximately 1700 °C to vaporize the metal atoms. One method of capturing the metal atoms involves using a transmission electron microscopy sample grid. The nanoparticles formed adhere to the grid and can be separated.³⁰⁻³² In the laser ablation method, the material from which the nanoparticles are to be produced is scanned with a laser. The laser's pulse duration and the metal's electron-photon coupling are crucial factors. This coupling converts the laser's energy into heat, concentrating it at a particular point. This results in temperatures exceeding 10,000 K. Such high energy is adequate to vaporize the metal. The significant temperature differential creates a shockwave, which induces spontaneous condensation of the vaporized metal atoms, leading to the formation of nanoparticles.³³

The bottom-up method encompasses thermal decomposition, chemical reduction, and biological reduction processes for nanoparticle synthesis.

In thermal decomposition, nanoparticles are generated through the breakdown of metal complexes at elevated temperatures. For instance, silver oxalate decomposes at 140 °C, yielding elemental silver and CO₂. By cleaving the C-C bond in the oxalate, electrons are liberated to reduce silver ions, resulting in the formation of stable silver nanoparticles.³⁴

Chemical reduction involves reducing metal salts to their elemental forms to produce nanoparticles. Shape, size, and ligands can be precisely controlled to tailor the nanoparticle synthesis. The Turkevich method, for example, utilizes gold chloride and sodium citrate to synthesize gold nanoparticles. Sodium citrate acts as a reducing agent, facilitating the reduction of gold ions from the gold chloride solution. The size and morphology of the resulting nanoparticles can be manipulated by adjusting the ratio of gold chloride to sodium citrate.³⁵

Biological reduction offers another avenue for bottom-up nanoparticle synthesis. The mechanism resembles chemical reduction but employs biological agents such as plant extracts, fungi, or microorganisms. These agents are reducing agents and stabilizers in nanoparticle synthesis, utilizing specific biological pathways to control particle formation.³⁶

2.3.2 Plasmonic Properties

Nanoparticles can generate localized surface plasmons due to their size, evident in the distinct colors observed in silver and gold nanoparticles. When light of a specific wavelength interacts with nanoparticles, the oscillating electromagnetic fields induce a coherent, collective oscillation in the conductionband electrons, cf. Fig. 2.3. These electrons are displaced away from the positive nuclear charges, and the resulting Coulomb attraction creates a restoring force such that the electrons oscillate relative to the position of the favorable core structure at a particular frequency.

When incident light matches the resonant frequency of the surface plasmon oscillation, it is absorbed, leading to the appearance of a plasmon band in the absorption spectrum. For spherical particles, this band typically appears around 530 nm for gold nanoparticles and 420 nm for silver nanoparticles. Modifying the size or shape of the nanoparticles can shift this plasmon band, cf. Fig. 2.4.

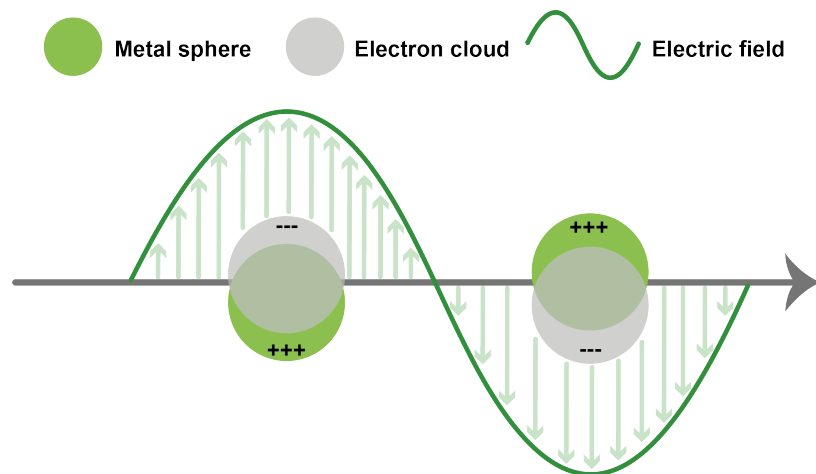


Figure 2.3 – Scheme of localized surface plasmons of nanoparticles

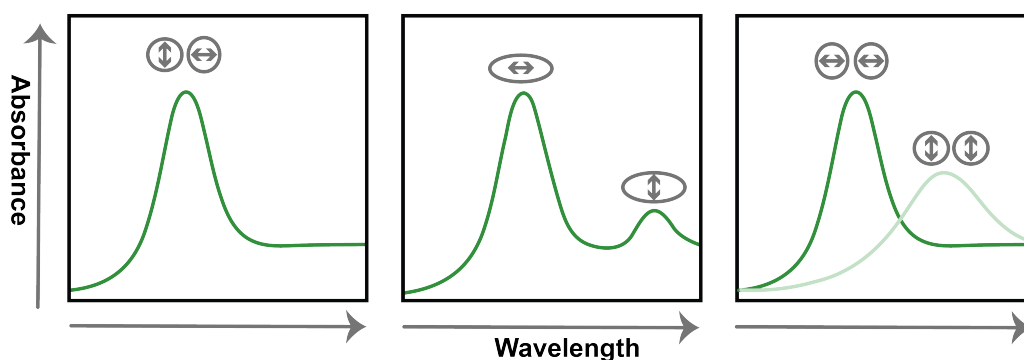


Figure 2.4 – Scheme of different plasmon bands caused by nanoparticles.

Spherical nanoparticles generate only one plasmon band, as their oscillation is the same in the transverse and longitudinal directions, cf Fig. 2.4, left. Non-spherical nanoparticle shapes, such as nanorods, can exhibit multiple plasmon bands. In the case of nanorods, a characteristic plasmon resonance occurs at longer wavelengths due to the oscillation of free electrons in the longitudinal direction of the nanoparticle structure, cf Fig. 2.4, middle. The length of a nanorod determines the extent to which the plasmon resonance is shifted towards higher wavelengths. If aggregation of spherical nanoparticles occurs, the transverse oscillation remains the same, but the longitudinal oscillation of the agglomerated nanoparticles produces a second band at higher wavelength, cf Fig. 2.4, right.³⁷

2.3.3 Agglomeration of Nanoparticles and Hot-Spots

If nanoparticles aggregate, the process is referred to as aggregation. When considered within a thermodynamic framework, nanoparticles inherently seek a lower energy state, typically achieved through growth such as aggregation.³⁸ To counteract agglomeration, various ligands can be employed to stabilize nanoparticle suspensions.³⁹ Two primary stabilization methods are electrochemical and steric stabilization. Electrochemical stabilization involves using salts as ligands, which adhere to nanoparticles via their charge. Conversely, steric stabilization occurs through polymers that covalently bind to nanoparticles, preventing their aggregation through chain entanglement.³⁸

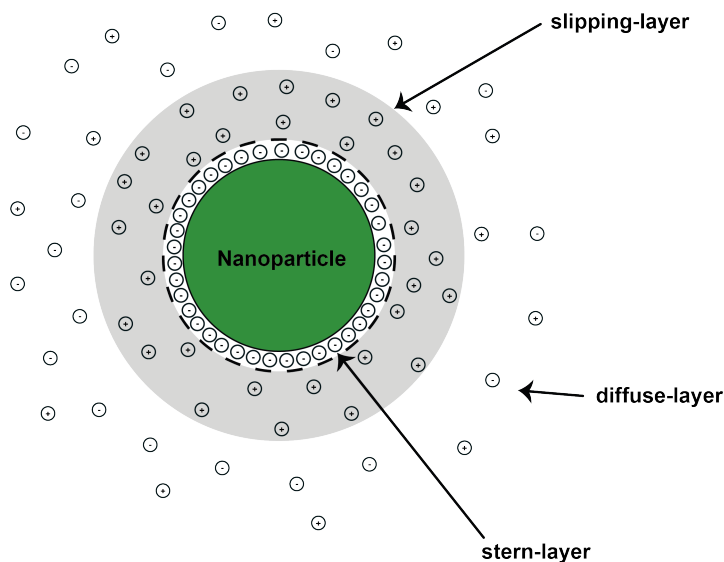


Figure 2.5 – Scheme of zeta potential with stern-layer, slipping-layer and diffuse-layer around a nanoparticle.

A common ligand employed for electrochemical stabilization is citrate. According to the Derjaguin-Landau-Verwey-Overbeek (DLVO) theory, citrate or its corresponding ligand physically adsorbs onto the nanoparticle surface via its charge, forming a so-called stern-layer, cf. Fig. 2.5.⁴⁰ Within this layer, the two carboxyl groups of citrate orient towards the nanoparticle, while the third protrudes outward, imparting a negative charge to the nanoparticle-citrate complex. Cations in solution then attach to this negative charge, forming a layer known as the slipping layer, which shields the attractive forces of the stern layer. This results in the formation of a diffuse layer around the nanoparticle-citrate complex. The potential difference between the slipping and diffuse layers is termed the zeta potential.⁴¹

In stable systems, the zeta potential is typically high. Therefore, the zeta potential indicates the stability of a colloidal suspension, with stability generally achieved at a zeta potential of ± 30 mV. A decrease in the zeta potential corresponds to a reduction in interparticle repulsion forces, leading to agglomeration and subsequent flocculation.^{4,39}

The aggregation of nanoparticles results in the formation of so-called hot spots, which occur due to the reduction of the zeta potential and, consequently, the reduction of interparticle repulsive forces. This process leads to the formation of clusters of nanoparticles. The size of these nanoparticle clusters can be specifically controlled using various agglomeration agents and ligands. Possible agglomerating agents include mineral acids, hydrochloric acid, or salt solutions. The introduction of additional ions into the system reduces the Gibbs energy.⁴² As a result, the van der Waals forces become significantly stronger than the zeta potential, leading to a new equilibrium.⁴¹

The electromagnetic field around them significantly increases when nanoparticles agglomerate and come closer together. The coupling of individual surface plasmons creates new resonances at higher wavelengths. The resonance depends on the geometric shape of the nanoparticles; for example, spheres form differently distributed electric fields compared to cubic systems. The newly formed electric fields created by coupling surface plasmons are significantly more robust and exhibit much higher amplification in SERS experiments.^{39,44} Figure 2.6 shows the strength of the electric field of simple nanostructures depending on their geometry, such as a sphere (a) or a cube (b). When two structures of the same geometry begin to interact with each other, the electric field is strengthened

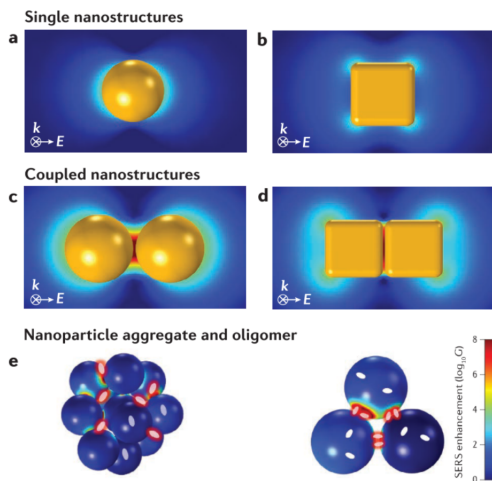


Figure 2.6 – Intensity of the electric field of simple nanostructures such as a sphere a) or a cube b). Coupling of spherical nanoparticles c) and cube nanoparticles d). Agglomeration of the spherical nanoparticles creates several hot spots e). Modified figure from Ding et al.⁴³

by the new resonance that is created. The coupling of the electric field of spherical nanoparticles (c) generates a significantly more intense electric field than the coupling of square nanoparticles (d). In e) it can be seen that by agglomeration of spherical nanoparticles significantly more nanoparticles couple and generate a larger hot spot than with agglomeration of square nanoparticles.

2.4 Computational Chemistry

The Hartree-Fock method serves as the basis for most modern quantum chemical calculations. However, it is no longer used as a stand-alone method since it provides somewhat inferior results compared to the state of the art. By applying density functional theory, significantly better results can be achieved within the same computation time. Nevertheless, the basics of Hartree-Fock will be discussed since they form a fundamental understanding of more modern methods.

This text provides a brief introduction to Configuration Interaction and Coupled Cluster methods. Density Functional Theory is explained in more detail, as this method is utilized in the later research section. The advantages and disadvantages of the four different methods are also discussed, cf. Fig 2.7.

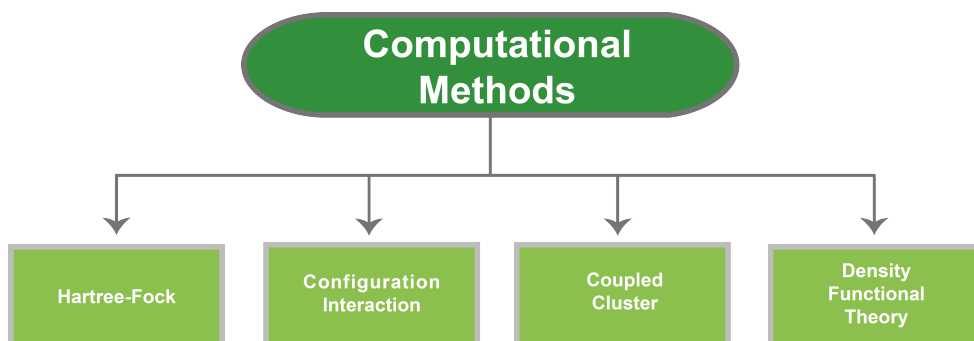


Figure 2.7 – Schematic depiction of different computational chemistry methods.

2.4.1 Hartree-Fock

Hartree-Fock (HF) is one of the so-called *ab initio* methods. The term *ab initio* comes from Latin and means "from the beginning", meaning that in the *ab initio* calculations, only fundamental constants are used when solving the Schrödinger equation. The opposite of *ab initio* calculations are semi-empirical calculations.^{45,46} Thereby, approximations are introduced, accelerating the computation and reducing the computation time strongly. If quantum-chemical calculations are taken for assistance, the Schrödinger equation must be solved in the first instance. The time-independent Schrödinger equation is shown in eq. 2.19.⁴⁷

$$\hat{H}\Psi = E\Psi \quad (2.19)$$

The energy of the chemical system is obtained by applying the Hamiltonian operator \hat{H} to the wave function. The Hamilton operator comprises the operators for the kinetic energy \hat{T} and the potential energy \hat{V} together with the electrons and atomic nuclei. For a system with N_C atomic nuclei and N_e electrons, one can formulate the molecular form of the Hamiltonian operator in atomic units and obtain eq. 2.20. In addition, M_I , the ratio between the nuclear mass of atom I and the mass of an electron, and Z_I , the atomic number of atom I, are also included in the equation.

$$\hat{H} = \underbrace{\sum_{i=1}^{N_{el}} \frac{\nabla_i^2}{2}}_{\hat{T}_e} - \underbrace{\sum_{I=1}^{N_C} \frac{\nabla_I^2}{2M_I}}_{\hat{T}_C} - \underbrace{\sum_{i=1}^{N_{el}} \sum_{I=1}^{N_C} \frac{Z_I}{r_{iI}}}_{\hat{V}_{eC}} + \underbrace{\sum_{i<j}^{N_{el}} \frac{1}{r_{ij}}}_{\hat{V}_{ee}} + \underbrace{\sum_{I<J}^{N_C} \frac{Z_I Z_J}{r_{IJ}}}_{\hat{V}_{CC}} \quad (2.20)$$

In equation 2.20, the Nabla operator ∇ is applied. The definition of the square of the Nabla operator is shown in eq. 2.21. The Nabla operator is a derivative operator yielding the derivative when applied to a function, where ∇^2 corresponds to the operator of the second derivative. Also, in eq. 2.20, \hat{T}_e and \hat{T}_C stand for the kinetic energy operators of the electrons and the atomic nuclei, respectively. Whereas \hat{V}_{ee} , \hat{V}_{CC} and \hat{V}_{eC} are the operators for the potential energy between electron-electron, nucleus-nucleus, and electron-nucleus interactions.

$$\nabla_i^2 = \left(\frac{\partial^2}{\partial x_i^2} + \frac{\partial^2}{\partial y_i^2} + \frac{\partial^2}{\partial z_i^2} \right) \quad (2.21)$$

Since protons and neutrons are almost two thousand times heavier than electrons, the motion of atomic nuclei is much slower than that of electrons. For this reason, the nuclear motion can be neglected in a first approximation. This fundamental approximation in quantum chemistry, based on the nuclei's inertia is called the Born-Oppenheimer approximation.⁴⁸⁻⁵⁰ By omitting the nuclear motion, the kinetic energy of the nuclei \hat{T}_C also becomes zero and therefore no longer needs to be calculated. The nucleus-nucleus repulsion becomes a constant, which has to be calculated only once for a given system of atomic nuclei. For this reason, the term \hat{V}_{CC} will be neglected in the following discussion of the derivation of the Hartree-Fock equations. Instead, an electronic Hamiltonian operator \hat{H}_{el} is defined eq. 2.22.⁵¹

$$\hat{H}_{el} = \hat{T}_e + \hat{V}_{ee} + \hat{V}_{eC} \quad (2.22)$$

If the Schrödinger equation from eq. 2.19 is solved by the application of the electronic Hamiltonian operator, only the electronic energy is obtained. If the total energy E_{tot} is to be calculated, the

constant energy of the Coulomb repulsion \hat{V}_{CC} must be re-added to the electronic energy obtained from the Schrödinger equation, cf. eq. 2.23

$$E_{tot} = E_{el} + \hat{V}_{CC} \quad (2.23)$$

Likewise, a suitable wave function must be present to solve the Schrödinger equation. This is mostly unknown. Only for one-electron systems, like hydrogen, the wave function is known. Therefore, a wave function must be constructed for systems with more electrons, composed of several wave functions for each electron. Douglas Rayner Hartree provided an approach to solve this problem. He formulated a multi-electron wave function with N electrons. This was called the Hartree product, see eq. 2.24. In the Hartree product, the wave function ψ^{HP} is defined as the product of all the single-particle wave functions $\phi_i(\vec{r}_i)$ involved in the system. Here, the single-particle wave function is composed of the respective electron ϕ_i at position \vec{r}_i .⁵²⁻⁵⁴

$$\psi^{HP} = \prod_{i=1}^N \phi_i(\vec{r}_i) \quad (2.24)$$

However, the construction of the Hartree product has the weakness that it does not satisfy nor the antisymmetric of the wave function, the Pauli principle, or the indistinguishability of electrons. Therefore, the Slater determinant ψ^{SD} was introduced.⁵⁵ It provides a much better approach to the treatment of multi-electron systems since, in the Slater determinant, each electron is inserted into each one-electron orbital the same number of times, i.e. $((N - 1)!)$ -times.

$$\langle \psi | \psi \rangle \stackrel{!}{=} 1 \quad (2.25)$$

The multi-electron wave function is also normalized to 1, eq. 2.25, resulting in the prefactor $\frac{1}{\sqrt{N!}}$, eq. 2.26 for the Slater determinant. The orbitals $\phi_a(i)$ in eq. 2.26 are spin orbitals, i.e. one-electron orbitals. These spin orbitals are the product of a position function φ and the spin function η . The spin function can take the values α and β , spin up and spin down, respectively. A requirement for the spin-orbital is that these spin orbitals are orthonormal.

$$\psi^{SD}(1, 2, \dots, N) = \frac{1}{\sqrt{N!}} \begin{pmatrix} \phi_1(1) & \phi_2(1) & \cdots & \phi_N(1) \\ \phi_1(2) & \phi_2(2) & \cdots & \phi_N(2) \\ \vdots & \vdots & \ddots & \vdots \\ \phi_1(N) & \phi_2(N) & \cdots & \phi_N(N) \end{pmatrix} \quad (2.26)$$

The Pauli principle is fulfilled because the interchange of two electrons equals the interchange of two lines in the Slater determinant. If within the determinant two electrons are completely equal in all four quantum numbers, then consequently two columns of the determinant are equal and the Slater determinant becomes zero, this fulfills the Pauli exclusion principle.⁵⁶ Moreover, all electrons are now indistinguishable because they can be exchanged arbitrarily within the determinant without changing the observable of the Slater determinant itself.⁴⁶ Since the Schrödinger equation is itself an eigenvalue equation, but the Slater determinant is not an eigenfunction of the Hamilton operator,

the energy must be calculated via the expectancy value, cf. eq. 2.27.

$$E_{el} = \langle \psi^{SD} | \hat{H}_{el} | \psi^{SD} \rangle \quad (2.27)$$

The electronic Hamiltonian operator can be divided into two terms. A one-electron term in which only one electron is involved at a time. This includes the operator of the kinetic energy of the electrons \hat{T}_e and the operator of the nucleus-electron interaction \hat{V}_{eC} . On the contrary, operators are summarized in terms of which two-electrons are involved in the two-electron operator. The one-electron operator \hat{h}_i is calculated according to eq. 2.28. The operator \hat{h}_i acts only on the corresponding electron i . This has the consequence that separating the orbitals according to their electron coordinates is possible.

$$\hat{h}_i = \underbrace{-\frac{\nabla_i^2}{2}}_{\hat{T}_e} - \underbrace{\sum_{I=1}^{N_C} \frac{Z_I}{r_{iI}}}_{\hat{V}_{eC}} \quad (2.28)$$

Since the one-electron operator acts only on specific orbitals, it is irrelevant whether the Hartree product or the Slater determinant is used. However, with the two-electron operator, this leads to a difference since the orbitals are permuted with the Slater determinant. Therefore, the permutation operator $\hat{P}_{i,j}$ results, which swaps the electrons in the orbitals i and j . Supposing the permutation operator is applied to the one-electron integral. In that case, the terms of the swapped orbitals are omitted because they are orthogonal to each other, so the integral value is 0. However, if the permutation operator is applied to the two-electron term V_{ee} , additional terms are obtained, which are not omitted. These terms describe the interaction of the two electrons and named the Coulomb term J_{ij} and the exchange term K_{ij} . The Coulomb term can be interpreted analogously to classical mechanics as the Coulomb repulsion of two charged particles, whereas there is no classical analog for the exchange term. Using the one- and two-electron terms to describe the electronic energy, we obtain equation 2.29.

$$E_{el} = \langle \psi^{SD} | \hat{H}_{el} | \psi^{SD} \rangle = \sum_{i=1}^N \hat{h}_i + \sum_{i=1}^N \sum_{j>1}^N (J_{ij} - K_{ij}) \quad (2.29)$$

Here, eq. 2.29 is usually formulated as eq. 2.30, since it is assumed that paired electrons with α and β -spin exhibit the same energy. This approach is referred to as *restricted Hartree-Fock* (RHF). Here, the energy of all electrons of α -spin is calculated once, and this value is doubled.

$$E_{el} = \sum_{i=1}^{N/2} 2\hat{h}_i + \sum_{i=1}^{N/2} \sum_{j=1}^{N/2} (2J_{ij} - K_{ij}) \quad (2.30)$$

The next step is to formulate the Fock operator itself. This combines the one- and two-electron operators. The one-electron operator has already been formulated in eq. 2.30. The corresponding operators are to be formulated for the Coulomb and exchange terms. Together with the one-electron operator and the two-electron operators, J_{ij} for the Coulomb operator, and K_{ij} for the exchange

operator, the Fock operator \hat{f}_i itself can be formulated, cf. eq. 2.31.

$$\hat{f}_i = \hat{h}_i + \sum_j^{N/2} (2\hat{J}_{ij} - \hat{K}_{ij}) \quad (2.31)$$

The variation principle should be explained before the Fock operator can be used since this shows that the calculated energy of a system can never be smaller or more favorable than the energy of the physical wave function of the electronic ground state, cf. eq. 2.32. Since the exchange term is always a positive scalar, it always corrects the upward value of the energy. Likewise, the Born-Oppenheimer approximation must be mentioned again because neglecting the relativistic effects allows only a precisely calculated energy value within this approximation.

$$E_{el,0}^{min} = \langle \psi^{SD} | \hat{H}_{el} | \psi^{SD} \rangle \geq E_{el,0}^{exact} \quad (2.32)$$

The expected value of the energy corresponds to a function that depends on the wave function of the Slater determinants, cf. eq. 2.26. If the energy takes the minimum value, which corresponds to a minimum, the first derivative of eq. 2.33 must assume 0, cf. eq. 2.34.

$$E_{el,0} [\psi^{SD}] = \langle \psi^{SD} | \hat{H}_{el} | \psi^{SD} \rangle \quad (2.33)$$

$$\frac{d}{d\psi^{SD}} E_{el,0} [\psi^{SD}] = 0 \quad (2.34)$$

This function has been transformed into a sum. For this purpose, the Lagrange multipliers are used. By applying the Lagrange multipliers λ , the Hartree-Fock equation is obtained, cf. 2.35.

$$\hat{f}_i \phi_i = \sum_j^N \lambda_{ij} \phi_j \quad (2.35)$$

Since the Fock operator itself depends on all occupied orbitals as it involves \hat{K} and \hat{J} , cf. 2.31, it is a pseudo-eigenvalue equation. As a consequence, the energy of an orbital can only be calculated if all orbitals involved in the calculation are known. Since this is not the case, the Hartree-Fock method uses an iterative procedure, the so-called self-consistent field (SCF) method. First, the energies of the involved orbitals are guessed as accurately as possible. Then, they are optimized during the SCF procedure until they sufficiently describe the system.^{52-54,57,58}

2.4.2 Configuration Interaction & Coupled Cluster

The HF method yields an energy above the exact value per eq. 2.32. To improve this, the Configuration Interaction (CI) approach captures the correlation energy E_{corr} , the difference between the exact non-relativistic ground state energy $E_{exact,0}$ and the Hartree-Fock ground state energy E_0 , defined in eq. 2.36.^{59,60}

$$E_{corr} = E_{exact,0} - E_0 \quad (2.36)$$

This negative correlation energy is critical for accurately describing chemical bonds. Due to its computational demands, the CI method calculates these energies but is limited to tiny molecules.⁶¹

CI uses multiple Slater determinants instead of one, improving correlation energy. All Slater determinants are needed to account for the correlation, which makes the CI computationally intensive. For medium-sized molecules, CI must truncate early, including only some determinants.^{61,62} This truncated CI lacks size consistency and extensivity, making it inaccurate for larger systems.

The Coupled Cluster (CC) method addresses CI's limitations, ensuring size consistency by summing excitation operators and maintaining higher excitation stages even when truncated.⁶³

2.4.3 Density Functional Theory

Density Functional Theory (DFT) is probably the most widely used computational method in chemistry. In DFT, the upper variable of a system, such as the energy, is not calculated from the wave function, as is the case with Hartree-Fock, Configuration Interaction, or Coupled Cluster, but from the electron density.^{62,63} In 1964, Hohenberg and Kohn established two theorems.⁶⁴ The first theorem states that the energy of a system is determined by its electron density $\rho(\vec{r})$. Thus, there is a one-to-one link between the exact ground state energy and a functional F of the electron density. This function is initially unknown but universal and identical for any system. The second theorem of Hohenberg and Kohn is the validity of the variational principle. The universal functional yields energies for test densities that are either higher than or equal to the exact ground state energy. The function gives the minimum energy only when $\rho(\vec{r})$ is equal to the exact ground state density, cf. 2.37.

$$F[\rho(\vec{r})_{\text{Test}}] \geq E_{\text{exact},0} \quad (2.37)$$

One of the most significant advantages of orbital-free density functional theory over wavefunction-based theories such as Hartree-Fock, Configuration Interaction, and Coupled Cluster is that the energy depends only on the electron density. The associated function is known if this electron density is known. The system's energy can be determined without knowing its wave function, hence the electron density is observable and, therefore, measurable. The second theorem of Hohenberger and Kohn states that the minimum of the electron density functional must be found to determine the ground state energy. Since the electron density has only three spatial coordinates, it is integrated over all electron coordinates, with the differential operator d^3 , except one electron coordinate, cf., eq. 2.38.

$$\rho(\vec{r}_1) = \int |\Psi(\vec{r}_1, \vec{r}_2, \vec{r}_3, \dots, \vec{r}_N)|^2 d^3\vec{r}_2, d^3\vec{r}_3 \dots d^3\vec{r}_N \quad (2.38)$$

The Slater determinant, on the other hand, depends on all electron coordinates, i.e. $3N$ spatial coordinates, or $4N$ if the spin is to be considered. To calculate the system's energy using DFT, only three coordinates are necessary, independent of the number of electrons in the system. Thus the complexity is clearly reduced compared to wave function theories. The energy contributions of the unknown functional can be written analogously to Hartree-Fock, cf. 2.20. It can be written as a sum of functionals, cf. eq. 2.39.

$$F[\rho(\vec{r})] = T_e[\rho] + E_{eN}[\rho] + E_{ee}[\rho] \quad (2.39)$$

$T_e[\rho]$ describes the kinetic energy of the electrons, $E_{eN}[\rho]$ the electron-nucleus attraction and $E_{ee}[\rho]$ the electron-electron interaction. Like in the Hartree-Fock method, the Born-Oppenheimer approximation is also used. Thus, the kinetic energy of the nuclei is neglected, and the nucleus-

nucleus repulsion is assumed to be constant.

$$J[\rho] = \frac{1}{2} \int \int \frac{\rho(\vec{r}_1)\rho(\vec{r}_2)}{|\vec{r}_1 - \vec{r}_2|} d^3\vec{r}_1 d^3\vec{r}_2 \quad (2.40)$$

In addition, analogous to the fock operator from eq. 2.35, the electron-electron interaction $E_{ee}[\rho]$, which implicitly contains the electron correlation, can be split into the Coulomb- $J[\rho]$ and exchange $K[\rho]$ functionals, which can be described by classical equations, cf. eq. 2.40 & eq. 2.41.

$$E_{eN}[\rho] = \sum_{I=1}^{N_N} \int \frac{Z_I \rho(\vec{r}_1)}{|\vec{R}_I - \vec{r}|} d^3\vec{r} \quad (2.41)$$

The description of the kinetic and exchange energy represents the difficulty of the presented orbital-free density functional theory. If one restricts oneself to a uniform electron gas, there is an approach according to Thomas-Fermi, which includes the kinetic energy $T_{TF}[\rho]$, cf. eq. 2.42. The Thomas-Fermi approach was extended by Dirac by a term for the exchange energy $K_D[\rho]$.

$$E_{TFD}[\rho] = T_{TF}[\rho] + E_{eN}[\rho] + J[\rho] + K_D[\rho] \quad (2.42)$$

These calculations can help calculate the electron density for a uniform electron gas. However, this approach does not describe bonds, making application to molecules impossible.

With the approach of Kohn and Sham in 1965, orbitals were introduced again into the density functional theory.⁶⁵ However, this makes the energy again dependent on the electrons in the system, as in the wave function theories. However, Kohn and Sham formulated an expression with which a large part of the kinetic energy could be described, which was impossible with the orbital-free density functional theory. To calculate this energy, Kohn and Sham used a trick. The term for the kinetic energy is split into two parts. The first part is a term which can be calculated exactly, the second part is a correction term. By this splitting, the Hamilton operator can be formulated as in eq. 2.43

$$\hat{H}_\lambda = \hat{T} + \hat{V}_{ext}(\lambda) + \lambda \hat{V}_{ee} \quad \text{with} \quad 0 \leq \lambda \leq 1 \quad (2.43)$$

The term \hat{V}_{ext} describes an external potential in which the electrons move around, where for $\lambda = 1$ the external potential corresponds to \hat{V}_{eN} , where $\lambda = 1$ corresponds to a natural system. If the value for λ varies between 0 and 1, it is assumed that the external potential can be adjusted so that the density ρ remains unchanged and exact. If $\lambda = 0$, the electrons do not interact, and the exact solution can be calculated with a Slater determinant. The Kohn-Sham theory calculates the kinetic energy under the approximation of non-interacting electrons. This energy part is, of course, missing when considering the exact kinetic energy. Therefore, the missing part of the kinetic energy is additionally considered, along with the electron correlation and the exchange energy in the DFT energy calculation, with an additional term. This term has different theories on how they will be calculated. For each theory, there is another function available. The function should cover the need for the calculation and the problem itself.

The different functionals used in DFT can be divided into different classes based on their computational approaches. There are local density approximation (LDA) functionals, generalized gradient approximation (GGA), meta-GGA functionals, hybrid functionals, and double hybrid functionals. They

are all summarized in the Jacobs Ladder and classified according to their quality, cf Tab. 2.1 The LDA

Table 2.1 – Jacobs ladder with the ranking from high to low quality of different functionals for density functional theory.⁶⁶

Ladder level	Assumption	Example
Double hybride	Hartree-Fock, virtuel orbitals, $\nabla^2\rho, \nabla\rho, \rho$	B2BLYP
Hybride	Hartree-Fock, occupied orbitals, $\nabla^2\rho, \nabla\rho, \rho$	B3LYP, PW6B95
meta-GGA	$\nabla^2\rho, \nabla\rho, \rho$	TPSS
GGA	$\nabla\rho, \rho$	PBE, BLYP
LDA	ρ	LDA

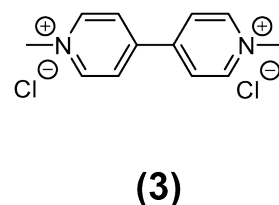
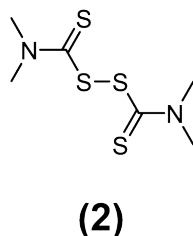
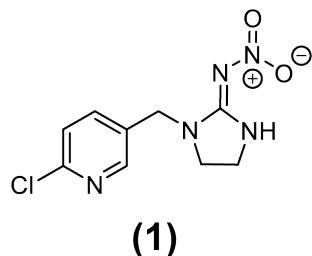
functionals are the simplest and thus qualitatively lowest on Jacob's ladder. The assumption is that the local electron density can be treated as a homogeneous electron gas. Therefore, as mentioned, this function is only suitable for metals but not for molecular systems since bonds cannot be described. The GGA functionals are located on the Jacobs Ladder above the LDA functionals. In addition to the local electron density, they include its derivative. For the calculation of exchange and correlation energies there are different approaches for different functionals, e.g. PBE, BP86 or BLYP.⁶⁷ The choice of the functional has a considerable influence on the result. The GGAs are mainly used for solids and large chemical systems. On the level above the GGAs are the meta-GGAs. The second derivatives of the electron density supplements these functionals. The hybrid functionals follow the meta-GGAs. These form a hybrid approach of LDA or (meta-) GGA functional and Hartree-Fock method. One of these functionals is the widely used B3LYP functional. On the top level of the Jacobs ladder are the double hybrid functionals. They include virtual orbitals and explicit electron correlations in addition to the hybrid functionals.⁶⁸ However, these methods are computationally very extensive and should only be used for very small molecules, like methane.⁶⁹

2.5 State-of-the-Art

This section will first describe the standards of pesticide analysis using conventional methods and then the SERS technique. It will then provide a more detailed description of the different methods and substrates used in SERS technology and explain the current state of the art.

2.5.1 Pesticides

The pesticides imidacloprid (**1**), thiram (**2**) and paraquat (**3**) are used in agriculture with different uses and risks. Imidacloprid is a neonicotinoid insecticide often used to control crop pests. It acts on the insects' nervous system and leads to paralysis and death. Imidacloprid is highly effective against aphids, beetles, and other sucking insects. However, its use is controversial because it can negatively affect bees and pollinators. The application of imidacloprid and other neonicotinoids has been restricted in some regions, including the European Union, due to concerns about bee mortality.⁷⁰ Chemically, imidacloprid comprises a chloropyridine ring, and a pyrazole ring connected via a methylene bridge. A nitroimine group is attached to the pyrazole group. This structure gives imidacloprid the ability to bind to the acetylcholine receptors, similar to nicotine but with a much higher selectivity for insects than mammals.^{71,72}



Thiram is a fungicide and seed treatment that prevents fungal diseases in various crops. Thiram belongs to the class of dithiocarbamates and works by inhibiting the sporulation and growth of fungi. As a systemic pesticide, seeds are often coated with thiram to protect germination and early plant growth. However, thiram can be toxic to humans and animals and should be handled with care. In some countries, the uses of thiram are also regulated, mainly due to its potential health risks.^{73,74} The core of thiram contains a tetraethylthiuram disulfide structure, which is decisive for the fungicidal activity of thiram. The ethylene groups provide chemical stability and bioactive properties. The nitrogen atoms give thiram a specific binding capacity. The interaction of thiram with metal ions can further enhance the fungicidal effect.⁷⁵

Paraquat is a very strong herbicide used for weed control and soil preparation in agriculture. It is a contact herbicide, which means that it quickly kills plants it comes into contact with. It is used in many countries because of its efficiency, but it is controversial due to its high toxicity and the risk of serious damage to health, including fatal poisoning. The handling and use of paraquat require strict safety measures. In many countries, including the European Union, paraquat is banned or severely restricted.⁷⁶ Paraquat is an ionic compound. The chemical structure has a bipyridyl moiety that forms the basic structure of paraquat. The compound of the two pyridine rings is characterized as 1,1'-dimethyl-4,4'-bipyridinium. Paraquat reacts as a dication with a positive charge on the nitrogen on each pyridine ring. This positive charge is crucial for biological activity and toxicity. If paraquat is purchased as a commercial product, chloride is usually used as the counter ion.⁷⁷ The chemical structure of paraquat enables the herbicide to react quickly with the plant tissue, leading to the rapid destruction of the cells. The high toxicity to humans and animals is due to the ability of paraquat to cause oxidative damage, particularly in the lungs and other organs.^{76,78}

2.5.2 Methods of Pesticide Analytics

Various analytical methods exist for detecting pesticides in agriculture and food industry.⁷⁹ Chromatography separates the different analytes in a sample and makes identifying and quantifying specific pesticides possible. Gas chromatography (GC) and high-performance liquid chromatography (HPLC) are the most commonly used methods.⁸⁰⁻⁸⁴

Sample preparation must be carried out for both chromatography methods. In GC, the analyte must be converted to a gaseous state, while in HPLC, the analyte must dissolve in the mobile phase. Mass spectrometry or absorption are commonly used for detection in these chromatographic methods.⁸⁴⁻⁸⁷ The two chromatography methods mentioned are very powerful and can detect a wide range of pesticides in agricultural samples or foodstuffs, offering high sensitivity, precision, and

selectivity. This makes them the preferred methods in the analysis of pesticide residues.^{79,87} Mass spectrometry can help to identify the pesticides based on their exact mass.^{82,86,88} Mass spectrometry also offers very high sensitivity, selectivity, and accuracy in the identification of pesticides.⁸¹

Furthermore, enzymatic and immunological tests are also used to analyze pesticides.⁸⁹ In enzymatic tests, a specific reaction occurs between the enzyme and the pesticide, which triggers a measurable reaction, e.g., color reaction.⁸⁹ They are well suited for preliminary screening analysis of pesticides in agricultural samples. These tests are highly specific and highly sensitive, but they are only suitable for one specific pesticide, whereas other methods such as GC-MS can analyse a broader spectrum of pesticides in a single run.⁹⁰

The immunological test is a test method based on the interaction between specific antibodies and the target pesticides; the test principle follows the lock-and-key model.^{91,92} First, specific antibodies are generated against the target pesticide. This is typically done by immunizing an animal (e.g., a rabbit or a mouse) with the pesticide or a derivatized antigen. The animals then produce antibodies in response to the pesticide.⁹² The most common methods are enzyme-linked immunosorbent assay (ELISA) and lateral flow assays.^{91,93} The results can usually be interpreted quickly and easily, making immunological tests a practical choice for rapidly analyzing pesticide residues. Immunological methods are also fast, inexpensive, and relatively easy to perform on-site. However, as with enzymatic tests, they are less specific and sensitive than chromatographic methods such as GC or HPLC, especially regarding the accurate identification and quantification of pesticides. As a result, they tend to be used for rapid screening.⁹¹

Likewise, with conventional analytical methods for detecting pesticides, appropriate sample preparation is essential, as mentioned before. Sample preparation in pesticide analysis is a critical step that extracts the pesticides from the sample matrix, concentrates them, and prepares them for subsequent analysis.⁷⁹ Different methods can be used for sample preparation depending on the type of sample and the analytical requirements. For example, the pesticides can be extracted using solvents during sample preparation.⁹⁴ This is one of the most common methods and is usually supported by acetonitrile or methanol as a solvent. Solid-phase extraction can also be used.⁸⁵ In this method, the sample is pumped through a column containing a solid sorbent material that selectively retains the pesticides while other matrix components pass through. The pesticides are then eluted from the column and concentrated before being used for analysis.⁹⁴ Analogous to solid phase extraction, there is also the solid phase microextraction method.

In this method, a coated fiber is immersed in the sample, and the pesticides are adsorbed. The fiber is then introduced into the analyzer, where the pesticides are desorbed and analyzed.^{80,95} If pesticides are to be detected in matrices such as milk or meat, the matrix liquefaction method can also be used. In this method, the sample is treated with an enzyme that decomposes the matrix and facilitates the release of the pesticides.⁹⁵ Another standard method is the Quick, Easy, Cheap, Effective, Rugged, Safe (QuEChERS) method.^{81,83,84} QuEChERS method combines extraction and separation and is often used to analyze pesticide residues in fruit, vegetables, and other foods.⁸⁴ The sample is extracted with a solvent and then treated with a mixture of salts and sorbent materials to remove unwanted components and concentrate the pesticides.⁸³ Each method is time-consuming and costly and requires specially trained laboratory staff.⁹⁰

Since around 2015, the SERS technique has been increasingly used in the environmental sector in pesticide analysis.^{96,97} The use of the SERS technique drastically improves sensitivity compared to

Raman spectroscopy. This enables the detection of pesticide residues in deficient concentrations, even in the parts per billion (ppb) or parts per trillion (ppt) range. SERS offers high selectivity as the Raman signals of analyte molecules can be identified based on their characteristic spectral fingerprints. This enables accurate identification of specific pesticides in complex sample mixtures. SERS allows the simultaneous detection of multiple pesticides in a single sample.⁹⁸ By using different metallic substrates or multifunctional nanoparticles, several target molecules can be detected simultaneously, making the analysis more efficient. For example, the SERS technique can be implemented in compact devices, allowing for portable use in the field or food laboratories.⁹⁹ This offers the possibility of quick and easy monitoring of pesticide residues without time-consuming sample preparation. Advances in the production of SERS substrates have led to improved reproducibility, resulting in more reliable and consistent results. Overall, SERS is revolutionizing the detection method of pesticides through its increased sensitivity, selectivity, and the possibility of multiplex analysis. Integrating this technology into agricultural practice allows pesticide residues to be monitored and controlled more effectively, improving food safety and environmental protection.⁹⁶

2.5.3 SERS Substrates

The results of the SERS technique depend crucially on the substrates. It should be noted that the term "substrate" may be defined differently in different scientific publications. For example, it can be liquid substrates such as nanoparticle suspensions or solid nanoparticle substrates.⁹⁶

Solid nanoparticle substrates can be divided into flexible and rigid materials. Examples of flexible substrates are cellulose paper, various polymers, or textiles such as cotton or silk. These substrates offer the advantage of being produced inexpensively and being accessible to prepare for measurement. They enable the analysis of a wide range of sample molecules and, due to their flexibility, offer a variety of sampling techniques, such as the simple dabbing of pesticides on fruit or vegetables for on-site detection with a Raman spectrometer.¹⁰⁰

Materials such as glass, silicon, or metal are suitable for rigid substrates on which nanoparticles can be applied. The advantage of these rigid substrates lies in their signal homogeneity, frequent reusability, and a higher amplification factor. The homogeneous and orderly distribution of the particles on the substrates achieves the latter. Although these materials are often recyclable, they are more expensive, an important criterion.¹⁰¹

The following section provides some examples of new SERS substrates. Publications of SERS substrates that can currently be used to detect thiram, paraquat, and imidacloprid are considered. A complete overview of all SERS substrates is not possible within the scope of this work and can also be found in detail in selected review articles.^{4,96,102} Starting with a method by Zhang et al. from 2019 for identifying melamines with a hydrophobic paper-based SERS substrate, which was successfully applied to thiram. Spherical silver nanoparticles prepared from silver nitrate and sodium citrate were used. The filter paper was placed in NaCl and dried to produce the substrates. The dip coating method applied the silver nanoparticles to the filter paper. Due to the hydrophobic properties of the substrates, they can be washed and thus reused. Another advantage in terms of sustainability is that only a few chemicals are required for the nanoparticles and the substrates.¹⁰³ In the somewhat complex metal sputtering method, the substrates are cotton fabric coated with silver. No nanoparticles are used in this method; instead, the substrate base is coated directly with the

SERS-active material. To do this, the cotton must first be cleaned in an ultrasonic bath with acetone. It is then washed with distilled water. The silver can then be applied using a magnetron sputter system. An aqueous solution of thiram is dripped onto the substrate to examine the analytes.^{104,105} It is also possible to produce SERS substrates from nanoparticles of several precious metals. Hussain et al. have developed such a bimetallic substrate and successfully detected thiram in milk. They first produced gold nanoparticles, which were then coated with a 6 nm thick layer of silver. These encapsulated nanoparticles could be used directly as a SERS substrate. In a further optimization step, the surface of the nanoparticles was modified with mercaptooctane to ensure a longer shelf life through steric stabilization.^{106,107} Bimetallic nanoparticles were also used by Wang et al. for a SERS substrate. Wang et al. also produced gold nanoparticles, which were coated with a silver layer. However, this was not used directly in the solution but applied to a PET film a SERS substrate. Wang et al. used this substrate to detect thiram on apples, tomatoes and cucumbers.¹⁰⁸ Zhang et al. developed a substrate that utilises the charge of pesticide molecules such as paraquat. Tungsten was used in the synthesis to generate spots with tungsten atoms on the nanoparticle surface. These gold nanoparticles are ideal for forming hydrogen bridge bonds, which ensure agglomeration of the nanoparticles and, thus, hot spots. Paraquat, carbendazim, and acetamiprid were successfully detected with these nanoparticles.¹⁰⁹ Bakar et al. used a substrate with nanosilver stars to detect imidacloprid, applying several layers of silver nanostars to the substrate. The silver nanostars were produced by chemical reduction and then arranged into a film by self-assembly of the nanostars. Various bases, such as glass and silicon surfaces, were investigated. The highest amplification was achieved with 10 layers of silver nanostars on glass. The substrate produced by Bakar et al. is also storable and can be used directly on-site in the field.¹¹⁰ Al-Syadi et al. describe the development of a novel SERS substrate based on palladium nanoparticles deposited on a mesoporous silicon layer to detect imidacloprid. The substrate was produced by electrochemical anodisation of a silicon wafer and subsequent immersion coating with palladium nanoparticles. The porous structure of the palladium nanoparticles enables a high surface enlargement, which facilitates the formation of 'hotspots' for strong amplification.¹¹¹

References

1. Raman, C. & Krishnan, K. A New Type of Secondary Radiation. *Nature* **121**, 501–502 (1928).
2. Singh, R. & Riess, F. Sir C. V. Raman and the story of the Nobel prize. *Current Science* **75**, 965–971 (1998).
3. Göpel, W. & Ziegler, C. *Struktur der Materie : Grundlagen, Mikroskopie und Spektroskopie* (Vieweg+Teubner, Stuttgart, 1994).
4. Pilot, R., Signorini, R., Durante, C., *et al.* A Review on Surface-Enhanced Raman Scattering. *Biosensors* **9** (2019).
5. Fleischmann, M., Hendra, P. J. & McQuillan, A. J. Raman spectra of pyridine adsorbed at a silver electrode. *Chemical Physics Letters* **26**, 163–166 (1974).

6. Jeanmaire, D. L. & Van Duyne, R. P. Surface raman spectroelectrochemistry: Part I. Heterocyclic, aromatic, and aliphatic amines adsorbed on the anodized silver electrode. *Journal of Electroanalytical Chemistry and Interfacial Electrochemistry* **84**, 1–20 (1977).
7. Albrecht, M. G. & Creighton, J. A. Anomalously intense Raman spectra of pyridine at a silver electrode. *Journal of the American Chemical Society* **99**, 5215–5217 (1977).
8. Moskovits, M. Surface roughness and the enhanced intensity of Raman scattering by molecules adsorbed on metals. *The Journal of Chemical Physics* **69**, 4159–4161 (1978).
9. Moskovits, M. Surface-enhanced Raman spectroscopy: a brief retrospective. *Journal of Raman Spectroscopy* **36**, 485–496 (2005).
10. Otto, A. The 'chemical'(electronic) contribution to surface-enhanced Raman scattering. *Journal of Raman Spectroscopy* **36**, 497–509 (2005).
11. Etchegoin, P. G. & Le Ru, E. C. A perspective on single molecule SERS: current status and future challenges. *Physical Chemistry Chemical Physics* **10**, 6079–6089 (2008).
12. Le Ru, E. C., Galloway, C. & Etchegoin, P. G. On the connection between optical absorption/extinction and SERS enhancements. *Physical Chemistry Chemical Physics* **8**, 3083–3087 (2006).
13. Bantz, K. C., Meyer, A. F., Wittenberg, N. J., *et al.* Recent progress in SERS biosensing. *Physical Chemistry Chemical Physics* **13**, 11551–11567 (2011).
14. Dick, L. A., McFarland, A. D., Haynes, C. L. & Van Duyne, R. P. Metal Film over Nanosphere (MFON) Electrodes for Surface-Enhanced Raman Spectroscopy (SERS): Improvements in Surface Nanostructure Stability and Suppression of Irreversible Loss. *The Journal of Physical Chemistry B* **106**, 853–860 (2002).
15. Joseph, V. *Nanopartikel auf Oberflächen* PhD Thesis, Humboldt-Universität zu Berlin, Mathematisch - Naturwissenschaftliche Fakultät I, Berlin (2012).
16. Mie, G. Beiträge zur Optik trüber Medien, speziell kolloidaler Metallösungen. *Annalen der Physik* **330**, 377–445 (1908).
17. Creighton, J. A. Surface raman electromagnetic enhancement factors for molecules at the surface of small isolated metal spheres: The determination of adsorbate orientation from sers relative intensities. *Surface Science* **124**, 209–219 (1983).
18. Metiu, H. & Das, P. The Electromagnetic Theory of Surface Enhanced Spectroscopy. *Annual Review of Physical Chemistry* **35**, 507–536 (1984).
19. Kerker M Wang DS, C. H. Surface enhanced Raman scattering (SERS) by molecules adsorbed at spherical particles. *Applied Optics* **10**, 3373–3388 (1980).
20. Kerker, M., Siiman, O. & Wang, D. S. Effect of aggregates on extinction and surface-enhanced Raman scattering spectra of colloidal silver. *The Journal of Physical Chemistry* **88**, 3168–3170 (1984).
21. Feynman, R. There's plenty of room at the bottom. *Engineering and Science* **23**, 22–36 (1960).

22. Barrak, H., Saied, T., Chevallier, P., *et al.* Synthesis, characterization, and functionalization of ZnO nanoparticles by N-(trimethoxysilylpropyl) ethylenediamine triacetic acid (TMSEDTA): Investigation of the interactions between Phloroglucinol and ZnO@TMSEDTA. *Arabian Journal of Chemistry* **12**, 4340–4347 (2019).
23. Lee, J. E., Lee, N., Kim, T., Kim, J. & Hyeon, T. Multifunctional mesoporous silica nanocomposite nanoparticles for theranostic applications. *Accounts of Chemical Research* **44**, 893–902 (2011).
24. Mansha, M., Qurashi, A., Ullah, N., *et al.* Synthesis of In₂O₃/graphene heterostructure and their hydrogen gas sensing properties. *Ceramics International* **42**, 11490–11495 (2016).
25. Ganesh, M., Hemalatha, P., Peng, M. M. & Jang, H. T. One pot synthesized Li, Zr doped porous silica nanoparticle for low temperature CO₂ adsorption. *Arabian Journal of Chemistry* **10**, S1501–S1505 (2017).
26. Shaalan, M., Saleh, M., El-Mahdy, M. & El-Matbouli, M. Recent progress in applications of nanoparticles in fish medicine: A review. *Nanomedicine: Nanotechnology, Biology, and Medicine* **12**, 701–710 (2016).
27. Dreaden, E. C., Alkilany, A. M., Huang, X., Murphy, C. J. & El-Sayed, M. A. The golden age: Gold nanoparticles for biomedicine. *Chemical Society Reviews* **41**, 2740–2779 (2012).
28. Khan, I., Saeed, K. & Khan, I. Nanoparticles: Properties, applications and toxicities. *Arabian Journal of Chemistry* **12**, 908–931 (2019).
29. Ealias, A. M. & Saravanakumar, M. P. A review on the classification, characterisation, synthesis of nanoparticles and their application. *IOP Conference Series: Materials Science and Engineering* **263**, 032019 (2017).
30. Abou El-Nour, K. M., Eftaiha, A., Al-Warthan, A. & Ammar, R. A. Synthesis and applications of silver nanoparticles. *Arabian Journal of Chemistry* **3**, 135–140 (2010).
31. Martin H. Magnusson , Knut Deppert , Jan-Olle Malm , Jan-Olov Bovin. Gold Nanoparticles: Production, Reshaping, and Thermal Charging. *Journal of Nanoparticle Research* **1**, 243–251 (1999).
32. Abhijit S. Gurav , Toivo T. Kodas , Lu-Min Wang , Esko I. Kauppinen , Jorma Joutsensaari. Generation of nanometer-size fullerene particles via vapor condensation. *Chemical Physics Letters* **218**, 304–308 (1994).
33. Semaltianos, N. G. Nanoparticles by Laser Ablation. *Critical Reviews in Solid State and Materials Sciences* **35**, 105–124 (2010).
34. Navaladian, S., Viswanathan, B., Viswanath, R. & Varadarajan, T. Thermal decomposition as route for silver nanoparticles. *Nanoscale research letters* **2**, 44–48 (2006).
35. Dong, J., Carpinone, P. L., Pyrgiotakis, G., Demokritou, P. & Moudgil, B. M. Synthesis of Precision Gold Nanoparticles Using Turkevich Method. *Kona : powder science and technology in Japan* **37**, 224–232 (2020).
36. Targeted nanoparticles for drug delivery through the blood-brain barrier for Alzheimer's disease. *Journal of controlled release : official journal of the Controlled Release Society* **108**, 193–214 (2005).

37. Morton, S. M., Silverstein, D. W. & Jensen, L. Theoretical studies of plasmonics using electronic structure methods. *Chemical reviews* **111**, 3962–3994 (2011).
38. Dahman, Y. *Nanotechnology and functional materials for engineers* (Elsevier, 2017).
39. Park, J.-W. & Shumaker-Parry, J. S. Structural Study of Citrate Layers on Gold Nanoparticles: Role of Intermolecular Interactions in Stabilizing Nanoparticles. *Journal of the American Chemical Society* **136**, 1907–1921 (2014).
40. Derjaguin, B., Churaev, N., Muller, V., *et al.* The Derjaguin - Landau - Verwey - Overbeek (DLVO) theory of stability of lyophobic colloids. *Surface forces*, 293–310 (1987).
41. Lowry, G. V., Hill, R. J., Harper, S., *et al.* Guidance to improve the scientific value of zeta-potential measurements in nanoEHS. *Environmental Science: Nano* **3**, 953–965 (2016).
42. Zhao, P., Li, N. & Astruc, D. State of the art in gold nanoparticle synthesis. *Coordination Chemistry Reviews* **257**, 638–665 (2013).
43. Ding, S.-Y., Yi, J., Li, J.-F., *et al.* Nanostructure-based plasmon-enhanced Raman spectroscopy for surface analysis of materials. *Nature reviews materials* **1**, 16021 (2016).
44. Aravind, I., Nitzan, A. & Metiu, H. The interaction between electromagnetic resonances and its role in spectroscopic studies of molecules adsorbed on colloidal particles or metal spheres. *Surface Science* **110**, 189–204 (1981).
45. Bubin, S., Pavanello, M., Tung, W.-C., Sharkey, K. L. & Adamowicz, L. Born–Oppenheimer and Non-Born–Oppenheimer, Atomic and Molecular Calculations with Explicitly Correlated Gaussians. *Chemical Reviews* **113**, 36–79 (2013).
46. Simons, J. An experimental chemist's guide to ab initio quantum chemistry. *Journal of Physical Chemistry* **95**, 1017–1029 (1991).
47. Schrödinger, E. Quantisierung als Eigenwertproblem. *Annalen der Physik* **384**, 489–527 (1926).
48. Born, M. & Oppenheimer, R. Zur Quantentheorie der Moleküle. *Annalen der Physik* **389**, 457–484 (1927).
49. Kolos, W. & Wolniewicz, L. Improved Theoretical Ground-State Energy of the Hydrogen Molecule. *Journal of Chemical Physics* **49**, 404–410 (1968).
50. Pack, R. T. & Hirschfelder, J. O. Energy Corrections to the Born–Oppenheimer Approximation. The Best Adiabatic Approximation. *Journal of Chemical Physics* **52**, 521–534 (1970).
51. Nakai, H. Nuclear orbital plus molecular orbital theory: Simultaneous determination of nuclear and electronic wave functions without Born–Oppenheimer approximation. *International Journal of Quantum Chemistry* **107**, 2849–2869 (2007).
52. Hartree, D. R. The Wave Mechanics of an Atom with a Non-Coulomb Central Field. Part I. Theory and Methods. *Mathematical Proceedings of the Cambridge Philosophical Society* **24**, 89–110 (1928).
53. Hartree, D. R. The Wave Mechanics of an Atom with a Non-Coulomb Central Field. Part II. Some Results and Discussion. *Mathematical Proceedings of the Cambridge Philosophical Society* **24**, 111–132 (1928).

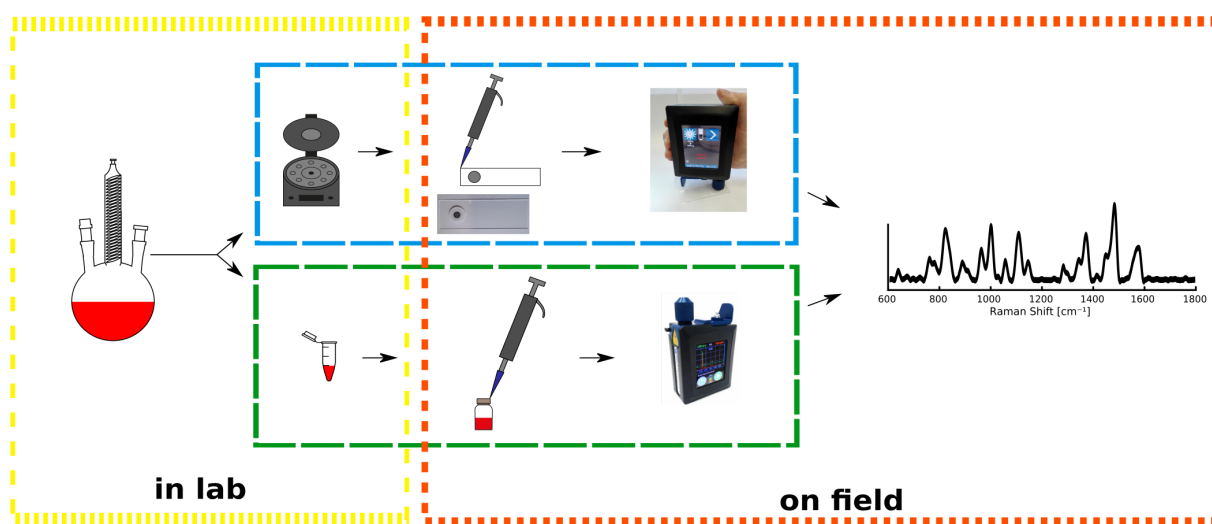
54. Hartree, D. R. The Wave Mechanics of an Atom with a non-Coulomb Central Field. Part III. Term Values and Intensities in Series in Optical Spectra. *Mathematical Proceedings of the Cambridge Philosophical Society* **24**, 426–437 (1928).
55. Slater, J. C. The Theory of Complex Spectra. *Physical Review* **34**, 1293–1322 (1929).
56. Pauli, W. Über den Zusammenhang des Abschlusses der Elektronengruppen im Atom mit der Komplexstruktur der Spektren. *Einführung und Originaltexte* **229**, 765–783 (1925).
57. Fock, V. Näherungsmethode zur Lösung des quantenmechanischen Mehrkörperproblems. *Zeitschrift für Physik* **61**, 126–148 (1930).
58. Mulliken, R. S. Report on notation for the spectra of polyatomic molecules. *The Journal of Chemical Physics* **23**, 1997–2011 (1955).
59. Boys, S. F. Electronic wave functions-I. A general method of calculation for the stationary states of any molecular system. *Proceedings of the Royal Society of London. Series A. Mathematical and Physical Sciences* **200**, 542–554 (1950).
60. Dykstra, C. E. *Advanced theories and computational approaches to the electronic structure of molecules* (Springer Science & Business Media, 2012).
61. Koch, W. & Holthausen, M. C. *A chemist's guide to density functional theory* (John Wiley & Sons, 2015).
62. Jensen, F. *Introduction to computational chemistry* (John Wiley & Sons, 2017).
63. Cramer, C. J. *Essentials of computational chemistry: theories and models* (John Wiley & Sons, 2013).
64. Hohenberg, P. & Kohn, W. Inhomogeneous Electron Gas. *Physical Review* **136**, B864–B871 (1964).
65. Kohn, W. & Sham, L. J. Self-Consistent Equations Including Exchange and Correlation Effects. *Physical Review* **140**, A1133–A1138 (1965).
66. Van Doren, V. E., Van Alsenoy, C. & Geerlings, P. *Density functional theory and its application to materials* (Melville, N.Y., 2001).
67. Lathiotakis, N., Helbig, N., Zacarias, A. & Gross, E. A functional of the one-body-reduced density matrix derived from the homogeneous electron gas: Performance for finite systems. *The Journal of Chemical Physics* **130**, 064109 (2009).
68. Tran, F., Stelzl, J. & Blaha, P. Rungs 1 to 4 of DFT Jacob's ladder: Extensive test on the lattice constant, bulk modulus, and cohesive energy of solids. *The Journal of Chemical Physics* **144**, 204120 (2016).
69. Grimme, S. Density functional theory with London dispersion corrections. *Wiley Interdisciplinary Reviews: Computational Molecular Science* **1**, 211–228 (2011).
70. Suchail, S., Guez, D. & Belzunces, L. P. Characteristics of imidacloprid toxicity in two *Apis mellifera* subspecies. *Environmental Toxicology and Chemistry: An International Journal* **19**, 1901–1905 (2000).
71. Bal, R., Türk, G., Tuzcu, M., *et al.* Assessment of imidacloprid toxicity on reproductive organ system of adult male rats. *Journal of Environmental Science and Health, Part B* **47**, 434–444 (2012).

72. Yang, C., Fang, S., Tsai, H., Chen, J. & Liu, Y. Newly prepared surface-enhanced Raman scattering-active substrates for sensing pesticides. *Journal of Electroanalytical Chemistry* **861**, 113965 (2020).
73. Liu, K., Li, Y., Iqbal, M., Tang, Z. & Zhang, H. Thiram exposure in environment: A critical review on cytotoxicity. *Chemosphere* **295**, 133928 (2022).
74. Maita, K., Tsuda, S. & Shirasu, Y. Chronic toxicity studies with thiram in Wistar rats and beagle dogs. *Toxicological Sciences* **16**, 667–686 (1991).
75. Cereser, C., Boget, S., Parvaz, P. & Revol, A. An evaluation of thiram toxicity on cultured human skin fibroblasts. *Toxicology* **162**, 89–101 (2001).
76. Böger, P. & Kunert, K. Phytotoxic action of paraquat on the photosynthetic apparatus. *Zeitschrift für Naturforschung C* **33**, 688–694 (1978).
77. Smith, P., Heath, D. & Fishman, A. P. Paraquat. *CRC critical reviews in toxicology* **4**, 411–445 (1976).
78. McCormack, A. L., Atienza, J. G., Johnston, L. C., *et al.* Role of oxidative stress in paraquat-induced dopaminergic cell degeneration. *Journal of neurochemistry* **93**, 1030–1037 (2005).
79. Carvalho, F. P. Pesticides, environment, and food safety. *Food and Energy Security* **6**, 48–60 (2017).
80. Abdulrauf, L. B. & Tan, G. H. Chemometric approach to the optimization of HS-SPME/GC–MS for the determination of multiclass pesticide residues in fruits and vegetables. *Food Chemistry* **177**, 267–273 (2015).
81. Andrade, G. C. R. M., Monteiro, S. H., Francisco, J. G., *et al.* Liquid chromatography–electrospray ionization tandem mass spectrometry and dynamic multiple reaction monitoring method for determining multiple pesticide residues in tomato. *Food Chemistry* **175**, 57–65 (2015).
82. Bakirci Gozde, T. & Hicil, Y. Fast and simple extraction of pesticide residues in selected fruits and vegetables using tetrafluoroethane and toluene followed by ultrahigh-performance liquid chromatography/tandem mass spectrometry. *Food Chemistry* **135**, 1901–1913 (2012).
83. Carneiro, R. P., Oliveira, F. A. S., Madureira, F. D., *et al.* Development and method validation for determination of 128 pesticides in bananas by modified QuEChERS and UHPLC–MS/MS analysis. *Food Control* **33**, 413–423 (2013).
84. Chamkasem, N., Ollis, L. W., Harmon, T., Lee, S. & Mercer, G. Analysis of 136 Pesticides in Avocado Using a Modified QuEChERS Method with LC-MS/MS and GC-MS/MS. *Journal of Agricultural and Food Chemistry* **61**, 2315–2329 (2013).
85. Balinova, A., Mladenova, R. & Shtereva, D. Solid-phase extraction on sorbents of different retention mechanisms followed by determination by gas chromatography–mass spectrometric and gas chromatography–electron capture detection of pesticide residues in crops. *Journal of Chromatography A* **1150**, 136–144 (2007).
86. Cervera, M. I., Portoles, T., Pitarch, E., Beltran, J. & Hernandez, F. Application of gas chromatography time-of-flight mass spectrometry for target and non-target analysis of pesticide residues in fruits and vegetables. *Journal of Chromatography A* **1244**, 168–177 (2012).

87. Abd Al-Rahman, S. H., Almaz, M. M. & Osama, I. A. Determination of Degradation Rate of Acaricide Fenpyroximate in Apple, Citrus, and Grape by HPLC-DAD. *Food Analytical Methods* **5**, 306–311 (2012).
88. Gilbert-Lopez, B., Garcia-Reyes, J. F., Fernandez-Alba, A. R. & Molina-Diaz, A. Evaluation of two sample treatment methodologies for large-scale pesticide residue analysis in olive oil by fast liquid chromatography–electrospray mass spectrometry. *Journal of Chromatography A* **1217**, 3736–3747 (2010).
89. Caetano, J. & Machado, S. A. S. Determination of carbaryl in tomato in natura using an amperometric biosensor based on the inhibition of acetylcholinesterase activity. *Sensors and Actuators B: Chemical* **129**, 40–46 (2008).
90. Narendaran, S. T., Meyyanathan, S. N. & Babu, B. Review of pesticide residue analysis in fruits and vegetables. Pre-treatment, extraction and detection techniques. *Food Research International* **133**, 109141 (2020).
91. Gascon, J., Oubina, A. & Barcelo, D. Detection of endocrine-disrupting pesticides by enzyme-linked immunosorbent assay (ELISA): application to atrazine. *Trends in Analytical Chemistry* **16**, 554–562 (1997).
92. Chaudhary, V., Kumar, M., Chauhan, C., *et al.* Strategies for mitigation of pesticides from the environment through alternative approaches: A review of recent developments and future prospects. *Journal of Environmental Management* **354**, 120326 (2024).
93. Octobre, G., Delprat, N., Doumeche, B. & Leca-Bouvier, B. Herbicide detection: A review of enzyme- and cell-based biosensors. *Environmental Research* **249**, 118330 (2024).
94. Aysal, P., Ambrus, A., Lehotay, S. J. & Cannavan, A. Validation of an efficient method for the determination of pesticide residues in fruits and vegetables using ethyl acetate for extraction. *Journal of Environmental Science and Health, Part B* **42**, 481–490 (2007).
95. Arthur, C. L. & Pawliszyn, J. Solid phase microextraction with thermal desorption using fused silica optical fibers. *Analytical Chemistry* **62**, 2145–2148 (1990).
96. Xu, M.-L., Gao, Y., Han, X. X. & Zhao, B. Detection of Pesticide Residues in Food Using Surface-Enhanced Raman Spectroscopy: A Review. *Journal of Agricultural and Food Chemistry* **65**, 6719–6726 (2017).
97. Sharma, S., Kolavinac, S., Jiang, X., *et al.* Raman Spectroscopy-Based Chemometrics for Pesticide Residue Detection: Current Approaches and Future Challenges. *ACS Agricultural Science & Technology* **4**, 389–404 (2024).
98. Xu, R., Dai, S., Dou, M., *et al.* Simultaneous, Label-Free and High-throughput SERS Detection of Multiple Pesticides on Ag@Three-Dimensional Silica Photonic Microsphere Array. *Journal of Agricultural and Food Chemistry* **71**, 3050–3059 (2023).
99. Wang, Y., Wang, Z., Chen, C., *et al.* Fabrication of Flexible Pyramid Array as SERS Substrate for Direct Sampling and Reproducible Detection. *Analytical Chemistry* **95**, 14184–14191 (2023).
100. Fateixa, S., Pinheiro, P. C., Nogueira, H. I. & Trindade, T. Gold loaded textile fibres as substrates for SERS detection. *Journal of Molecular Structure* **1185**, 333–340 (2019).

101. Bharati, M. S. S. & Soma, V. R. Flexible SERS substrates for hazardous materials detection: recent advances. *Opto-Electron Advances* **4**, 210048 (2021).
102. Pang, S., Yang, T. & He, L. Review of surface enhanced Raman spectroscopic (SERS) detection of synthetic chemical pesticides. *Trends in Analytical Chemistry* **85**, 73–82 (2016).
103. Zhang, C., You, T., Yang, N., *et al.* Hydrophobic paper-based SERS platform for direct-droplet quantitative determination of melamine. *Food chemistry* **287**, 363–368 (2019).
104. Zhang, Z., Si, T., Liu, J. & Zhou, G. In-Situ Grown Silver Nanoparticles on Nonwoven Fabrics Based on Mussel-Inspired Polydopamine for Highly Sensitive SERS Carbaryl Pesticides Detection. *Nanomaterials* **9**, 1–12 (2019).
105. Gao, W., Xu, J., Cheng, C., Qiu, S. & Jiang, S. Rapid and highly sensitive SERS detection of fungicide based on flexible wash free metallic textile. *Applied Surface Science* **512**, 144693 (2020).
106. Hussain, A., Sun, D.-W. & Pu, H. Bimetallic core shelled nanoparticles (Au@AgNPs) for rapid detection of thiram and dicyandiamide contaminants in liquid milk using SERS. *Food chemistry* **317**, 126429 (2020).
107. Hussain, N., Pu, H. & Sun, D.-W. Core size optimized silver coated gold nanoparticles for rapid screening of tricyclazole and thiram residues in pear extracts using SERS. *Food chemistry* **350**, 129025 (2021).
108. Wang, K., Sun, D.-W., Pu, H. & Wei, Q. Polymer multilayers enabled stable and flexible Au@Ag nanoparticle array for nondestructive SERS detection of pesticide residues. *Talanta* **223**, 121782 (2021).
109. Zhang, Q., Chen, B., Ma, Q., *et al.* Single-atom oxide-decorated AuNPs for universal enhancement in SERS detection of pesticide residues. *Analytica Chimica Acta*, 343192 (2024).
110. Abu Bakar, N. & Shapter, J. G. Silver nanostar films for surface-enhanced Raman spectroscopy (SERS) of the pesticide imidacloprid. *Heliyon* **9** (2023).
111. Al-Syadi, A. M., Faisal, M., Harraz, F. A., Jalalah, M. & Alsaiari, M. Immersion-plated palladium nanoparticles onto meso-porous silicon layer as novel SERS substrate for sensitive detection of imidacloprid pesticide. *Scientific Reports* **11**, 9174 (2021).

3 In-Field Detection Method for Imidacloprid by Surface-Enhanced Raman Spectroscopy



Chapter 3 is reproduced from *Andrea Hermsen, David Lamers, Justus Schoettl, Christian Mayer & Martin Jaeger (2022) In-Field Detection Method for Imidacloprid by Surface Enhanced Raman Spectroscopy, Toxicological & Environmental Chemistry, DOI: 10.1080/02772248.2021.1991929* with permission from Taylor and Francis.

3.1 Abstract

Neonicotinoids such as imidacloprid are used in agriculture worldwide. Due to their hazardous potential, their occurrence is monitored. For pesticide identification in environmental samples, the major tool, high performance liquid chromatography coupled with mass spectrometry, is not fit for field monitoring due to instrument size and technical requirements. To overcome this disadvantage, a method for fast on-site identification of imidacloprid was developed using a handheld Raman spectrometer and surface enhanced Raman spectroscopy. As enhancing agents, gold nanoparticles in solution and on textile support were compared for easy, fast and sensitive monitoring. Agglomeration of nanoparticles led to further signal enhancement. Several agglomeration reagents, filter paper and non-woven polylactide as substrates were tested for optimum enhancement. Addition of hydrochloric acid provided best amplification of imidacloprid signals in solution, while PLA as solid support yielded best sensitivity. Both the solution and solid support methods were estimated to be sufficiently sensitive for fieldable pesticide identification, which may precede standard laboratory analysis. Based on spectral analysis, a proposal for the imidacloprid-gold surface geometry was derived.

3.2 Introduction

Pesticides, their degradation products, and their bound residues represent a major problem for the global environment despite of their benefits. Increasing food production due to an ever-growing world population and the need for extensive use of pesticides in the agricultural economy lead to the occurrence of pesticides in human nutrition.¹ They eventually affect human health.²

As a consequence, food safety and environmental protection in agriculture have been and still are heavily discussed and are seen as research topics of major importance.³ In the early 1990s, neonicotinoids were launched as systemic insecticides to the global market. Imidacloprid is one of the major neonicotinoid compounds which represents one third of the market for insecticides worldwide.⁴ Despite of their relatively low toxicity in ecotoxicological assays, neonicotinoids and especially imidacloprid are suspected of being harmful to pollinators like honey bees and bumble bees.⁵ Increasingly, studies show adverse effects with respect to bees and bio diversity in general.⁴ Another danger originates from pesticide allurements. Bees were observed to prefer a field treated with a pesticide after previous exposure. In an analogous study, bees were drawn to a sucrose solution containing neonicotinoids rather than to a mere sucrose solution.⁶

The flight routes of bees were also found to be affected. After exposure to neonicotinoids, bees died since they were unable to navigate to their colony.⁷ In a long-term study, pesticides were detected in honey, which must be considered as a major food safety issue and a substantial risk to human health.⁸

Scientific studies and surveys point out the urge for monitoring the use of pesticides and their residues with respect to environmental concerns and food safety.⁹ As the two most common methods, gas chromatography-mass spectrometry (GC-MS) and liquid chromatography-mass spectrometry (LC-MS) have established themselves as major tools for pesticide identification and quantification.¹⁰ Chromatographic analysis of pesticides usually takes between 5 and 10 minutes, but may also exceed 30 min in case of GC.¹¹ In addition, the sample preparation is extremely important for sensitivity purposes. The most common method is the so-called "Quick, Easy, Cheap, Effective, Rugged, Safe" (QuEChERS) method, which has been introduced by Anastassiades et al.¹² When monitoring larger areas, the application of QuEChERS becomes time-consuming and costly. The use of a wide-area survey with sample preparation and LC- or GC-MS analysis is only feasible for random sampling at a limited number of test spots. Furthermore, well-trained laboratory personnel are required. Sample preparation has a strong impact on overall method sensitivity. In contrast, surface enhanced Raman spectroscopy (SERS) provides a fast, easy-to-use and fieldable methodology for the sensitive and selective detection of drugs and pesticides.¹³⁻¹⁶ Technological advances in this field have made it possible to use SERS in environmental and food safety for pesticide detection.¹⁷ Ever since the first SERS spectra of pesticides were reported in the late 1980s, a variety of applications has been demonstrated.¹⁸ Various types of spectrometer setups are known, ranging from Raman microscopes to portable instruments.^{19,20} Based on Raman spectroscopy, SERS takes advantage of the signal amplification caused by nanoparticles either in solution or immobilized on solid supports.^{21,22} Suitable nanoparticles, such as gold or silver nanoparticles, possess surface plasmons whose absorption range coincides with the wavelength of the laser used for Raman excitation. Resulting signal amplifications of up to 14 to 15 orders of magnitude have been described. This allows the use of less powerful handheld instruments with lower resolution and laser power directly on the field.²³ For reproducible and sensitive analyses, the morphology of the nanoparticles needs to be as uniform as possible.²⁴ The signal enhancement is based on the electromagnetic (EM) and the chemical (CM) effect.²⁵ The EM effect originates from the interaction of light with the surface of the nanoparticle. It strongly depends on the distance but does not require interaction between molecule and nanoparticle. The CM effect depends on the interaction, e.g. covalent or coordinative binding or charge-transfer, hence on the type of molecule and originates from the change of its polarizability.²⁶ Major advantages of SERS are inexpensive, fast analyses, since no complex sample preparation and no highly trained personnel are required.

In this study, we developed a workflow to prepare agglomerated nanoparticles in solution and on PLA substrates to record SERS spectra of imidacloprid using a handheld Raman spectrometer. We compared four agglomeration procedures using salts and acids and two suitable support varieties to ensure signal enhancement. We proposed the molecular arrangement of the analyte on the gold nanospheres (GNS). Eventually we estimated the amount of imidacloprid to be expected in a field and compared it to the limit of detection of the SERS methods.

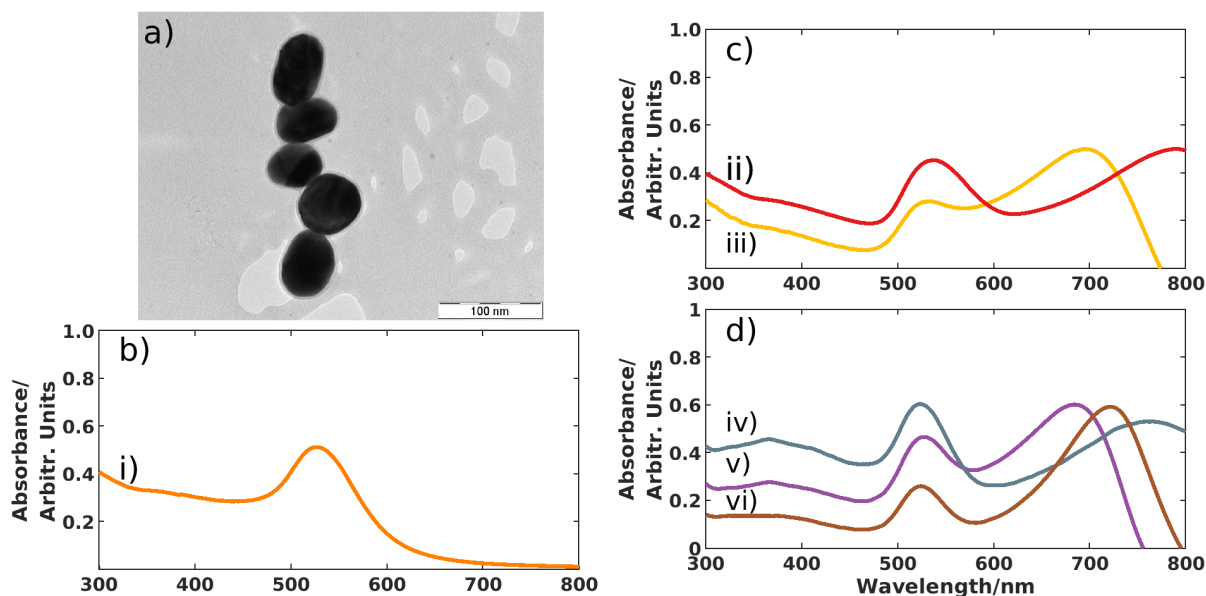


Figure 3.1 – TEM image and absorption spectra of GNS synthesized using a modified Turkevich method. (a) TEM image of GNS of 40 nm diameter; (b) absorption spectrum of GNS (i); (c) absorption spectrum of GNS agglomerated using HCl (ii) and NaOH (iii); (d) absorption spectrum of GNS agglomerated using KCl (iv), NaCl (v) and MgSO₄ (vi).

3.3 Materials & Methods

Imidacloprid (as Pestanal[®]), tetrachloroauric(III) acid (HAuCl₄), and trisodium citrate were purchased from Sigma Aldrich (Darmstadt, Germany). A stock solution of imidacloprid (10 mmol/L) in distilled water was prepared. Caustic soda, hydrochloric acid, sodium chloride, potassium chloride and magnesium sulfate were purchased from Roth (Karlsruhe, Germany) and prepared as 2 mol/L solutions.

Gold nanospheres (GNS) were prepared following a previously reported method.^{27–29} The original method by Turkevich and Frens using citrate reduction of HAuCl₄ was modified as follows. Under nitrogen atmosphere, 1.25 mL of HAuCl₄ (10 mmol/L) were added to 50 mL of deionized water and stirred at 500 rpm. The solution was heated to 80 °C. A solution of 1% trisodium citrate (450 mL) was added until the color changed from yellow to red. The solution was kept at 80 °C for another 5 minutes. The nanoparticle suspension was allowed to cool down to ambient temperature while being stirred. The nanoparticles were characterized by recording absorption spectra in a 10 mm quartz glass suprasil cuvette (Hellma, Muellheim, Germany) using a UV-1601PC (Shimadzu, Kyoto, Japan). The spectra were recorded from 190 nm to 800 nm with a resolution of 1 nm. Transmission electron micrographs were recorded using a H-7100FA (Hitachi, Tokyo, Japan) with 100 kV on carbon lacey copper grid. The software IC Measure, version 2.0.0.161 (The Imaging Source Europe, Bremen, Germany) was used to determine the size of the nanoparticles.

The Raman and SERS spectra in solution and on solid substrates with immobilized GNS were carried out using an ID mini Raman 2.0 hand-held spectrometer (Ocean Optics, Dunedin, FL, USA). A spectral range was recorded from 400 cm⁻¹ to 2300 cm⁻¹ with a resolution of

12 - 14 cm^{-1} , an excitation laser wavelength of 785 nm and a power of 100 mW. Thirty-two spectra were accumulated and averaged. Smoothing was applied using a Savitzky-Golay filter over 11 Points and a polynome of grade 3. Raster-Orbital-Scanning was chosen where acquisitions averaged ten individual spots on a square of 8 mm^2 .

For recording Raman and SERS spectra in solutions, samples were transferred into 2 mL vials (Glass Vials, Hannover, MD, USA). Subsequently, 1 mL of GNS suspension, corresponding to about 5×10^{11} particles, 0.5 mL deionized water, and 100 μL imidacloprid solution were added into the vial. For investigation of the agglomeration procedure, 2 mol/L solutions of caustic soda, hydrochloric acid, sodium chloride, potassium chloride and magnesium sulfate in deionized water were used as agglomeration agents. To ensure uniform agglomeration, samples were taken 1 minute prior to the measurement. To record SERS spectra on immobilized nanoparticles, two preparation routes were used for the substrates:

a. For preparing filter paper substrates, standard laboratory filter paper (Schleicher & Schuell, Dassel, Germany) was used. A 20 mL syringe was filled with GNS suspension. The flow rate was adjusted to 10 mL/min. A suction filter G4 connected to a water pump jet was placed under the syringe. Filter paper (1 cm^2) was placed on the suction filter and the GNS suspension was passed through the filter paper. A total of 100 mL GNS suspension was allowed to pass through the filter paper. The filter paper was then washed with 250 mL deionized water to remove residues of trisodium citrate. Eventually, the substrate was dried at room temperature and stored in the dark.

b. For preparing polylactic acid (PLA) substrates, a nonwoven PLA textile was gratefully received from the Deutsche Textilforschungszentrum Nord-West e.V. (Krefeld, Germany). Two layers of the textile were pressed together using a hydraulic press for 10 minutes at ten tons per square centimeter. A 1 cm^2 piece of double-layer PLA was placed on a glass slide and 15 mL of GNS suspension, 100 times concentrated, pipetted on the textile, which was then dried at room temperature and stored in the dark.

After preparing the GNS substrates, a spectrum was recorded as a background spectrum. For SERS investigation, 15 μL of the imidacloprid stock solution were pipetted onto the substrate. The spectrum was recorded after the substrate was allowed to dry at room temperature. For this purpose, the Raman instrument was equipped with a point-and-shoot adapter (Ocean Optics, Dunedin, FL, USA) that allowed to position the substrate at the correct distance to the spectrometer.

Spectral acquisition and baseline correction were performed using the software Peak Version 1.3.54 (Snowy Range Instruments, Laramie, WY, USA). All resulting data were processed using Matlab R2019b, Update 3 (MathWorks, Natick, MA, USA). Imidacloprid structure was optimized with Gaussian 16 software package using density with functional theory PW6B95D3 and basis set cc-pVTZ.³⁰⁻³² No imaginary frequencies during frequency calculation were obtained. Hence, the imidacloprid geometry represents a stable structure of a minimum on potential energy surface.

3.4 Results & Discussion

The size and shape of nanoparticles in a representative example of a nanoparticle preparation can be recognized in the TEM images shown in Figure 3.1(a). On analyzing the image, the nanoparticles amounted to 35 to 40 nm in diameter as would be expected for an absorption maximum around 530 nm.²⁷⁻²⁹ As expected, the nanoparticle suspension displayed an absorption band with a maximum at 530 nm, cf. Figure 3.1(b), typical for the plasmon band of isolated GNS. For successful SERS experiments, plasmon band and excitation wavelength of the laser should coincide or at least be as close as possible. This plasmon band tuning can be achieved by modification of the shape or by agglomeration of the nanospheres.³³ In this study, nanoparticles were agglomerated yielding in a shift towards the plasmon band close to 785 nm. Systematic variation of salts and pH was used to induce agglomeration, leading to the desired bathochromic effect. Increasing particle size causes a decrease in excitation energy of the plasmon and a corresponding red shift. Agglomeration may also transform the spherical to cylindrical particles. This transformation was observed as indicated by a second absorption band at higher wavelengths, cf. Figure 3.1(c,d). These findings agreed well with the observations by Xie et al. and Bell et al..^{34,35} Agglomeration in a basic milieu caused the occurrence of an absorption band at 700 nm, while acidic pH led to a band at 790 nm. Sodium chloride induced agglomeration resulted in a plasmon absorption at 683 nm, whereas magnesium sulfate produced an absorption at 722 nm and potassium chloride one at 762 nm, the latter extending over a range of 20 to 30 nm, cf. Figure 3.1. In all cases, plasmon bands were obtained in sufficient proximity to the laser wavelength to observe SERS spectra. When aspherical particles were formed, the second, redshifted plasmon band was observed. The presence of aspherical particles was reported to foster the formation of hot spots.³⁶ While an electromagnetic field of a certain strength prevails between two nanoparticles, a significantly stronger field occurs in hot spots, which leads to larger SERS amplification.

The chemical structure of imidacloprid and its 3D representation are shown in Figure 3.2. The scaffold comprises three main components; a chloropyridine ring attached to an imidazole ring via an alkyl bridge and a nitro group connected by a guanidine-like moiety to the imidazole ring. No Raman spectrum of imidacloprid in aqueous solution was observed with reasonable signal-to-noise-ratio. From the stock solution, no Raman spectrum at all was obtained due to the concentration of 0.025 mmol/L. For reference purposes during this study, the Raman spectrum of solid imidacloprid shown in Figure 3.3 was used. The assignment of the major Raman bands is given in the spectra in Figure 3.3 (a). The wavenumbers and assigned vibrations were compared with those computed by Moreira et al., who applied density-functional theory for the spectral interpretation.³⁷

In the regions between 400 and 600 cm^{-1} and between 1800 cm^{-1} and 2200 cm^{-1} no peaks were detected. Therefore, the spectral ranges below 600 and above 1800 cm^{-1} were omitted in the presented spectra. The vibrations were assigned to the three major structural features: chloro-pyridine, imidazole, and nitro group. The peak at 755 cm^{-1} originated from a C-C-C puckering of the ring of the chloropyridine moiety. The band at 770 cm^{-1} was related to an

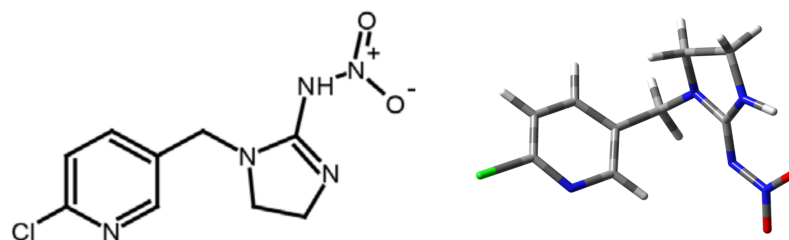


Figure 3.2 – Chemical structure (left) and computationally optimized 3D structure of imidacloprid (right).

asymmetrical nitro group stretching vibration. A C–C–C in plane bending of the pyridine structure gave rise to a signal at 818 cm^{-1} . The imidazoline ring moiety showed vibrational bands at 886 cm^{-1} (C–C–N bending), 960 cm^{-1} (symmetric stretching), 998 cm^{-1} (symmetric stretching), 1053 cm^{-1} (asymmetric stretching). A C–C–C breathing of the pyridine moiety was observed at 1104 cm^{-1} . The imidazoline ring stretching was found at 1141 cm^{-1} . The bands at 1279 cm^{-1} and 1371 cm^{-1} stemmed from a CH_2 methylene bending of the imidazole ring. The C–C stretching of pyridine was found at 1451 cm^{-1} . The imidazole ring displayed a second stretching vibration of the C–N–N moiety at 1481 cm^{-1} . The nitro guanidine part had a stretching vibration at 1580 cm^{-1} .

A solution of imidacloprid with a concentration of 25.5 ng/L in the presence of suspended GNS was investigated. The resulting spectrum was compared to the solid-state spectrum. Due to the SERS enhancement, a strong signal was observed, where imidacloprid in solution did not exhibit any signal. As demonstrated in Figure 3.3 (b), the bands appeared more enhanced at low wavenumbers than at high ones. The signals were most amplified in the range of $750\text{--}1250\text{ cm}^{-1}$. Above 1250 cm^{-1} , the low signal-to-noise ratio of the enhanced peaks did not allow assignment. This may be due to no or insufficient agglomeration, which prevents hot spots from being formed.

In particular, the vibrations of the pyridine moiety at lower wavenumbers were enhanced, among them the bands at 831 cm^{-1} , 998 cm^{-1} , 1110 cm^{-1} . These are related to the pyridine ring and the imidazol moiety. The nitrogen atoms in both parts could establish weak attractive interactions with the GNS, which causes a decrease in distance between the nanoparticle and the molecule.

The spectrum of imidacloprid in the presence of GNS after agglomeration by hydrochloric acid addition, cf. Figure 3.3 c), contained more intense and distinguishable signals for the same amount of imidacloprid than the one recorded in the presence of GNS. It is also remarkable that the bands at higher wavenumbers were evenly amplified. The bands also appeared more resolved, see e.g. the signals at 755 , 1054 , and 1371 cm^{-1} . This observation might be traced back to the arrangement of imidacloprid on the nanoparticle. As a result of sufficient destabilization of the citrate layer during hydrochloric acid treatment and agglomeration, imidacloprid molecules may experience more space at the nanoparticle surface and re-orient to a preferred arrangement.³⁸ Since the sample solution was enriched with chloride ions during acid addition, a chloride ion effect may additionally influence the SERS activity of the nanoparticles in a positive way. Li et al. observed a change of charge

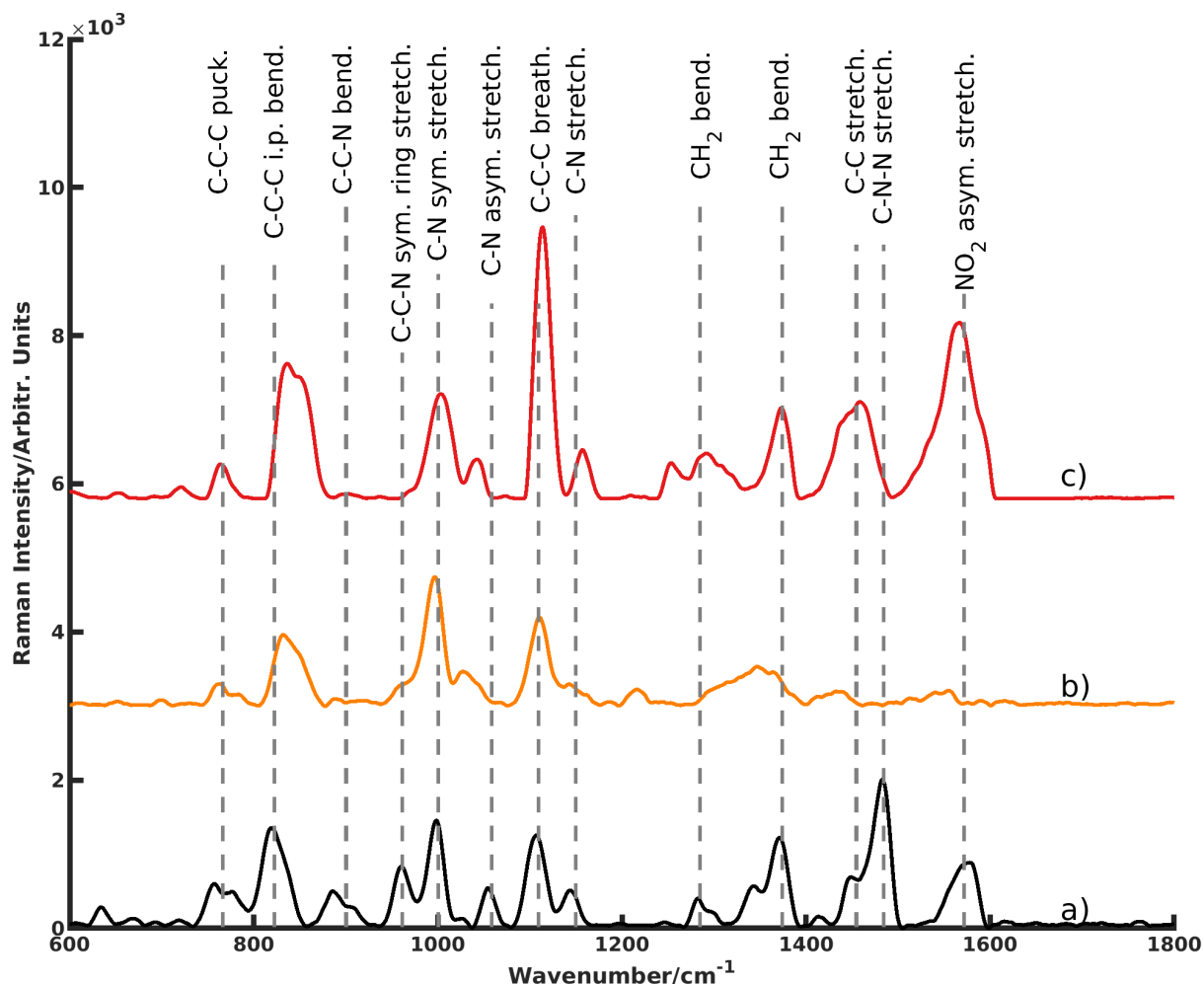


Figure 3.3 – (a) Raman spectrum of imidacloprid as a solid; (b) SERS spectra of imidacloprid in the presence of GNS, and (c) in the presence of GNS agglomerated by HCl. Vibrations were assigned based on the Raman spectrum. Vibrations are abbreviated: i.p.: in-plane; sym: symmetrical; asym: asymmetrical; puck: puckering; bend: bending; stretch: stretching; breath: breathing.

happening on the surface of the nanoparticles.³⁹ The decrease in charge caused an increase of the field emanating from the plasmon and led to a corresponding signal enhancement. This change of charge resulted in an agglomeration of the nanoparticles leading to a signal enhancement. Furthermore, the bands at 755 and 1054 cm^{-1} were shifted as compared to the solid-state spectrum. The signal at 755 cm^{-1} moved to 764 cm^{-1} and that at 1054 cm^{-1} to 1041 cm^{-1} . Frequency or wavenumber shifts result from CM, while the EM effect might still produce the more significant signal enhancement.

The agglomeration of GNS induced by salt addition led to similar spectra as before, cf. Figure 3.4. From inspection of the spectra in Figure 3.3, the following bands were interpreted as having experienced wavenumber shifts: 764, 837, 1116, 1430, and 1550 cm^{-1} . In contrast, the band at 955 cm^{-1} remained unshifted, which indicates amplification from the EM effect. The signal at 1374 cm^{-1} was shifted to 1340 cm^{-1} , see Figure 3.3 (c). From comparison with the vibrational frequencies, it may be assumed that imidacloprid molecules formed charge-transfer (CT) complexes with the GNS. The CT led to an alteration of the charge distribution within imidacloprid, thus changing the vibrational modes and polarizability. The

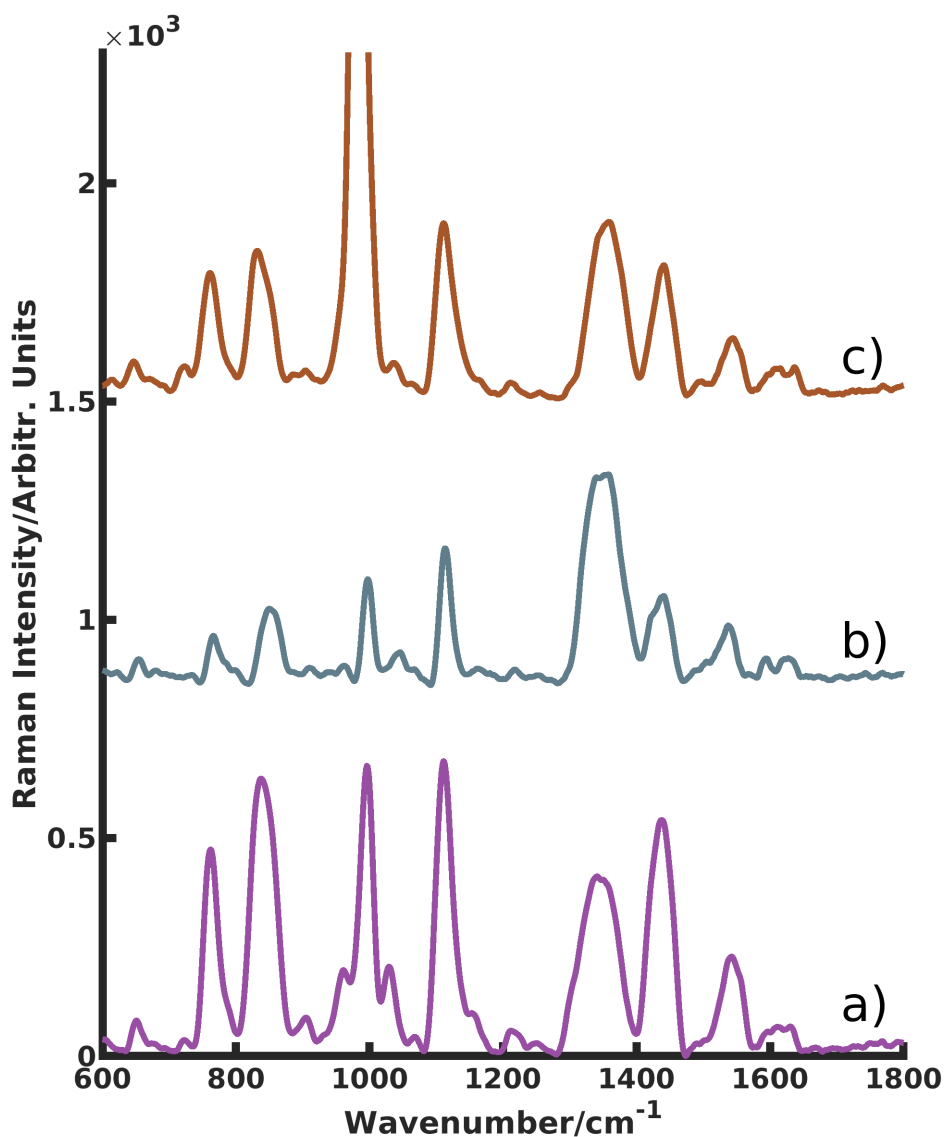


Figure 3.4 – SERS spectra of imidacloprid in solution in the presence of GNS agglomerated by (a) NaCl; (b) KCl; and (c) MgSO_4 . The strongest signal in (c) is cut off as it stems from sulfate.

CT complex between molecule and nanoparticle might be considered as a new entity yielding new Raman bands, which may or may not be – in parts – similar to those of the unbound molecule. This effect renders analytical identification of compounds through SERS difficult. Inspection of signal enhancements and shifts, cf. Figure 3.3, suggested that imidacloprid molecules bind – or are at least in close proximity – to the gold surface through the nitro group and the pyridine moiety. Coordinative binding and charge transfer to the gold surface lead to changes in the polarizability, and hence to spectral changes. Surface selection rules also apply, which enhance or cancel signals. Hence, interpretation of the spectral changes requires further thorough analysis. The most obvious enhancing effects were observed at 1580 and 1104 cm^{-1} , which were attributed to nitro and pyridine vibrations, whereas bands at 1279 and 1481 cm^{-1} belonging to imidazole vibrations were much less enhanced.

As to the solution spectra, different forms of agglomeration induced by various salts and acids also led to different SERS spectra. The signals enhanced by GNS agglomerated by sodium chloride and potassium chloride looked very similar. In the case of magnesium sulfate an additional peak due to the sulfate was observed at 955 cm^{-1} . The sizes of the nanoparticle clusters were observed to influence the intensities of all bands. Nanoparticle agglomeration induced by magnesium sulfate, cf. Figure 3.4 (c), led to the band at 955 cm^{-1} which was a superposition of the symmetric C–N stretching vibration and the vibration of the sulfate ion. Hydrochloric acid as agglomeration agent induced the strongest signal amplification. This observation may be explained in terms of ionic strength and the chloride ion effect. An analogous effect was described for sulfate.⁴⁰ Dowgiallo and Guenther reported on the solution SERS spectra of numerous compounds in the presence of GNS agglomerated by hydrochloric acid.⁴¹ For imidacloprid, bands at 837 and 955 cm^{-1} were observed. The wave numbers differed slightly from those observed in this study. This could be due to different spectral resolutions and laser powers, which were 3.5 times higher in the previous study.

Imidacloprid SERS spectra recorded on substrates made of GNS on textile fiber or filter paper support were again different from solution SERS spectra, cf. Figure 3.5. Firstly, the spectrum on PLA fabric displayed higher intensity obviously caused by stronger enhancement. This may be induced by the chemical structure of PLA, which exercises a hydrophobic effect due to the methyl groups. The hydrophobic surface led to a concentrated spot of the applied nanoparticle droplet that did not extend during drying. On filter paper as substrate, a significantly larger amount of nanoparticle suspension was required to achieve the same concentration of nanoparticles in one spot, since filter paper is hydrophilic and leads to a rapid horizontal and vertical expansion of the droplet. Since the coffee ring effect is active for both PLA and filter paper support, still a large part of the nanoparticles was transported away from the center of the spot.⁴² Vibrations of imidacloprid on the two substrates were amplified in different ways. It could not be clearly determined how the imidacloprid molecule might be arranged on or between the nanoparticles on the substrates. All bands were enhanced by the EM effect and shifted differently by the CM effect. Largely different SERS spectra have been reported previously for imidacloprid under different conditions.^{21,41,43,44} These differences can be traced back to the nanoparticles made of different noble metals, such as silver and gold. A second cause stems from the shape of the nanoparticles, e.g. spheres or rods. A third reason originates from different substrates. While the bands at 870 , 1026 , 1126 , 1295 , and 1450 cm^{-1} were also observed in the mere PLA spectrum, and hence originated from the substrate, filter paper as substrate did not give rise to background signals. Yet, background signals might be subtracted. Nonetheless, background correction was not carried out since the software of the handheld Raman spectrometer would not allow this operation during field use. The band at 1240 cm^{-1} in both spectra originated from citrate used during production to stabilize the nanoparticles in solution. During drying of substrate, citrate precipitated. Without background and citrate bands, the following signals stemmed

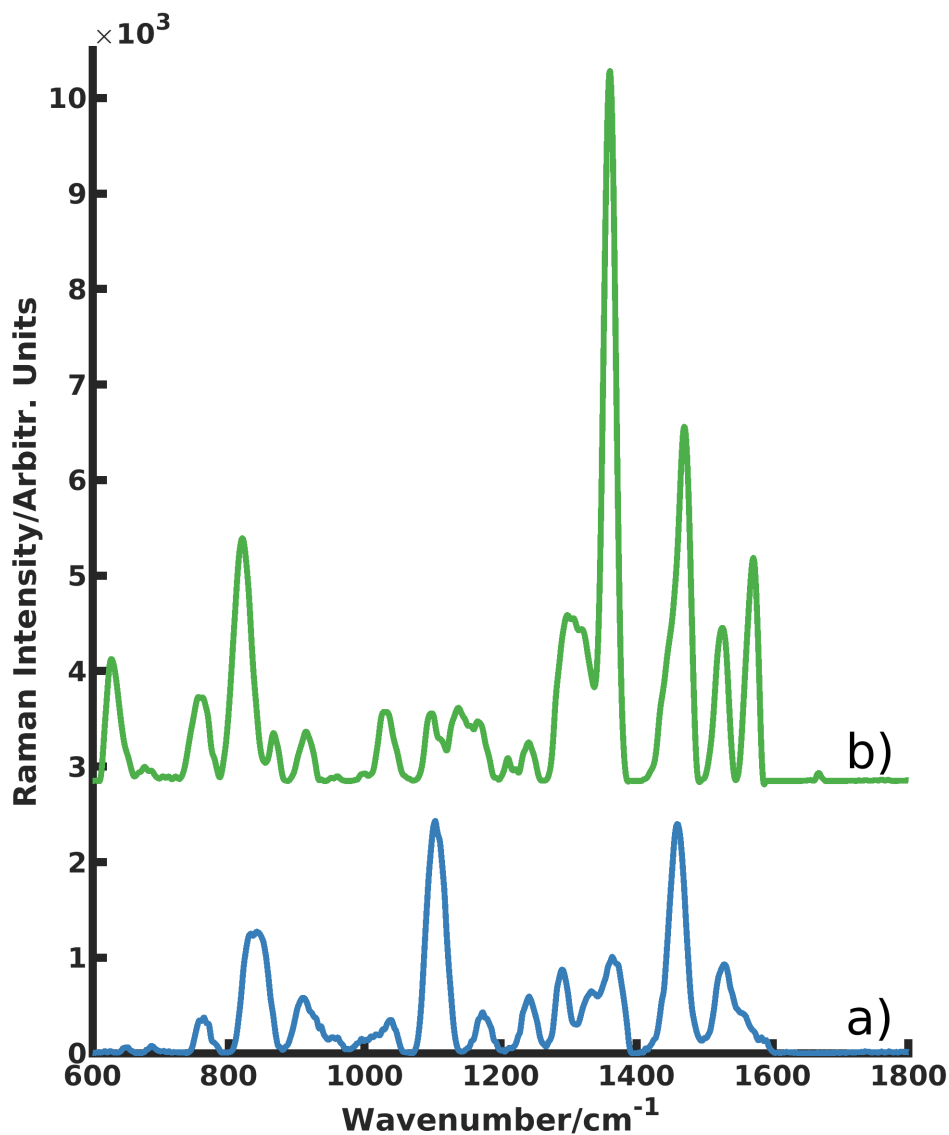


Figure 3.5 – SERS spectra of imidacloprid on (a) gold nanoparticle filter paper and (b) PLA substrate.

from imidacloprid, see Figure 3.5: 755, 818 cm⁻¹ shifted to 827, 998, 1053 cm⁻¹ shifted to 1034, 1104, 1279, 1450 cm⁻¹ shifted to 1461 and 1580 cm⁻¹ shifted to 1530 cm⁻¹. The band at 1450 cm⁻¹ also occurred in the PLA spectra, but background peaks were not shifted or amplified. Therefore, the shifted band at 1461 cm⁻¹ clearly originated from imidacloprid. In the spectrum of imidacloprid on PLA substrate, a peak at 1164 cm⁻¹ was observed, which can be related to the peak at 1141 cm⁻¹ in the solid-state spectrum.

Higher nanoparticle density accounted for more and stronger hot spots and hence signal enhancement, cf. spectral scale in Figure 3.5, which will significantly facilitate the analytical detection of imidacloprid. It is also possible to prepare the substrate using lower amounts of GNS suspension rendering the analyses less expensive. Both methods, cf. Figure 3.6, agglomerated GNS in solution and GNS immobilized on supports, allowed rapid and sensitive identification of imidacloprid. In addition, both would allow for on-site analysis, as the SERS matrix can be prepared in the laboratory beforehand.

Table 3.1 – LOD for SERS methods of imidacloprid.

Analysis method	LOD
Solution	
GNS	70 $\mu\text{g/L}$
GNS + HCl	30 $\mu\text{g/L}$
GNS + NaCl	170 $\mu\text{g/L}$
GNS + KCl	240 $\mu\text{g/L}$
GNS + MgSO ₄	280 $\mu\text{g/L}$
Substrate	
GNS on filter paper	240 ng/L
GNS on PLA textile	280 ng/L

For analyses in solution, HCl proved to be the best agglomeration agent, as the highest signal enhancement was observed. In consequence, the lowest limit of detection (LOD), 30 mg/L for imidacloprid in solution was obtained, cf. Table 3.1. LODs were calculated as 3 times the signal-to-noise ratio, where the noise was sampled over a range of 200 cm^{-1} . The most intense band of imidacloprid in each spectrum was chosen as signal. Furthermore, the spectrum showed good resolution rendering the identification more reliable. For the GNS substrate, PLA was superior to filter paper. It showed a lower LOD, 3 ng, compared to filter paper substrates, 15 ng. It should be mentioned, that PLA is made of sustainable materials and less GNS suspension was needed for analysis. Using either method, several types of samples could be analyzed. Aqueous or samples dissolved in organic solvents could be screened using GNS dispersions, only the agglomeration agent would need to be added in the field. For solid samples or suspensions, nanoparticles on substrate could be used. Raman detection could enable fast on-site analysis with some medium throughput capabilities. Since the analysis is non-destructive, interesting samples could be stored and passed on to more thorough laboratory analysis. Significant shortening of total analysis time and reduction of sample numbers would result. Yet, a spectral database would have to be generated in order to identify the target species and to remove background signals of agglomeration agents and substrates. Since the spectrum itself depends on particle material, particle morphology, agglomeration agents and substrate, a database would also have to take these analytical or chemical parameters into account. Furthermore, substrates would need to be prepared in a highly reproducible manner in order to provide identical SERS spectra of an analyte. Promising studies using e.g. printing procedures have been reported.^{13,45} In a field study, samples should be investigated using both, solution and substrate methods.

An estimate of expected agricultural concentrations should yield a rough evaluation of the potential for field applications: around 95,000 grains of wheat per hectare are commonly distributed during sowing. This corresponds to an average of 95 g per hectare of a systemically applied pesticide, such as imidacloprid.⁴⁶ Assuming a penetration depth of 0.02 m for the pesticide after aqueous removal from grains by rain, a concentration of 0.475 g/m^3 would be accumulated. With the average density of soil being 1.4 g/cm^3 , a mass concentration of 0.34 mg of imidacloprid per gram of soil result.⁴⁷ In terms of analytical sampling, i.e. about

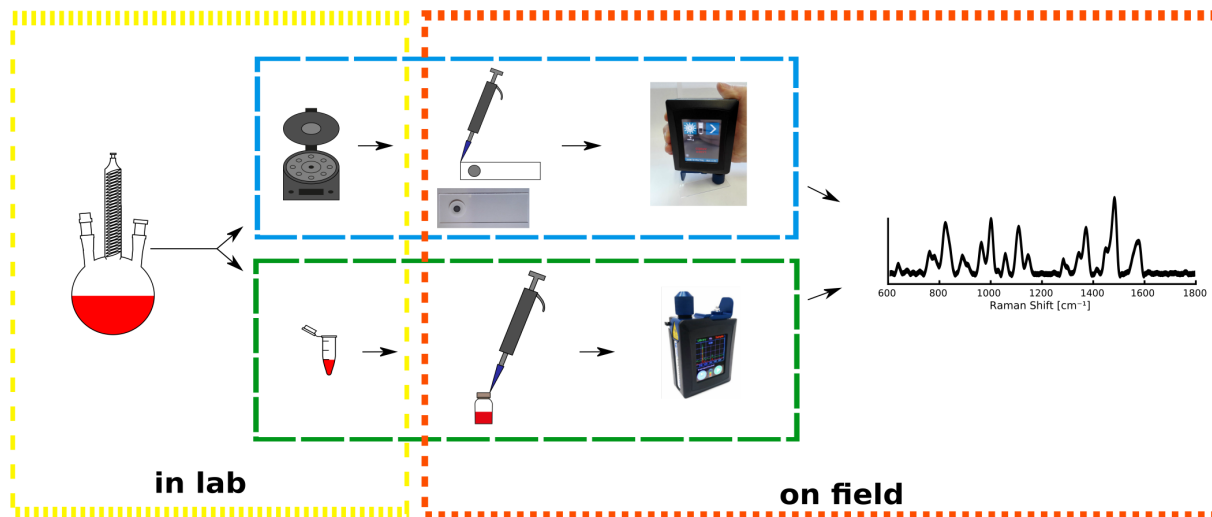


Figure 3.6 – Schematic depiction of analysis routes for measuring on solid nanoparticle substrate (blue, upper route) and in solution (green, lower route).

500 g of soil per sample, a total of approximately 170 mg of imidacloprid should be expected. Since a wheat grain generally absorbs less than 10 % of the applied stain, 306 mg/kg imidacloprid remain in the soil.⁴⁸ Hence, a lower microgram range up to a few hundreds of micrograms will be the analytical working range. In this study, approximately 300 mg/L were detected with good signal-to-noise ratio. With the LOD of 30 mg/L for the method with HCl, just 1/10 of a typical soil sample would be needed. For the method with PLA substrate and a sample volume of 15 mL, a detection of imidacloprid was achieved with a LOD of 3 ng. These LODs should be sufficient to allow for on-site extraction of imidacloprid from a 50 to 100 g soil sample. In conclusion, using SERS and pre-prepared GNS, either agglomerated in solution or on a PLA substrate, together with a handheld Raman spectrometer proved a promising tool for in-field pesticide analysis.

3.5 Conclusion

The described SERS method was successfully applied to identify imidacloprid. Analysis of the Raman and SERS spectra yielded a structure proposal for the molecular arrangement of imidacloprid on the GNS surface. Since the method is based on pre-prepared acid agglomerated GNS solutions or GNS PLA substrates and a handheld Raman spectrometer, the assay should be suitable for fast and easy field measurements. The estimated limit of detection reached the expected pesticide content of $\sim 300 \mu\text{g}/\text{kg}$ in agricultural soils. Such testing would allow to precede more in-depth analyses, as only positive on-site test results would need to proceed to laboratory examinations. The method will be extended to other pesticides. For identification, a spectral library needs to be built, since SERS spectra are prone to change depending on the enhancing agent. For quantitation, calibration series need to be recorded and validated.

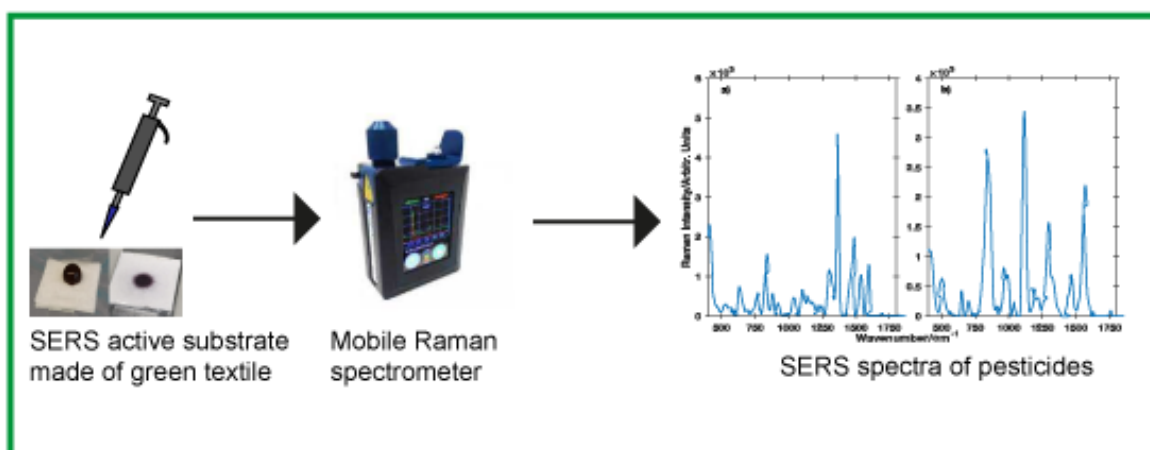
References

1. Tsagkaris, A. S., Uttl, L., Pulkrabova, J. & Hajslova, J. Screening of Carbamate and Organophosphate Pesticides in Food Matrices Using an Affordable and Simple Spectrophotometric Acetylcholinesterase Assay. *Applied Sciences* **10**, 22–36 (2020).
2. Mitchell, E. A. D., Mulhauser, B., Mulet, M., *et al.* A worldwide survey of neonicotinoids in honey. *Science* **358**, 109–111 (2017).
3. Lopez-Osorio, F. & Wurm, Y. Healthy Pollinators: Evaluating Pesticides with Molecular Medicine Approaches. *Trends in Ecology & Evolution* **35**, 380–383 (2020).
4. Sgolastra, F., Medrzycki, P., Bortolotti, L., *et al.* Bees and pesticide regulation: Lessons from the neonicotinoid experience. *Biological Conservation* **241**, 108356 (2020).
5. Woodcock, B. A., Bullock, J. M., Shore, R. F., *et al.* Country-specific effects of neonicotinoid pesticides on honey bees and wild bees. *Science* **356**, 1393–1395 (2017).
6. Kessler, S. C., Tiedeken, E. J., Simcock, K. L., *et al.* Bees prefer foods containing neonicotinoid pesticides. *Nature* **521**, 74–76 (2015).
7. Henry, M., Beguin, M., Requier, F., *et al.* A Common Pesticide Decreases Foraging Success and Survival in Honey Bees. *Science* **336**, 348–350 (2012).
8. Pilling, E., Campbell, P., Coulson, M., Ruddle, N. & Tornier, I. A Four-Year Field Program Investigating Long-Term Effects of Repeated Exposure of Honey Bee Colonies to Flowering Crops Treated with Thiamethoxam. *PLOS ONE* **8**, e77193 (2013).
9. Agency, U. E. P. Guidance for Assessing Pesticide Risks to Bees. *Health Canada Pest Management Regulatory Agency (PMRA), and California Department of Pesticide Regulation* (2014).
10. Tsvetkov, N., Samson-Robert, O., Sood, K., *et al.* Chronic exposure to neonicotinoids reduces honey bee health near corn crops. *Science* **356**, 1395–1397 (2017).
11. Babazadeh, S., Moghaddam, P. A., Keshipour, S. & Mollazade, K. Analysis of imidacloprid and penconazole residues during their pre-harvest intervals in the greenhouse cucumbers by HPLC–DAD. *Journal of the Iranian Chemical Society* **17**, 1439–1446 (2020).
12. Anastassiades, M., Lehotay, S. J., Stajnbaher, D. & Schenck, F. J. Fast and Easy Multiresidue Method Employing Acetonitrile Extraction/Partitioning and “Dispersive Solid-Phase Extraction” for the Determination of Pesticide Residues in Produce. *Journal of AOAC International* **86**, 412–431 (2019).
13. Hoppmann, E. P., Yu, W. W. & White, I. M. Highly sensitive and flexible inkjet printed SERS sensors on paper. *Methods* **63**, 219–224 (2013).
14. Zhao, J., Long, L., Weng, G., *et al.* Multi-branch Au/Ag bimetallic core–shell–satellite nanoparticles as a versatile SERS substrate: the effect of Au branches in a mesoporous silica interlayer. *J. Mater. Chem. C* **5**, 12678–12687 (2017).
15. Zhong, L.-B., Liu, Q., Wu, P., *et al.* Facile On-Site Aqueous Pollutant Monitoring Using a Flexible, Ultralight, and Robust Surface-Enhanced Raman Spectroscopy Substrate: Interface Self-Assembly of Au@Ag Nanocubes on a Polyvinyl Chloride Template. *Environmental Science & Technology* **52**, 5812–5820 (2018).

16. Halvorson, R. A. & Vikesland, P. J. Surface-Enhanced Raman Spectroscopy (SERS) for Environmental Analyses. *Environmental Science & Technology* **44**, 7749–7755 (2010).
17. Yao, J., Quan, Y., Gao, M., *et al.* AgNPs decorated Mg-doped ZnO heterostructure with dramatic SERS activity for trace detection of food contaminants. *Journal of Materials Chemistry C* **7**, 8199–8208 (2019).
18. Pang, S., Yang, T. & He, L. Review of surface enhanced Raman spectroscopic (SERS) detection of synthetic chemical pesticides. *Trends in Analytical Chemistry* **85**, 73–82 (2016).
19. Legner, R., Wirtz, A. & Jaeger, M. Using Compact ¹H NMR, NIR, and Raman Spectroscopy Combined with Multivariate Data Analysis to Monitor a Biocatalyzed Reaction in a Microreaction System. *Journal of Spectroscopy* **2018**, 5120789 (2018).
20. Legner, R., Voigt, M., Servatius, C., *et al.* A Four-Level Maturity Index for Hot Peppers (*Capicum annum*) Using Non-Invasive Automated Mobile Raman Spectroscopy for On-Site Testing. *Applied Sciences* **11** (2021).
21. Gong, X., Tang, M., Gong, Z., *et al.* Screening pesticide residues on fruit peels using portable Raman spectrometer combined with adhesive tape sampling. *Food Chemistry* **295**, 254–258 (2019).
22. Kwon, G., Kim, J., Kim, D., *et al.* Nanoporous cellulose paper-based SERS platform for multiplex detection of hazardous pesticides. *Cellulose* **26**, 4935–4944 (2019).
23. Nie, S. & Emory, S. R. Probing Single Molecules and Single Nanoparticles by Surface-Enhanced Raman Scattering. *Science* **275**, 1102–1106 (1997).
24. Chen, T., Wang, H., Chen, G., *et al.* Hotspot-Induced Transformation of Surface-Enhanced Raman Scattering Fingerprints. *ACS Nano* **4**, 3087–3094 (2010).
25. Pilot, R., Signorini, R., Durante, C., *et al.* A Review on Surface-Enhanced Raman Scattering. *Biosensors* **9** (2019).
26. Moskovits, M. Surface-enhanced spectroscopy. *Rev. Mod. Phys.* **57**, 783–826 (1985).
27. Frens, G. Controlled Nucleation for the Regulation of the Particle Size in Monodisperse Gold Suspensions. *Nature Physical Science* **241**, 20–22 (1973).
28. Kimling, J., Maier, M., Okenve, B., *et al.* Turkevich Method for Gold Nanoparticle Synthesis Revisited. *The Journal of Physical Chemistry B* **110**, 15700–15707 (2006).
29. Turkevich, J., Stevenson, P. C. & Hillier, J. A study of the nucleation and growth processes in the synthesis of colloidal gold. *Discussions of the Faraday Society* **11**, 55–75 (1951).
30. Frisch, M. J., Trucks, G. W., Schlegel, H. B., *et al.* *Gaussian 16 Revision C.01* Gaussian Inc. Wallingford CT. 2016.
31. Kendall, R. A., Dunning Thom H., J. & Harrison, R. J. Electron affinities of the first-row atoms revisited. Systematic basis sets and wave functions. *The Journal of Chemical Physics* **96**, 6796–6806 (1992).
32. Woon, D. E. & Dunning Thom H., J. Calculation of the electron affinities of the second row atoms: Al–Cl. *The Journal of Chemical Physics* **99**, 3730–3737 (1993).

33. Tian, F., Bonnier, F., Casey, A., Shanahan, A. E. & Byrne, H. J. Surface enhanced Raman scattering with gold nanoparticles: effect of particle shape. *Analytical Methods* **6**, 9116–9123 (22 2014).
34. Xie, J., Zhang, Q., Lee, J. Y. & C., D. I. The Synthesis of SERS-Active Gold Nanoflower Tags for In Vivo Applications. *ACS Nano* **2**, 2473–2480 (2008).
35. Bell, S. E. J. & McCourt, M. R. SERS enhancement by aggregated Au colloids: effect of particle size. *Physical Chemistry Chemical Physics* **11**, 7455–7462 (2009).
36. Ding, S.-Y., Yi, J., Li, J.-F., *et al.* Nanostructure-based plasmon-enhanced Raman spectroscopy for surface analysis of materials. *Nature Reviews Materials* **1**, 16021 (2016).
37. Moreira, A. A., De Lima-Neto, P., Caetano, E. W., Barroso-Neto, I. L. & Freire, V. N. The vibrational properties of the bee-killer imidacloprid insecticide: A molecular description. *Spectrochimica Acta Part A: Molecular and Biomolecular Spectroscopy* **185**, 245–255 (2017).
38. Park, J.-W. & Shumaker-Parry, J. S. Structural Study of Citrate Layers on Gold Nanoparticles: Role of Intermolecular Interactions in Stabilizing Nanoparticles. *Journal of the American Chemical Society* **136**, 1907–1921 (2014).
39. Li, Y.-S., Cheng, J. & Wang, Y. Surface-enhanced Raman spectra of dyes and organic acids in silver solutions: chloride ion effect. *Spectrochimica Acta Part A: Molecular and Biomolecular Spectroscopy* **56**, 2067–2072 (2000).
40. Zhang, Y., Sun, S., Zhang, X., *et al.* Sulfate-ion-assisted galvanic replacement tuning of silver dendrites to highly branched chains for effective SERS. *Physical Chemistry Chemical Physics* **16**, 18918–18925 (2014).
41. Dowgiallo, A. M. & Guenther, D. A. Determination of the Limit of Detection of Multiple Pesticides Utilizing Gold Nanoparticles and Surface-Enhanced Raman Spectroscopy. *Journal of Agricultural and Food Chemistry* **67**, 12642–12651 (2019).
42. Yunker, P. J., Durian, D. J. & Yodh, A. G. Coffee rings and coffee disks: Physics on the edge. *Physics Today* **66**, 60–61 (2013).
43. Chen, Q., Hassan, M. M., Xu, J., *et al.* Fast sensing of imidacloprid residue in tea using surface-enhanced Raman scattering by comparative multivariate calibration. *Spectrochimica Acta Part A: Molecular and Biomolecular Spectroscopy* **211**, 86–93 (2019).
44. Hou, R., Pang, S. & He, L. In situ SERS detection of multi-class insecticides on plant surfaces. *Analytical Methods* **7**, 6325–6330 (2015).
45. Yu, W. W. & White, I. M. Inkjet Printed Surface Enhanced Raman Spectroscopy Array on Cellulose Paper. *Analytical Chemistry* **82**, 9626–9630 (2010).
46. Schnier, H. F., Wenig, G., Laubert, F., Simon, V. & Schmuck, R. Honey Bee Safety of Imidacloprid Corn Seed Treatment. *Bulletin of Insectology* **56**, 73–75 (2003).
47. Suuster, E., Ritz, C., Roostalu, H., *et al.* Soil bulk density pedotransfer functions of the humus horizon in arable soils. *Geoderma* **163**, 74–82 (2011).
48. Laurent, F. M. & Rathahao, E. Distribution of [¹⁴C]Imidacloprid in Sunflowers (*Helianthus annuus* L.) following Seed Treatment. *Journal of Agricultural and Food Chemistry* **51**, 8005–8010 (2003).

4 Green Textile Materials for Surface-Enhanced Raman Spectroscopy Identification of Pesticides Using a Raman Handheld Spectrometer for In-Field Detection



Chapter 4 is reproduced from *Andrea Hermsen, Justus Schoettl, Florian Hertel, Matthias Cerullo, Adrian Schlueter, Christian Lehmann, Christian Mayer & Martin Jaeger (2022) Green Textile Materials for Surface Enhanced Raman Spectroscopy Identification of Pesticides Using a Raman Handheld Spectrometer for In-Field Detection, Applied Spectroscopy, DOI: 10.1177/00037028221097130* with permission from Sage.

4.1 Abstract

Surface enhanced Raman spectroscopy (SERS) has evolved into a powerful analytical method in food and environmental analytical sciences due to its high sensitivity. Pesticide analysis is a major discipline therein. Using sustainable materials has become increasingly important to adhere to Green Chemistry principles. Hence, the green textiles poly-(L-lactic acid) (PLA) and the mixed fabric polyethylene terephthalate polyamide (PET/PA) were investigated for their applicability as solid supports for gold nanoparticles to yield SERS substrates. Gold nanoparticle solutions and green textile supports were prepared after preparation optimization. Particle size, dispersity, and particle distribution over the textiles were characterized by absorption spectroscopy and transmission electron imaging. The performance of the SERS substrates was tested using the three pesticides imidacloprid, paraquat, and thiram and a handheld Raman spectrometer with a laser wavelength of 785 nm. The resulting SERS spectra possessed an intra-substrate variation of 7 – 8% in terms of the residual standard deviation. The inter-substrate variations amounted to 15% for PET/PA and to 27% for PLA. Substrate background signals were smaller with PLA but more enhanced through PET/PA. The pesticides could be detected at 1 pg on PET/PA and at 3 ng on PLA. Hence, PET/PA woven textile soaked with gold nanoparticle solution provides green SERS substrates and might prove, in combination with fieldable Raman spectrometers, suitable for in-field analytics for pesticide identification.

4.2 Introduction

The introduction of surface enhanced Raman spectroscopy (SERS) has amended the sensitivity of Raman spectroscopy and thus opened up a much broader range of applications. Surface enhancement amplifies signals up to 8 to 14 orders of magnitude.¹ Different kinds of nanoparticles were used for SERS, mostly gold, silver or copper nanoparticles as their surface plasmon resonances fall into the range of common Raman laser wavelengths.² The SERS mechanism is based on the electromagnetic and the chemical effect.³ SERS spectra can be obtained in solution or on solid supports. Such substrates are produced from laser ablation techniques, chemical synthesis, such as Ferrero[®]-chocolate-like Cu₂₀@Ag substrates or Eggshell membranes.⁴⁻⁶ Special-shaped nanoparticles may serve as SERS active substrates such as snowflake-shaped gold nanoparticles are used for the detection of organophosphates, or micro-bowl structured silver nanoparticles.^{7,8} Nanoparticles with a hybrid system in 3D Au@Ag nanocubes as mono films were used to detect chrysoidine.⁹ To avoid a complex process for substrate production requiring environmentally hazardous chemicals or high energy consumption, green textiles shall be investigated for their suitability. Poly(L-lactic acid) (PLA) textiles and textiles made of polyethylene terephthalate and polyamide (PET/PA) are considered green textiles. PLA is currently one of the most studied biorenewables as it is biodegradable and has little greenhouse gas emission. Microfilamentous PET/PA fibers are produced by water jet treatment yielding little waste. Water consumption is four hun-

dred times lower than in cotton production, is recycled and returned to the production process.¹⁰ Technological advances have paved the way for SERS into environmental and food analysis.¹¹⁻¹⁵ Important progress has been demonstrated in forensic science.¹⁶ The methodology is also increasingly investigated for applications to detect pesticides.¹⁷⁻¹⁹ The fast and easy in-field identification of pesticides becomes more and more important as bans on pesticides, such as imidacloprid, thiamethoxam, or clothianidin grow.^{20,21} Potential hazards for the terrestrial and aquatic environment rely on the detection of the pesticides.^{22,23} Most commonly, their routine trace analysis is accomplished through chromatography, such as high-performance liquid chromatography and gas chromatography, coupled to mass spectrometry due to their high specificity and sensitivity.²⁴ Yet, these instruments are not suitable for in-field analysis due to their size and weight. In addition, these chromatographic methods also require long and costly analysis times and can only be operated by trained operators.²⁵ However, using a Raman handheld spectrometer in combination with the SERS method makes in-field use possible at low cost and short analysis time.²⁶ In this study, a route to obtain sensitive and reproducible SERS spectra using solid support substrates and a handheld Raman spectrometer was developed for the pesticide imidacloprid as model compound. The prepared nanoparticles were characterized with respect to their size and size distribution. Results from imaging techniques were compared to those from absorption spectroscopy. The green textile materials PLA and PET/PA were investigated as solid supports of the gold nanoparticles for their applicability as SERS substrates. The results were analyzed with respect to enhancement, background signals, intra- and inter-substrate reproducibility as prerequisites for analytical utilization. Finally, the method was extended to thiram and paraquat to evaluate its potential towards a general fast, easy, and sensitive method for pesticide characterization.

4.3 Materials & Methods

Gold nanospheres were prepared according to the following route based on previously described protocols.²⁷⁻²⁹ Thus, 1.25 mL of hydrogen tetrachloroaurate solution (HAuCl_4 , 10 mmol/L) and 450 μL of 1% trisodium citrate solution were successively added to 50 mL of deionized water at 80 °C and stirred at 500 rpm. After color change from yellow to red, the solution was kept at 80 °C for another 5 min and then cooled down to ambient temperature while stirred. The synthesis was carried out under a nitrogen atmosphere. To concentrate the gold nanospheres the suspension was centrifuged at 770 g for 15 min. The supernatant was removed, and the resulting pellet resuspended. The process was repeated twice to increase nanoparticle concentration. Absorption spectra and transmission electron micrographs were recorded to characterize the nanoparticles and their size distribution. For absorption experiments, the centrifuged and non-centrifuged nanoparticle suspensions were diluted 1:10. For reference purposes, a gold nanoparticle reference standard with nanoparticles of known diameter, that is, 40 nm (Sigma-Aldrich, Germany) was applied. The reference solution was diluted with deionized water such that contents of 20, 40, 60, 80, and 100% resulted.

The solutions were used for calibration experiments. Absorption spectra of the liquids were recorded in a 10 mm quartz glass Suprasil cuvette (Hellmann, Germany) using a UV5Nano (Mettler Toledo, USA) with a spectral range from 200 to 1100 nm and a resolution of 1 nm. In addition, absorption spectra of spherical gold nanoparticles with a diameter of 40 nm were simulated using the software MiePlot v.4.6.14 choosing water as the surrounding medium with the Segelstein parameter for refractive indices.³⁰ Scanning electron micrographs (SEM) were recorded using a Hitachi TM3030 with an acceleration voltage of 15 kV. Transmission electron microscopy (TEM) was performed using a Hitachi HF2000 transmission electron microscope. It is operated at 200 kV accelerating voltage and equipped with a cold field emission gun. The size distribution was determined by measuring and averaging over 100 nanoparticles using IC Measure, v.2.0.0.161 (The Imaging Source Europe, Bremen, Germany). The pesticides imidacloprid, thiram, and paraquat were acquired as Pestanal series from Sigma-Aldrich (Darmstadt, Germany). Stock solutions of the compounds were prepared such that final concentrations were 1 mM for imidacloprid, 0.125 mM for thiram and 0.1 mM for paraquat. For SERS experiments on solid support, pieces of textile with a size of 1 mm² were used as substrates. The textiles consisted of polylactid acid (PLA), a nonwoven textile (Deutsche Textilforschungszentrum Nord-West e.V., Germany), and polyethylene terephthalate and polyamide (PET/ PA, Freudenberg, Germany). For single-layer substrates, the textile samples were attached to a conventional microscope glass slide; for double-layer substrates, two stacked pieces of textile were fixed to the glass slide. For double-layer pressed substrates, two textile layers were forced together using a hydraulic press (Perkin Elmer, Germany) exercising a pressure of 10 tons per square centimeter for 10 min. Finally, 15 μ L of gold nanoparticle suspension were pipetted onto the PLA textile. Onto the PET/PA textile, 10 times 15 μ L were pipetted. The nanoparticles suspension was allowed to dry at room temperature. For comparative Raman and SERS experiments, 15 μ L of pesticide stock solution were transferred onto the substrate. For model samples, lettuce leaves from a local supermarket were applied with 15 μ L of the pesticide stock solution. After evaporation of the solvent, the pesticide remained on the lettuce. The substance was re-uptaken by pipetting 15 μ L of deionized water onto the substrate and transferring the solution onto the SERS substrate. Raman and SERS spectra were recorded using an IDRaman Mini 2.0 handheld spectrometer (Ocean Insight, USA) with a spectral range from 400 cm⁻¹ to 2300 cm⁻¹ and a resolution of 12–14 cm⁻¹. The excitation laser wavelength was 785 nm with a laser power of 100 mW. For spectral processing, 32 spectra were accumulated and averaged, smoothed with a Savitzky–Golay filter over 11 points and a polynomial of grade 3 using Matlab R2019b, Update 3 (The MathWorks, Inc., USA). Raster orbital scanning was utilized accumulating 10 acquisitions. Statistical testing was performed in Matlab as well. Testing for significance was carried out using Student's t-test. The t-test value was chosen for a significance level of 5%.

4.4 Results & Discussion

Characterization of Gold Nanoparticles

Gold nanoparticles were synthesized following Turkevich and Frens.^{27,29} Characterization was carried out using imaging techniques, that is, TEM and absorption spectroscopy. The TEM results showed that nanoparticles with an average diameter of 33.80 nm and polydispersity of 7.44 nm were obtained through the synthesis route (Fig. 4.1a). The first centrifugation increased the average diameter to 36.81 nm with a polydispersity of 6.45 nm (Fig. 4.1b). The second centrifugation concentration step further increased the average diameter of the gold nanoparticles to 39.60 nm with a polydispersity of 5.52 nm (Fig. 4.1c). Thus, the polydispersity was reduced by 25.81%, while the mean diameter was increased by 17.04%. The observed size and polydispersity as consequence of the repeated centrifugation are in line with previous studies.²⁷⁻²⁹ Hence, the particle size obtained indicated the necessity of repeated centrifugation to achieve a particle size of about 40 nm. Figure 4.1d) shows the particles to be spherical. Furthermore, a more uniform SERS enhancement can be expected from the lower polydispersity. This relationship was described earlier.³¹ Hence high uniformity in size and shape of the nanoparticles is key to achieving homogenous and uniform SERS enhancement. The absorption spectra corresponding to the concentration by centrifugation are shown in Fig. 4.2a. As expected from the TEM images and the size derived, the absorption maximum became more prominent along the concentration series. Comparing the spectrum from the last centrifugation step with that of the nanoparticle reference standard, the absorption band width of the latter appeared smaller: full width at half-maximum (FWHM) of 59 nm as compared to FWHM of 88 nm. Hence, the nanoparticles synthesized in this work were found more dispersed than the nanoparticles from the reference standard. As can be seen in Fig. 4.1, centrifugation caused concentration of the particles but also reduction of the dispersity. Since smaller and thus lighter particles remained mainly in the supernatant, the lower end of the particle size distribution was shortened successively by centrifugation. More frequent repetition might lead to decrease dispersity up to the level of the reference standard. The maximum of the absorption band of the nanoparticles from synthesis and centrifugation was observed at 535 nm, while that of the reference nanoparticles was detected at 532 nm. Since larger nanoparticles are known to cause a red shift of the surface plasmon band, it might be assumed that the nanoparticles of this work were larger than those of the reference. Since the absorption band also depends on the dispersity, the difference of 3 nm might not be considered significant as supported by the TEM results.

When simulating the absorption spectrum (Fig. 4.2b, purple line) for spherical gold nanoparticles of 40 nm using MiePlot, a band was predicted with a maximum at 551 nm and an FWHM of 66 nm. The deviation between the calculated and the experimentally determined particle-size band position was hence large such that MiePlot proved of lesser value for the particle-size determination at this point. For the determination of the of gold nanoparticle concentration, a dilution series of the reference standard was used. Absorption spectra of the series are provided in Fig. 4.2c. Based on the intensities of the absorption

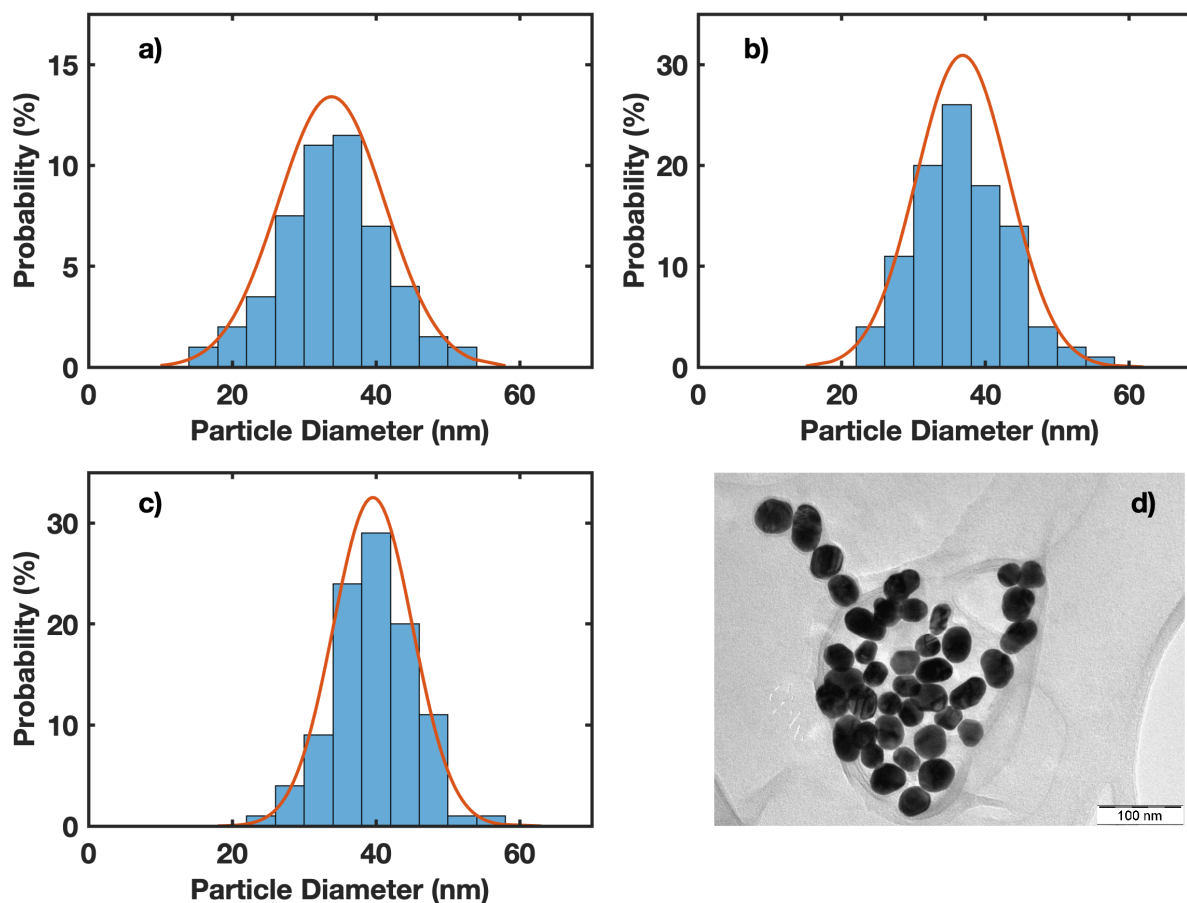


Figure 4.1 – (a–c) Size distribution of gold nanoparticles from synthesized gold nanoparticles and successive centrifugation steps and (d) transmission electron microscopy images. The size distribution of the nanoparticles from synthesis (a) yielded a mean diameter of 33.80 nm and a polydispersity of 7.44 nm, after the first concentration step (b) a mean diameter of 36.81 nm and a polydispersity of 6.45 nm and after the second concentration step (c) a mean diameter of 39.60 nm and a polydispersity of 5.52 nm.

bands of the centrifuged nanoparticle solutions from Fig. 4.2a, concentrations could be derived from the calibration function of the reference standard (Fig. 4.2c). A concentration of 7.85×10^{10} particles/mL was determined for the synthesized nanoparticles. After the first centrifugation, a concentration of 3.31×10^{11} particles/mL was obtained and 8.04×10^{11} particles/mL after the second centrifugation step. The concentration of nanoparticles was hence increased 10 times through twofold centrifugation. The deep purple color of the concentrated nanoparticle suspension can be recognized in Figure 4.8 (Supplemental Material).

Characterization of Surface-Enhanced Raman Spectroscopy Active Gold Nanoparticle Substrates

The PLA fabric with a drop of dark red gold nanoparticle solution is shown in Figure 4.8 a) (Supplemental Material). The hydrophobic character of the textile can be recognized since the drop did not disperse on the woven textile but retained its shape. The hydrophobicity is due to the methylated material.³² This property enabled drying of the gold nanoparticle

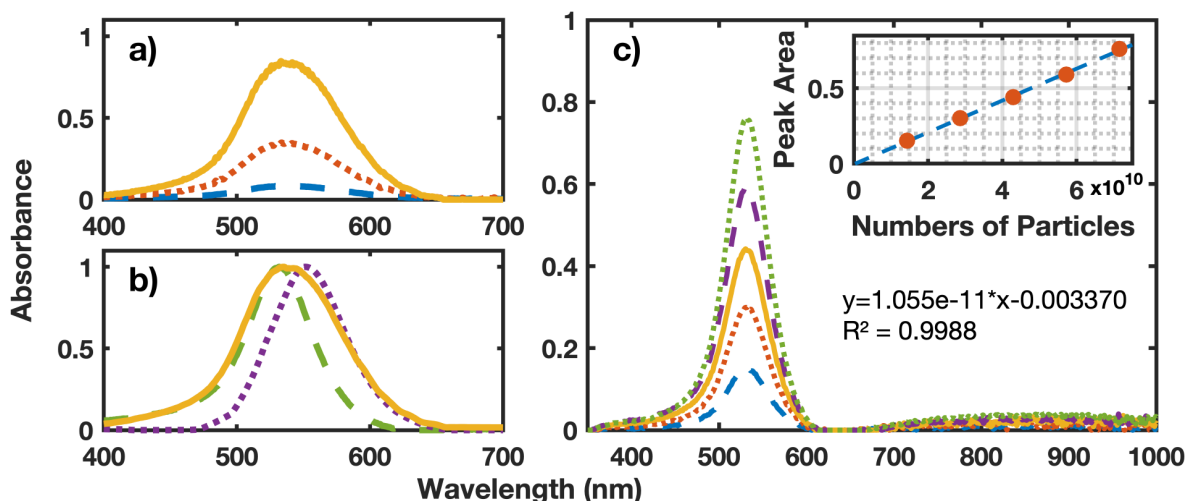


Figure 4.2 – Absorption spectra of the gold nanoparticle solutions: (a) nanoparticles as yielded through the synthesis (blue, lowest), after first centrifugation (red, middle) and after second centrifugation (yellow, highest); (b) after second centrifugation (yellow), nanoparticle reference standard (green) and simulated by MiePlot (purple); (c) calibration series from reference standard dilution, calibration function and its diagram peak area vs. number of particles (insert).

solution in a defined area (Figure 4.8). SEM images also demonstrated that a large proportion of the nanoparticles remained on the textile surface (Figures 4.9 a and 4.9 b, Supplemental Material), while in the case of PET/PA the nanoparticle suspension penetrated the textile when wet (Figure 4.8 c). As a consequence, the nanoparticles were distributed over a wider area and same was the case for PLA. In a dry state, the nanoparticle spot did not increase like in the wet state (Figure 4.8 d). Yet, nanoparticles might be more concentrated at the outer limit of the drop due to the coffee ring effect.³³ Nevertheless, the flow of the nanoparticle suspension into the textile core suggested that the overall concentration of nanoparticles on the surface was lower than that on the PLA woven textile substrate. The SEM images of the PET/PA (Figure 4.9 c) and Figure 4.9d, Supplemental Material), revealed that the PET/PA fibers were smaller than the PLA fibers, resulting in a smoother surface of the woven PLA textile. Similarly, the SEM images in Figure 4.9 indicated significantly more gold nanoparticles on the surface fibers of the woven textile. In summary, due to its hydrophobic effect, more nanoparticles resided in a more confined area on PLA. Since a higher density of nanoparticles will lead to a stronger SERS enhancement and thus a higher sensitivity of an analytical method, PLA seemed the more promising substrate at that point. To test this hypothesis and also the effect of concentration by centrifugation on SERS enhancement, the three concentration levels of gold nanoparticles were applied to both types of textiles using imidacloprid as model analyte. For comparison purpose, the Raman spectrum of imidacloprid is shown in Figure 4.8 a), as well as the Raman and SERS spectra of PLA textile and PLA textile equipped with gold nanoparticles (Figure 4.8 b), and PET/PA textile and PET/PA textile equipped with gold nanoparticles (Figure 4.8 c), for the recognition of background signals. Using increasing concentrations of nanoparticle solution in substrate preparation gave indeed rise to larger SERS enhancement, e.g. the concentration

of 8.04×10^{11} particles/mL yielded the most intense SERS spectrum on both textiles. The SERS spectra of imidacloprid recorded with the most concentrated nanoparticles and both types of textiles (Figures 4.11 a) and b). The most intense peak of the PLA background arose at 871 cm^{-1} . In general, the Raman signals of the PLA woven textile were significantly less intense than those of the PET/PA woven textile. The signals of PLA varied around 2000 counts and the signals of PET/PA woven textile amounted to 15 000 counts. In addition, PET/PA showed more characteristic signals than PLA. The most intense signals of the PET/PA woven textile were observed at 632 cm^{-1} , 857 cm^{-1} , 1287 cm^{-1} , 1615 cm^{-1} , and 1728 cm^{-1} (Figure 4.11). To find suitable concentrations of the nanoparticles for preparing SERS active substrates, the PLA peak at 871 cm^{-1} was used in the SERS spectra and the signal at 1615 cm^{-1} were used for PET/PA. Therefore, these signals needed to be minimized as much as possible through preparation of the SERS substrates. As a quality parameter, the ratio of the imidazole C-N-N stretching band of imidacloprid at 1457 cm^{-1} and selected signals of the textile materials was calculated. These data are compiled in Tables 4.2 and 4.3 (Supplemental Material). In the case of the PLA substrate, the ratio could be increased from 0.67 for the untreated nanoparticles to 1.71 after two centrifugation steps when applying the solutions on a single layer of the PLA textile (Table 4.2). For the PET/PA substrate, the concentration of nanoparticles led to an increase from 0.09 for the single layer PET/PA substrate and nonconcentrated nanoparticles to 9.34 for the single layer PET/PA substrate with doubly concentrated nanoparticles (Table 4.3). Hence, with both textiles the twice centrifuged nanoparticles produced the best signal enhancements. For further improvement, different types of textile layers were investigated and evaluated according to the signal ratio. The signal ratio for the PLA substrate was augmented from 1.71 for a single-layer substrate to 2.18 for a double-layer substrate applying doubly concentrated nanoparticles. Using double-layer pressed substrates of PLA, an increase of the signal ratio was found to be 3.51. For the PET/PA substrate, findings were different. The single layer substrate with the twofold concentrated nanoparticles already yielded a good signal ratio of 9.43, which could not be improved using a double-layer or double-layer pressed substrate (Table 4.3, Supplemental Material). The double-layer and double-layer pressed substrates showed signal ratios of 1.44 and 3.47, respectively. This result was attributed to the absorbent effect of PET/PA causing the nanoparticles to penetrate deeper and to be more distributed in the woven textile. An even and deep distribution would lead to a weaker enhancement as compared to a focused spot near the surface. In summary, the double-layer pressed substrate with twice concentrated nanoparticles showed highest enhancement of the imidacloprid signals among the PLA substrates (Fig. 4.3a). In the case of the PET/PA substrate, the single-layer substrate with twice concentrated nanoparticles displayed the best enhancement for imidacloprid analysis (Fig. 4.3b). Taking the enhancement into account, PET/PA proved the better substrate for imidacloprid. The lower background signals of PLA could not compensate for the much stronger enhancement by PET/PA substrates. Nevertheless, both textile substrate types were tested for inter-substrate reproducibility as analytical parameter.

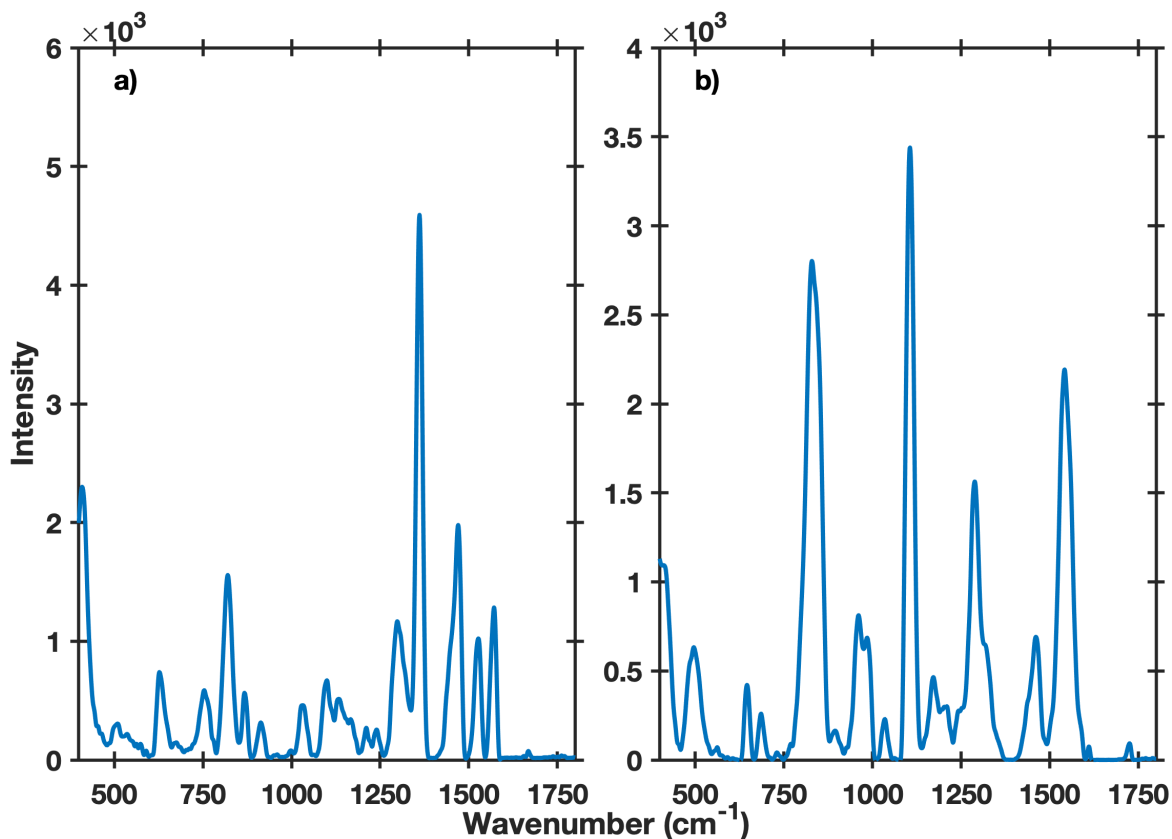


Figure 4.3 – Surface enhanced Raman spectroscopy spectra of imidacloprid on (a) a two-layer pressed PLA substrate with twice-concentrated nanoparticles, and on (b) a single layer PET/PA with twice-concentrated nanoparticles. Spectral differences are due to the background signals arising from the textile fabrics and due to the distribution and penetration of the nanoparticles in the textile materials.

Inter- and Intra-Substrate Reproducibility

By comparing the spectra of imidacloprid on PLA and PET/PA substrate, the observed signal patterns differ (Fig. 4.3). Background signals from the textile were still visible in the spectra, albeit weakly. Exemplarily, the signal at 871 cm^{-1} (Fig. 4.3a) originated from PLA. Analogously, the weak signal at 1660 cm^{-1} stemmed from PET/PA (Fig. 4.3b). The imidacloprid signals showed different intensities and linewidths. On both textile substrates, the peaks at 820 cm^{-1} , 1100 cm^{-1} , 1298 cm^{-1} , and 1456 cm^{-1} were enhanced. The peak at 820 cm^{-1} was attributed to a C–C–C in-plane bending vibration of the pyridine moiety, the band at 1100 cm^{-1} from a C–C–C breathing of pyridine and imidazole group, that at 1298 cm^{-1} from a methylene bending of the imidazole moiety, and the peak at 1470 cm^{-1} was assigned to the C–N–N stretching vibration of the imidazole group. The complete assignment of the vibrations is compiled in Table 4.4 (Supplemental Material). The peak at 1542 cm^{-1} in the spectrum of imidacloprid on PET/PA (Fig. 4.3), corresponded to two separate peaks in the spectrum of imidacloprid on PLA. These frequencies were assigned to the C–N–N stretching, 1470 cm^{-1} , and to the NO_2 asymmetric stretching from the nitro group, 1580 cm^{-1} . While the peak at 1362 cm^{-1} which stems from a CH_2 bending from the imidazole group was enhanced on PLA, it was not on PET/PA. This may be explained as due to the nonuniformity of the substrates, as

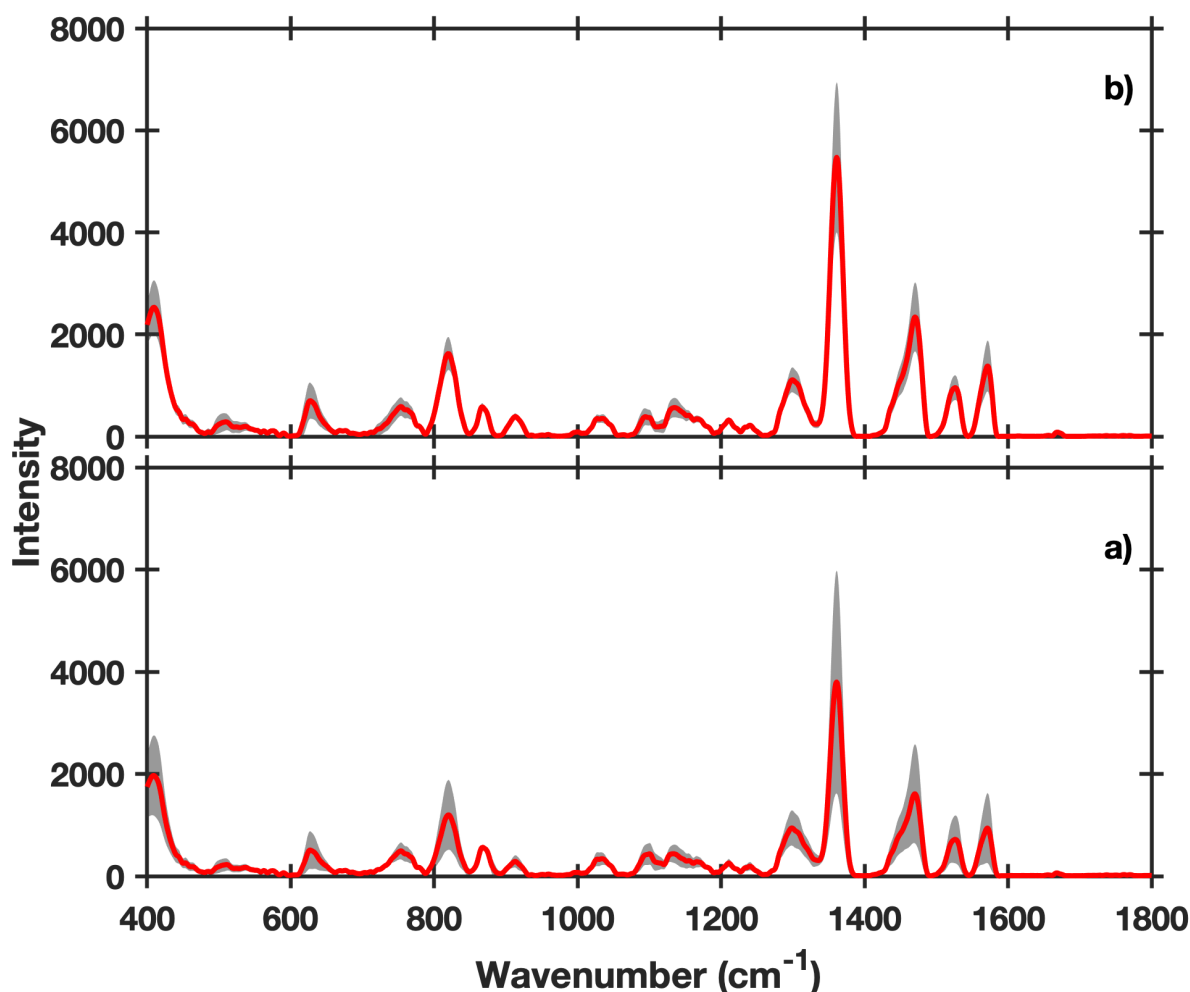


Figure 4.4 – Surface enhanced Raman spectroscopy spectra of imidacloprid on double pressed layer PLA and twice centrifuged nanoparticles: mean spectra (red) and standard deviation (gray). Spectral recording (a) on five different spots of the same substrate, and (b) on three different substrates. RSD value of 7.5% for intra-substrate and 27.35% for inter-substrate reproducibility.

nanoparticles of different sizes would enhance the imidacloprid signal differently.³⁴ It might be assumed that the PET/PA material, which is often used as filter material, retained the larger nanoparticles on the surface of the textile, but let the smaller nanoparticles enter into deeper layers of the material. As a consequence, the signals of imidacloprid on PET/PA were significantly more enhanced. It is known that different spectra of imidacloprid result from different SERS substrates. Chen et al. reported peaks at 680 cm^{-1} , 990 cm^{-1} , and 1360 cm^{-1} , where only the peak at 1360 cm^{-1} matched the signals in this study.³⁵ Yet, Dowgiallo and Guenther observed signals at 820 cm^{-1} , 1280 cm^{-1} , and 1457 cm^{-1} , which is in agreement with this study.³⁶ Further signals deviating in frequencies were reported elsewhere.^{37,38} These different observations clearly show that the nature of the SERS substrate has a significant impact on the SERS spectrum of the analyte, emphasizing the need for robust, reproducible substrates available in large quantities. In the following, PLA and PET/PA will be further examined with respect to intra-substrate reproducibility. Figures 4.4 and 4.5 present replicate

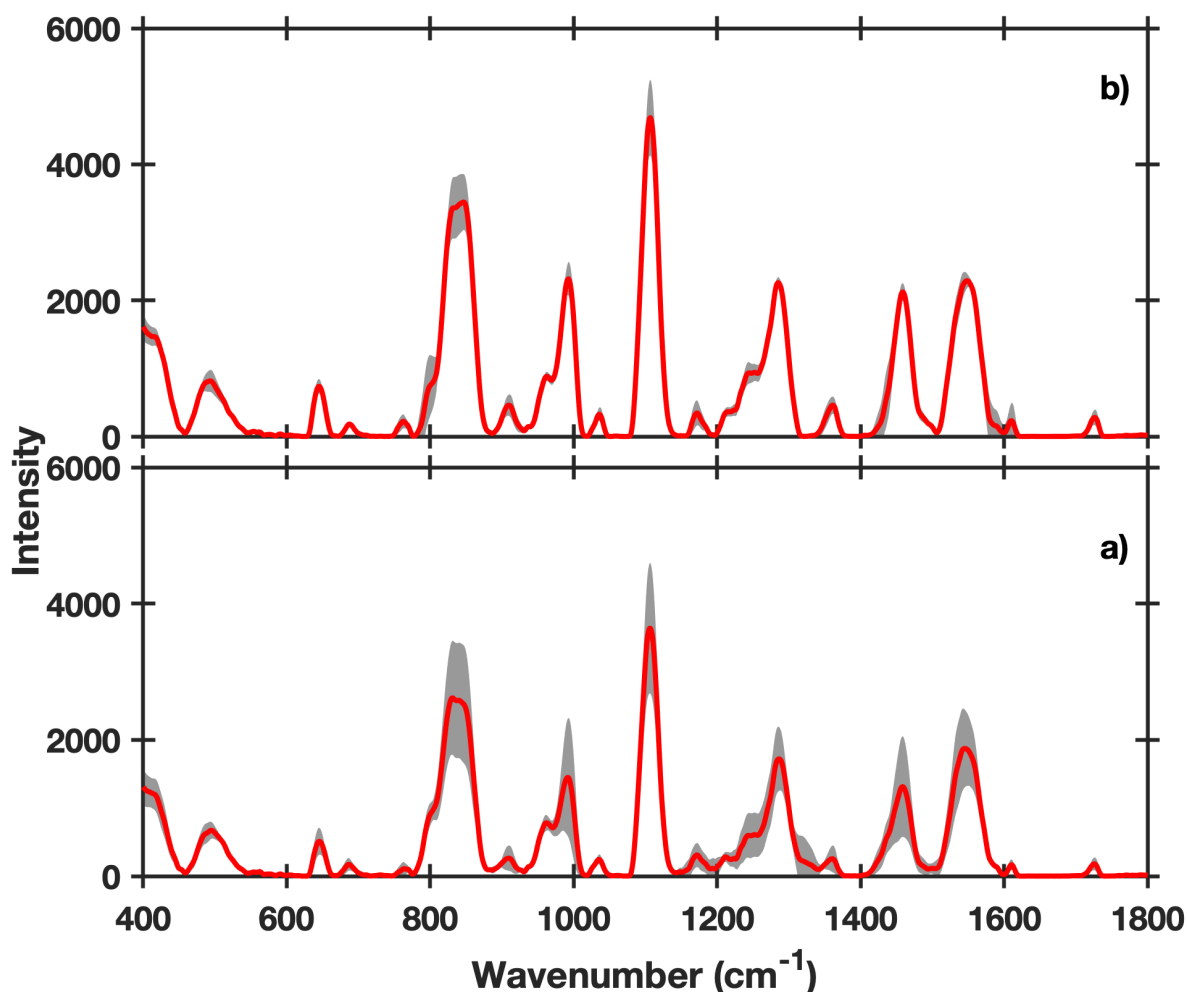


Figure 4.5 – Surface enhanced Raman spectroscopy spectra of imidacloprid on single-layer PET/PA with twice centrifuged nanoparticles, mean spectra (red) and standard deviation (gray). Spectral recording (a) on five different spots of the same substrate, and (b) on three different substrates. RSD value of 6.5% for intra- and 14.70% for inter-substrate reproducibility.

spectra of imidacloprid recorded at different spots on the same substrate and on three independently prepared substrates. As can be recognized, the signal frequencies did not vary. Variations were observed in the overall intensity while relative intensity distributions remained constant. In more detail, the peak at 1456 cm^{-1} observed from measurements of five different spots with PLA (Fig. 4.4) yielded a relative standard deviation (RSD) of 7.5% (Figure 4.13 a, Supplemental Material). The RSD for the three replicate PLA substrates was found to be 27.35%. As would be expected, the inter-substrate reproducibility was inferior to the intra-substrate variation. Despite of RSD values larger than 25%, it would be possible to create a spectral library and to detect and identify imidacloprid using a PLA substrate, as the spectral difference resulted only from varying peak intensities not from peak shifts. When choosing handheld or fieldable spectrometers, the set-up might also allow on-site identification. The spectra PET/PA substrate textile proved reproducible as well. Again, five spots on the same substrate were probed and compared to the mean spectrum

(Fig. 4.5a). An RSD of 6.5% was obtained for variation of the peak at 1456 cm^{-1} when using PET/PA as substrate (Figure 4.11b). The reproducibility of the signal was confirmed for three different PET/PA textile substrates (Fig. 4.5b). A RSD value of 14.7% was calculated. The PET/PA substrate thus showed higher reproducibility as compared to the PLA substrate, this increased reproducibility may be explained as due to the absorbent effect of the material. Although fewer nanoparticles were observed on the textile surface by SEM, their distribution appeared more homogeneously. Since for the PLA substrate imidacloprid signal frequencies remained substrate spot and batch independent as well as for the PET/PA substrates, spectral library matching is possible. Yet, signal intensities were clearly different over several PLA substrates, which renders quantitation impossible. These differences were found significant based on results from Student's t-testing (Table 4.5, Supplemental Material). However, the handheld Raman spectrometer method might prove useful as a method complementary to standard routine methods. The method may be particularly interesting for random sampling. Samples could be analyzed quickly and cost-efficiently on large fields. Positive testing for imidacloprid may induce more precise analyses using the standard methods such as liquid chromatography (LC-) and gas chromatography-mass spectrometry (GC-MS).

Investigation of Thiram and Paraquat

Both substrates were eventually applied to two more analytes. The resulting SERS spectra of thiram and paraquat are shown in Fig. 4.6. For comparison purposes, the Raman spectra of the solids are displayed as well. Differences were observed for the SERS spectra of thiram on PLA and PET/PA. Signals were found at 439 cm^{-1} , 555 cm^{-1} , 920 cm^{-1} , 1145 cm^{-1} , 1368 cm^{-1} , 1395 cm^{-1} , and 1459 cm^{-1} . The main pattern of the spectra was conserved in both SERS spectra, while a major difference was recognized for the signals at 1041 cm^{-1} and 1499 cm^{-1} . While the SERS signal intensity at 1041 cm^{-1} was reduced as compared to the Raman signal, the SERS signal at 1499 cm^{-1} was clearly more intense. The main difference between the Raman spectrum of the solid and the SERS spectra of thiram was the enhancement of the bands at 555 cm^{-1} and 1377 cm^{-1} , where the band at 555 cm^{-1} was less amplified in the SERS spectrum and appeared less intense in the pattern of the spectrum as compared to the other bands. The band at 1368 cm^{-1} was amplified. The investigation of paraquat yielded similar results. The SERS spectra on the different substrates show hardly any deviations from each other. For paraquat, the difference between Raman and SERS spectra were found smaller than that for thiram. The main SERS signals for paraquat appeared at frequencies 845 cm^{-1} , 1201 cm^{-1} , 1297 cm^{-1} , and 1659 cm^{-1} . Only the signal at 1230 cm^{-1} was not observed in the SERS spectrum, while the peak at 1659 cm^{-1} was amplified. A detailed assignment of the signals of thiram and paraquat can be found in Tables 4.6 and 4.7 (Supplemental Material). Precision tests yielded an intra-substrate RSD value for thiram on PET of 3% and an inter-substrate RSD of 4%. For the PLA woven textile, values were 3% and 6% for intra-substrate and inter-substrate RSDs, respectively. For paraquat, the variations were found larger. The intra-substrate RSD value for paraquat on PET was 10% and 14% between substrates. Paraquat on PLA substrate showed an intra-substrate lower deviation of 5% but

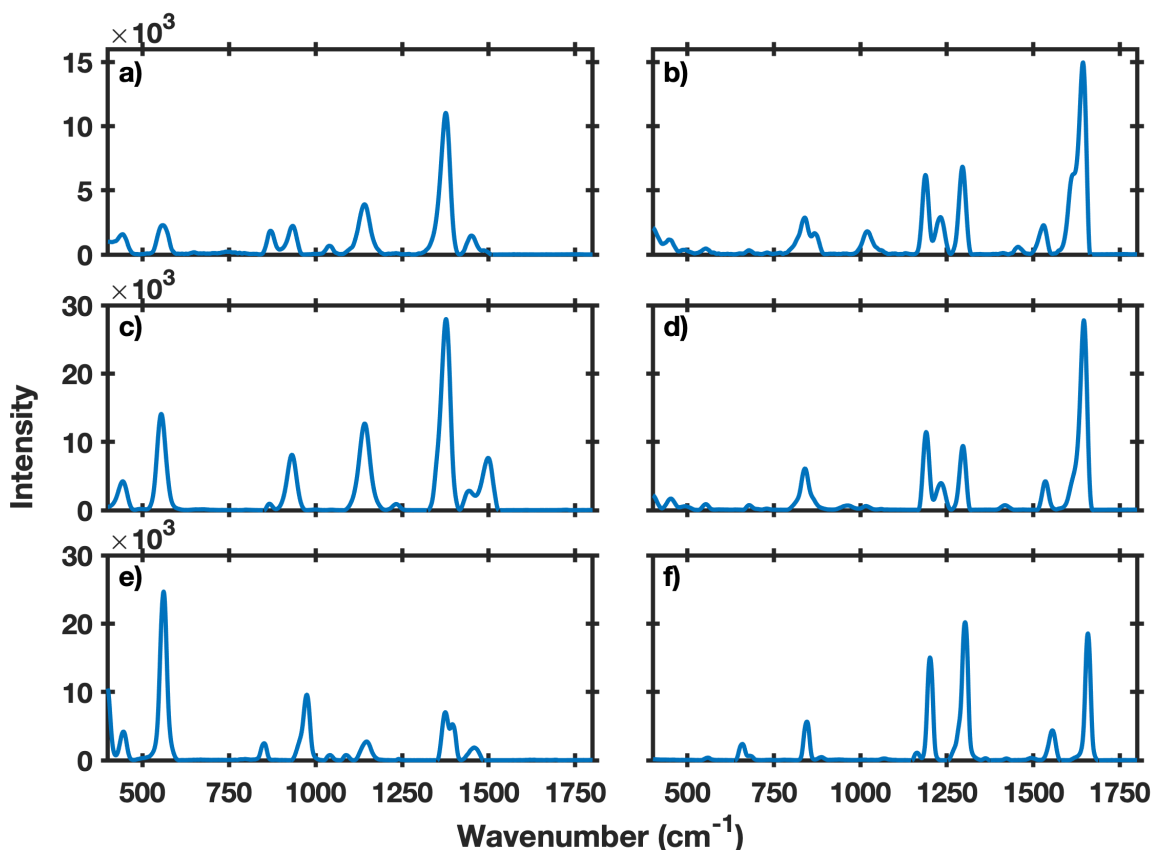


Figure 4.6 – Surface enhanced Raman spectroscopy spectra of thiram (left) and paraquat (right) on PLA substrate (a,b) and on PET/PA substrate (c, d) and Raman spectra of pure solids (e, f). Pesticide signal frequencies correspond in Raman and SERS spectra. Signal intensity differences between SERS and Raman spectra arise from different enhancements.

Table 4.1 – LODs for imidacloprid, thiram, and paraquat using PLA and PET/PA substrates, twice concentrated nanoparticle solutions and surface enhanced Raman spectroscopy detection.

Analyte	LOD	
	PLA	PET/PA
	m (ng)	m (pg)
Imidacloprid	3	600
Thiram	3	1100
Paraquat	2	960

15% between substrates. Finally, the potential of the method towards fast and easy trace analysis was investigated. To this purpose, the limit of detection (LOD) was determined. The values are compiled in Table 4.1. In addition, the performance of the substrates was estimated by the enhancement factor for paraquat. The enhancement factor was estimated to 10^7 for thiram and paraquat on both substrates following the common method.³⁹ LODs were calculated on the most intense signal in the SERS spectrum. The noise was sampled over a range of 100 cm^{-1} devoid of signals. For the LODs for imidacloprid, thiram, and paraquat, somewhat lower, that is, better, LODs were possible when using the PET/PA woven textile as gold nanoparticle support. Hence, LODs in the lower nanogram region were found attainable. A previous study could demonstrate that this sensitivity range should suffice

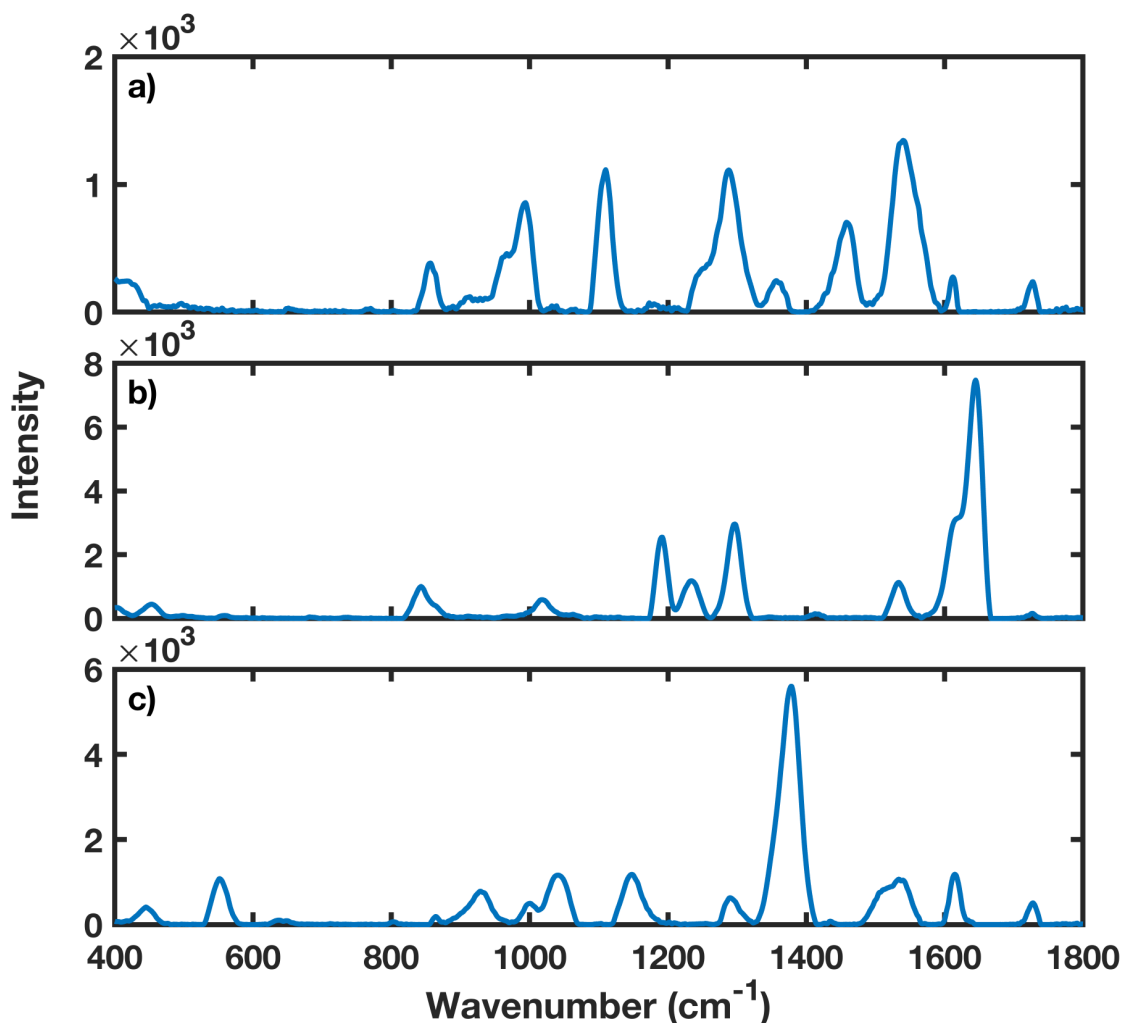


Figure 4.7 – Surface enhanced Raman spectroscopy spectra of (a) imidacloprid, (b) paraquat, and (c) thiram recovered from pesticide-treated model samples of lettuce leaves. Pesticide signals are most intense. Lettuce matrix signals, that is, carotenoid resonances, are found around 1500 cm^{-1} .

for on-site identification, for example, of pesticides on plants.²⁵ It can hence be concluded that the SERS method would be suitable for the identification of the pesticides imidacloprid, paraquat, and thiram.

Model Samples

Model samples were prepared and SERS spectra recorded for the three pesticides under investigation (Fig. 4.7). Lettuce leaves served as model for other vegetables. Observed signals showed that the pesticides were detected after retrieval from the model samples within the limits of detection provided in Table 4.1. Since PET/PA proved the better SERS substrate, model samples were investigated using this substrate. For imidacloprid, signals showed good agreement with the previously recorded spectrum at high wavenumbers. The intensity of the peak at 1100 cm^{-1} was attenuated. At low wavenumbers, no signals were observed for imidacloprid retrieved from the model sample. Yet identification based on the total spectrum was still possible. A more pronounced decrease in signal intensity was found

for thiram across the entire spectrum as compared to the reference spectra. This observation could be traced back to the incomplete recovery from the lettuce matrix. A minor signal from the lettuce matrix was observed around 1500 cm^{-1} . Carotenoids show signals at $1150\text{--}1170$ and $1500\text{--}1550\text{ cm}^{-1}$, whereas chlorophylls would lead to much weaker bands around 980 and 1380 cm^{-1} .⁴⁰ Hence, the signal might be interpreted as the most intense carotenoid band. A lesser intensity as expected was also found for paraquat, indicating again an incomplete retrieval. Yet, thiram and paraquat were clearly more reliably identified than imidacloprid via the SERS spectra recorded after recovery from model samples. There was no spectral interference from carotenoids or similar plant constituents, as the typical carotenoid or chlorophyll peaks were not observed except for the thiram sample. In summary, the spectral quality was sufficient to allow for identification of imidacloprid, thiram, and paraquat from lettuce leaves when treated with the pesticides in concentration ranges corresponding to the limit of detection.

4.5 Conclusion

Using PLA and PET/PA textiles treated with concentrated gold nanoparticle solution in combination with a handheld Raman spectrometer allowed for a sensitive fast, easy, and sustainable identification method for the pesticides imidacloprid, paraquat, and thiram. Nanoparticles were characterized by TEM and absorption spectroscopy to be 8.04×10^{11} particles/mL, of size 40 nm , and 5.5 nm dispersity. Green textiles were successfully applied as supports with PLA giving rise to minimum background and PET/PA yielding the highest signal enhancement 10^7 . PLA required less nanoparticles but a pressed double-layer support while one layer of PET/PA proved sufficient. With respect to reproducibility and precision, intra- and inter-substrate RSDs of PET/PA, 7% and 15%, were superior to PLA, 8% and 27%. LODs for PET/PA were found as low as 1000 pg for the three pesticides while PLA allowed for 3 ng . Imidacloprid, thiram, and paraquat could be identified after recovery from pesticide-treated lettuce-leaf model samples. Therefore, PET/PA woven textile in combination with concentrated gold nanoparticles might provide green SERS substrates for in-field analytics for pesticide identification. By optimizing the shape of the diameter, the agglomeration procedure to yield more hot-spots and the application onto the textile to obtain more uniform patterns, the limit of detection may be ameliorated. The optimization should also lead to decreasing inter- and intra-substrate variations.

4.6 Supplemental Information

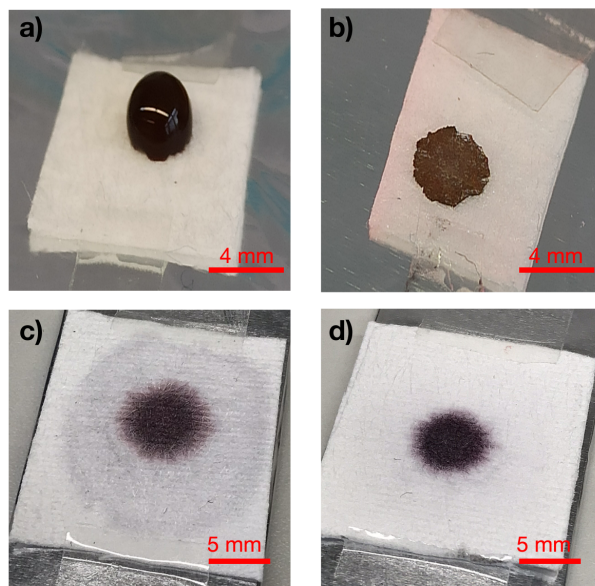


Figure 4.8 – Photographs of twice-concentrated gold nanoparticle solution on PLA textile (a) before and (b) after drying, and on PET/PA textile (c) before and (d) after drying.

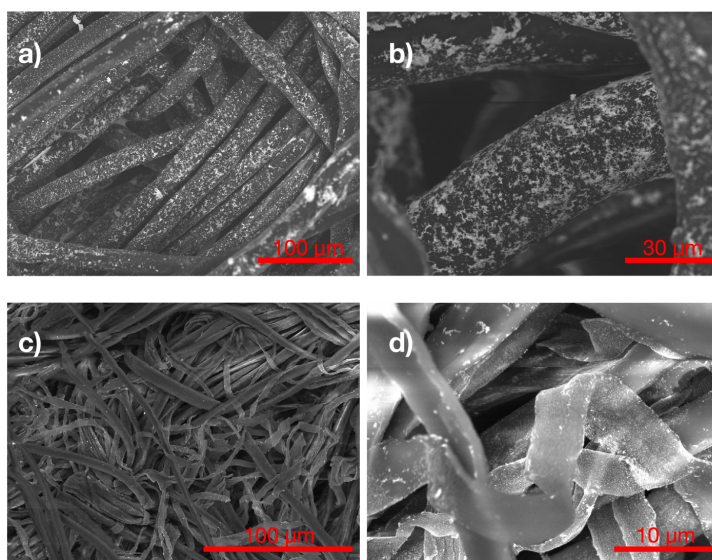


Figure 4.9 – SEM images of PLA magnification (a) 600, (b) 2000, and of PET/PA magnification (c) 1000 and (d) 7000.

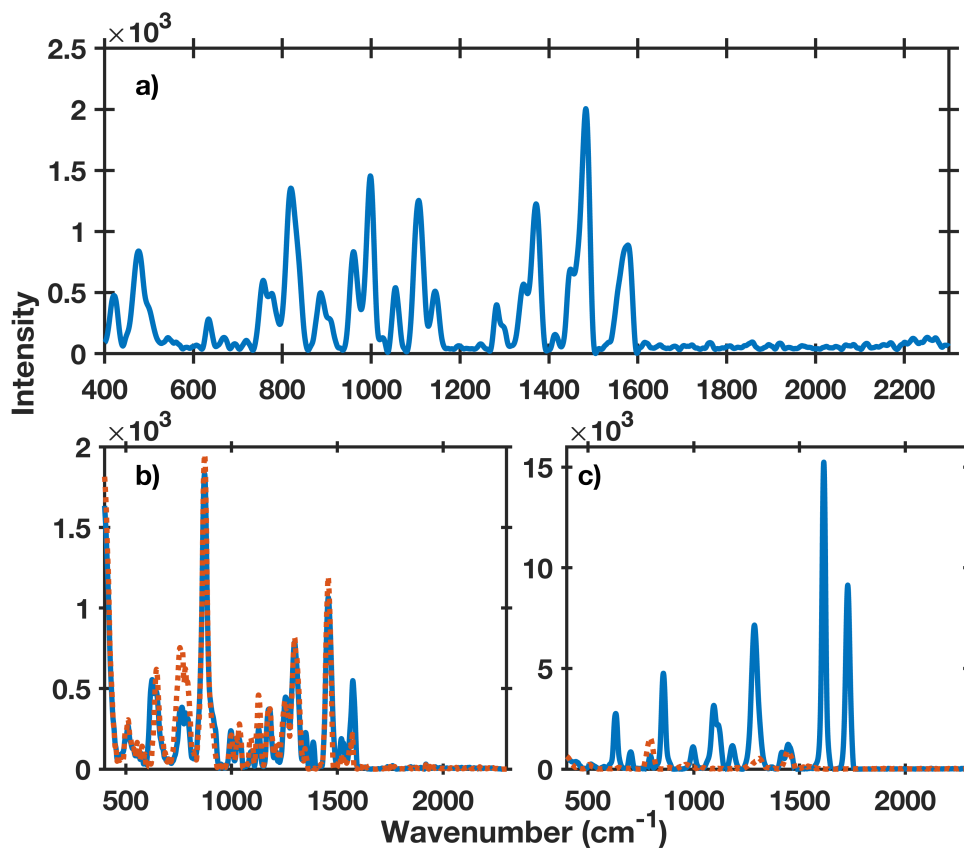


Figure 4.10 – Raman spectrum of (a) imidacloprid as solid and spectra of (b) PLA textile (blue, solid line) and PLA textile equipped with gold nanoparticles (red, dotted line), and (c) PET/PA textile (blue, solid line) and PET/PA textile equipped with gold nanoparticles (red, dotted line).

Table 4.2 – PLA Ratio.

Type of PLA substrate	Signal at 871 cm^{-1}	Signal at 1456 cm^{-1}	Ratio of imidacloprid and substrate signal
One layer and raw NP	504	339	0.67
One layer and 1× centrifuged NP	517	579	1.12
One layer and 2× centrifuged NP	552	946	1.71
Two layers and 2× centrifuged NP	641	1395	2.18
Two layers pressed and 2× centrifuged NP	564	1978	3.51

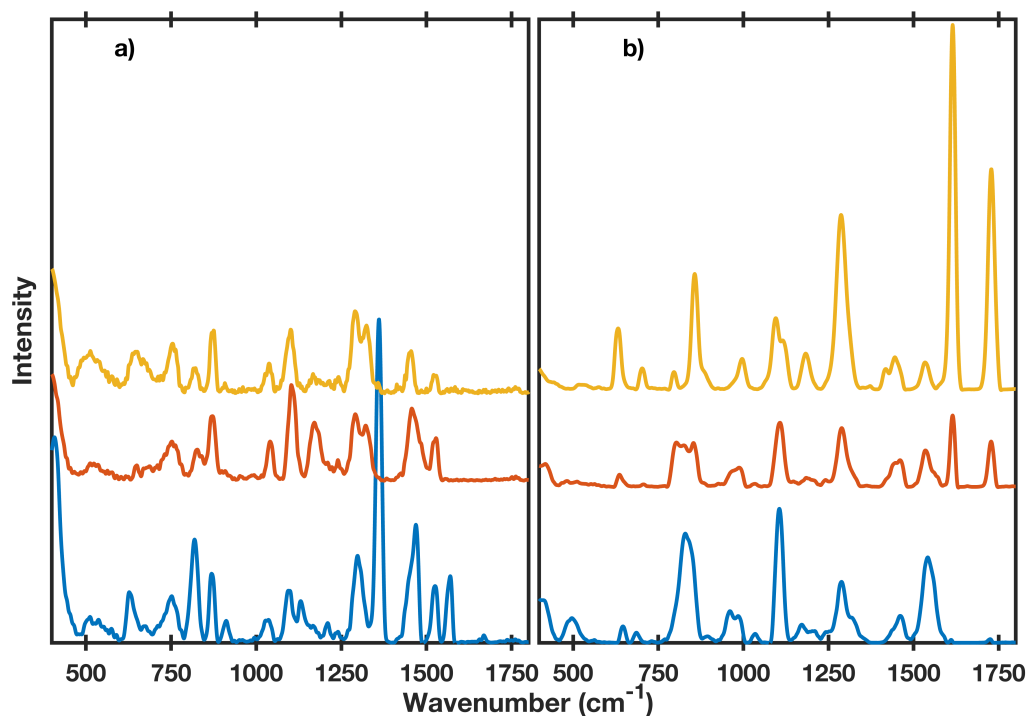


Figure 4.11 – SERS spectra of imidacloprid with nanoparticle suspension from synthesis (yellow line, top), nanoparticles centrifuged once (red line, middle) and twice centrifuged nanoparticles (blue line, bottom) on (a) PLA textile and (b) PET/PA textile.

Table 4.3 – PET /PA Ratio.

Type of PET/PA substrate	Signal at 871 cm ⁻¹	Signal at 1456 cm ⁻¹	Ratio of imidacloprid and substrate signal
One layer and raw NP	9357	828	0.09
One layer and 1× centrifuged NP	1834	686	0.37
One layer and 2× centrifuged NP	74	691	9.43
Two layers and 2× centrifuged NP	444	638	1.44
Two layers pressed and 2× centrifuged NP	307	1065	3.47

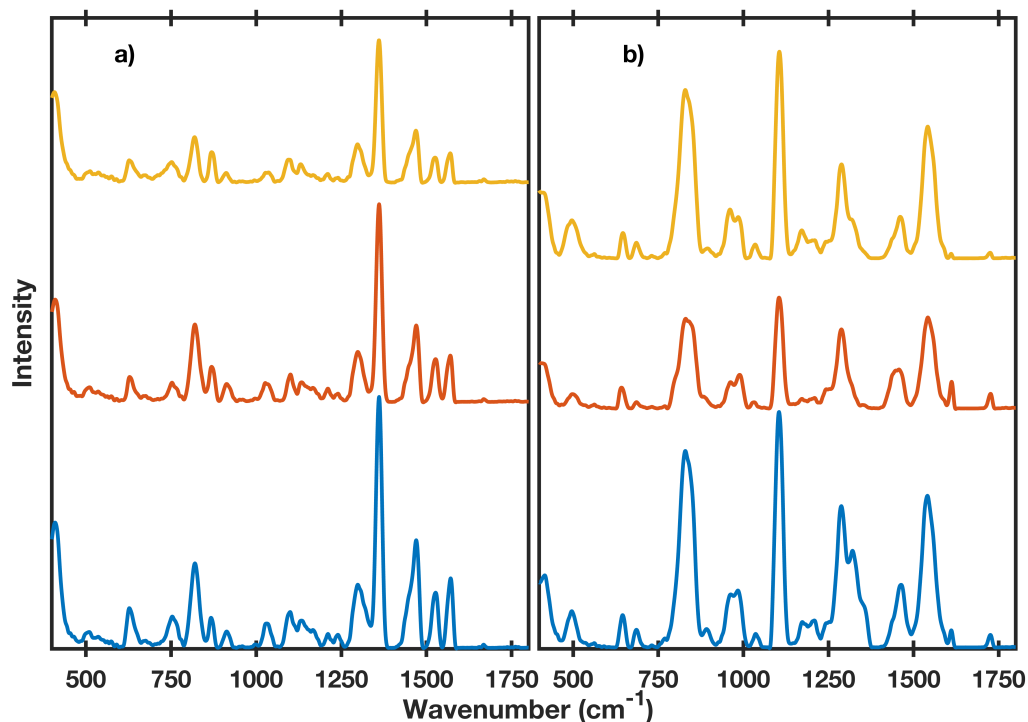


Figure 4.12 – SERS spectra of imidacloprid with twice concentrated nanoparticle suspension on single layer textile (yellow line, top), double layer textile (red line, middle) and pressed double layer textile (blue line, bottom) with (a) PLA textile and (b) PET/PA textile.

Table 4.4 – Assignment of imidacloprid vibrations.

Raman (cm^{-1})	wavenumbers	Assignment
755		C–C–C puckering
770		NO_2 asymmetric stretching
818		C–C–C in plane bending
886		C–C–N bending
960		C–C–N symmetric ring stretching
998		C–N symmetric stretching
1053		C–N asymmetric stretching
1104		C–C–C breathing
1141		C–N stretching
1279		CH_2 bending
1371		CH_2 bending
1451		C–C stretching
1481		C–N–N stretching
1580		NO_2 asymmetric stretching

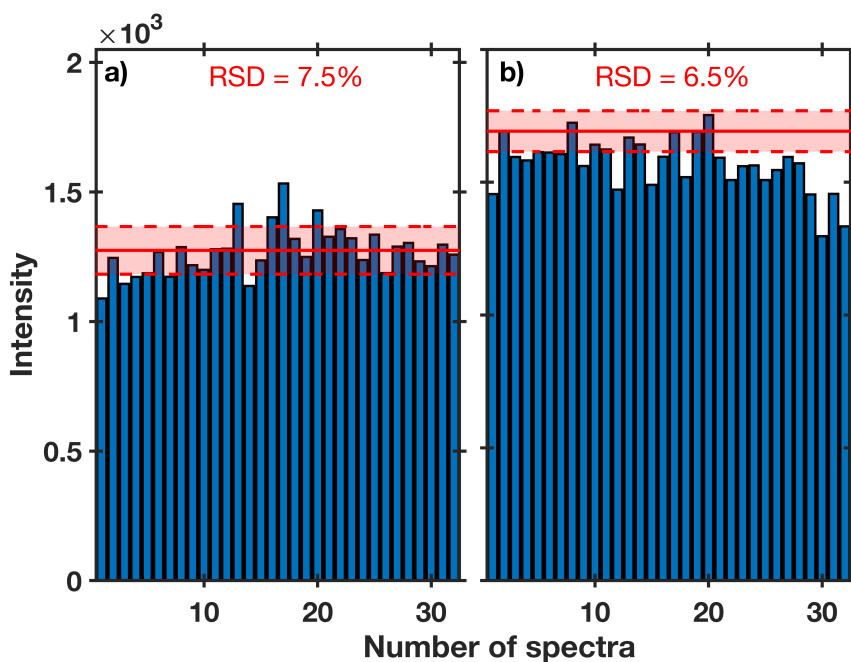


Figure 4.13 – Intensity of imidacloprid peak at 1456 cm^{-1} for (a) PLA and (b) PET/PA substrate with mean intensity and RSD value over 32 spectra.

Table 4.5 – Results from Student’s t-test for imidacloprid.

Parameter	Value
Mean intensity of PLA Peak at 1456 cm^{-1}	724.79
Mean intensity of PET/PA Peak at 1456 cm^{-1}	988.48
t-Value	-0.52
P-Value	0.31
Confidence	69%
Significance ^a	No

^a Hypothesis: Two values are equal. If significance equals no, then values are different.

Table 4.6 – Assignment of thiram vibrations.

Raman (cm^{-1})	wavenumbers	Assignment
439		C-N-C deformation
555		C=S stretching
998		asym. C-H deformation

Table 4.6 – Assignment of thiram vibrations. (*continuation*)

Raman (cm^{-1})	wavenumbers	Assignment
1145		S-S stretching
1368		C-N and S=S stretching
1395		C-H rocking, C-N stretching
1459		C-N stretching

Table 4.7 – Assignment of paraquat vibrations.

Raman (cm^{-1})	wavenumbers	Assignment
845		C-N stretching
1201		C=C bending
1297		C-C structural distortion
1659		C=N stretching

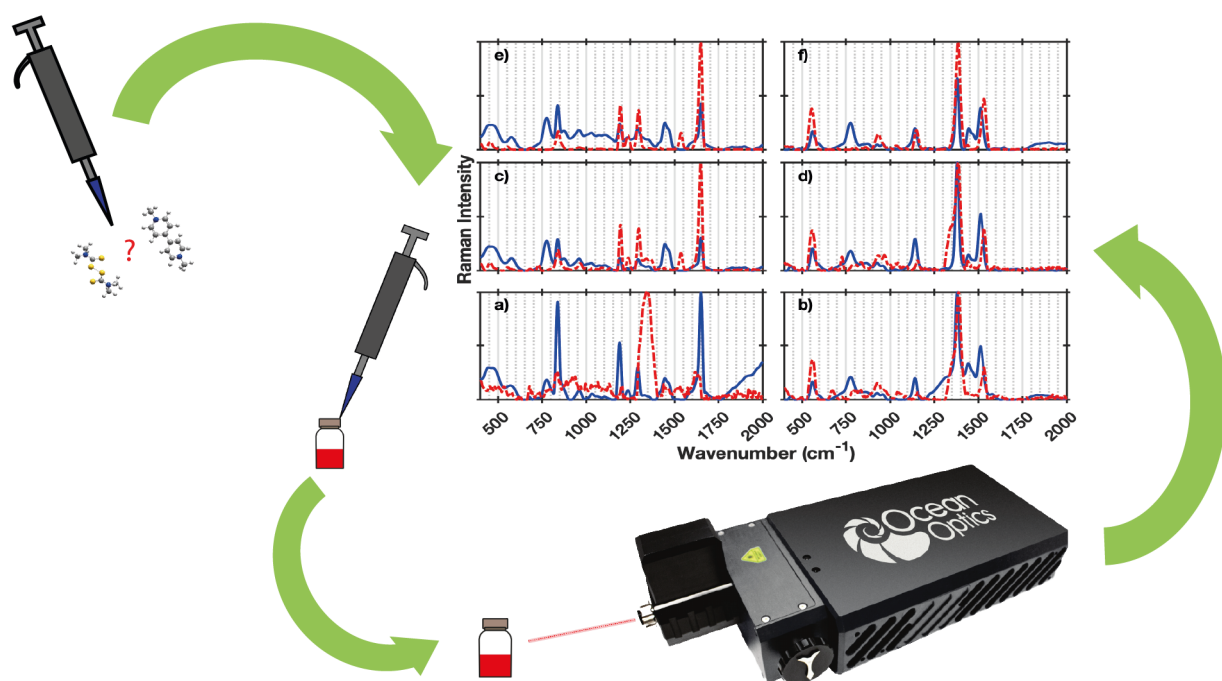
References

1. Kneipp, K. Surface-enhanced Raman scattering. *Physics Today* **60**, 40–46 (2007).
2. Moskovits, M. Surface-enhanced spectroscopy. *Rev. Mod. Phys.* **57**, 783–826 (1985).
3. Pilot, R., Signorini, R., Durante, C., *et al.* A Review on Surface-Enhanced Raman Scattering. *Biosensors* **9** (2019).
4. Yan, Z.-X., Zhang, Y.-L., Wang, W., *et al.* Superhydrophobic SERS Substrates Based on Silver-Coated Reduced Graphene Oxide Gratings Prepared by Two-Beam Laser Interference. *ACS Applied Materials & Interfaces* **7**, 27059–27065 (2015).
5. Yao, C., Gao, X., Liu, X., Shen, Y. & Xie, A. In-situ preparation of Ferrero[®] chocolate-like Cu₂O@Ag microsphere as SERS substrate for detection of thiram. *Journal of Materials Research and Technology* **11**, 857–865 (2021).
6. Ding, Q., Kang, Z., He, X., *et al.* Eggshell membrane-templated gold nanoparticles as a flexible SERS substrate for detection of thiabendazole. *Microchimica Acta* **186**, 453 (2019).
7. Huang, D., Zhao, J., Wang, M. & Zhu, S. Snowflake-like gold nanoparticles as SERS substrates for the sensitive detection of organophosphorus pesticide residues. *Food Control* **108**, 106835 (2020).
8. Zhu, C., Zhao, Q., Meng, G., *et al.* Silver nanoparticle-assembled micro-bowl arrays for sensitive SERS detection of pesticide residue. *Nanotechnology* **31**, 205303 (2020).
9. Gao, M., Lin, X., Li, Z., *et al.* Fabrication of highly sensitive and reproducible 3D surface-enhanced Raman spectroscopy substrates through in situ cleaning and layer-by-layer assembly of Au@Ag nanocube monolayer film. *Nanotechnology* **30**, 345604 (2019).
10. Freudenberg. *Even more sustainable: Evolon[®] made from post-consumer recycled PET - Freudenberg Performance Materials* Accessed: Dec 1 2021.
11. Dias Soares, J. M. & de Oliveira, H. P. Silver-based surface enhanced Raman spectroscopy devices for detection of organophosphorus pesticides traces. *Biotechnology Progress* **35**, e2809 (2019).
12. Yu, W. W. & White, I. M. A simple filter-based approach to surface enhanced Raman spectroscopy for trace chemical detection. *Analyst* **137**, 1168–1173 (2012).
13. Sun, J., Gong, L., Wang, W., *et al.* Surface-enhanced Raman spectroscopy for on-site analysis: A review of recent developments. *Luminescence* **35**, 808–820 (2020).
14. Jiang, J., Zou, S., Ma, L., *et al.* Surface-Enhanced Raman Scattering Detection of Pesticide Residues Using Transparent Adhesive Tapes and Coated Silver Nanorods. *ACS Applied Materials & Interfaces* **10**, 9129–9135 (2018).
15. Zhang, Y., Huang, Y., Zhai, F., *et al.* Analyses of enrofloxacin, furazolidone and malachite green in fish products with surface-enhanced Raman spectroscopy. *Food Chemistry* **135**, 845–850 (2012).
16. Fikiet, M. A., Khandasammy, S. R., Mistek, E., *et al.* Surface enhanced Raman spectroscopy: A review of recent applications in forensic science. *Spectrochimica Acta Part A: Molecular and Biomolecular Spectroscopy* **197**, 255–260 (2018).

17. Liu, Y., Li, X., Cheng, J., *et al.* SERS devices with "hedgehog-like" nanosphere arrays for detection of trace pesticides. *Journal of Innovative Optical Health Sciences* **14**, 2141005 (2021).
18. Yu, H., Lyu, Q., Chen, X., *et al.* Nylon membranes modified by gold nanoparticles as surface-enhanced Raman spectroscopy substrates for several pesticides detection. *RSC Advances* **11**, 24183–24189 (2021).
19. Han, C., Wei, Y., Lei, F., *et al.* Heterostructured CuO@ZnO@Ag biomimetic setaria as wettability-switchable difunctional SERS substrate for trace pesticide and DNA detections. *Nanophotonics* **10**, 2671–2682 (2021).
20. Authority, E. F. S. Evaluation of the data on clothianidin, imidacloprid and thiamethoxam for the updated risk assessment to bees for seed treatments and granules in the EU. *EFSA Supporting Publications* **15**, 1378E (2018).
21. Agency, U. E. P. Guidance for Assessing Pesticide Risks to Bees. *Health Canada Pest Management Regulatory Agency (PMRA), and California Department of Pesticide Regulation* (2014).
22. Chen, J., Huang, M., Kong, L. & Lin, M. Jellylike flexible nanocellulose SERS substrate for rapid in-situ non-invasive pesticide detection in fruits/vegetables. *Carbohydrate Polymers* **205**, 596–600 (2019).
23. Wood, T. J. & Goulson, D. The environmental risks of neonicotinoid pesticides: a review of the evidence post 2013. *Environmental Science and Pollution Research* **24**, 17285–17325 (2017).
24. Tsvetkov, N., Samson-Robert, O., Sood, K., *et al.* Chronic exposure to neonicotinoids reduces honey bee health near corn crops. *Science* **356**, 1395–1397 (2017).
25. Babazadeh, S., Moghaddam, P. A., Keshipour, S. & Mollazade, K. Analysis of imidacloprid and penconazole residues during their pre-harvest intervals in the greenhouse cucumbers by HPLC–DAD. *Journal of the Iranian Chemical Society* **17**, 1439–1446 (2020).
26. Hermsen, A., Lamers, D., Schoettl, J., Mayer, C. & Jaeger, M. In-field detection method for imidacloprid by surface enhanced Raman spectroscopy. *Toxicological & Environmental Chemistry* **104**, 36–54 (2022).
27. Frens, G. Controlled Nucleation for the Regulation of the Particle Size in Monodisperse Gold Suspensions. *Nature Physical Science* **241**, 20–22 (1973).
28. Kimling, J., Maier, M., Okenve, B., *et al.* Turkevich Method for Gold Nanoparticle Synthesis Revisited. *The Journal of Physical Chemistry B* **110**, 15700–15707 (2006).
29. Turkevich, J., Stevenson, P. C. & Hillier, J. A study of the nucleation and growth processes in the synthesis of colloidal gold. *Discussions of the Faraday Society* **11**, 55–75 (1951).
30. Bohren, C. & Huffman, D. *Absorption and Scattering of Light by Small Particles* (Wiley-VCH Verlag GmbH and Co., Weinheim, Germany, 1983).
31. Munro, C. H., Smith, W. E., Garner, M., Clarkson, J. & White, P. C. Characterization of the Surface of a Citrate-Reduced Colloid Optimized for Use as a Substrate for Surface-Enhanced Resonance Raman Scattering. *Langmuir* **11**, 3712–3720 (1995).

32. Tashiro, K., Kouno, N., Wang, H. & Tsuji, H. Crystal Structure of Poly(lactic acid) Stereocomplex: Random Packing Model of PDLA and PLLA Chains As Studied by X-ray Diffraction Analysis. *Macromolecules* **50**, 8048–8065 (2017).
33. Yunker, P. J., Durian, D. J. & Yodh, A. G. Coffee rings and coffee disks: Physics on the edge. *Physics Today* **66**, 60–61 (2013).
34. Joseph, V., Matschulat, A., Polte, J., *et al.* SERS enhancement of gold nanospheres of defined size. *Journal of Raman Spectroscopy* **42**, 1736–1742 (2011).
35. Chen, Q., Hassan, M. M., Xu, J., *et al.* Fast sensing of imidacloprid residue in tea using surface-enhanced Raman scattering by comparative multivariate calibration. *Spectrochimica Acta Part A: Molecular and Biomolecular Spectroscopy* **211**, 86–93 (2019).
36. Dowgiallo, A. M. & Guenther, D. A. Determination of the Limit of Detection of Multiple Pesticides Utilizing Gold Nanoparticles and Surface-Enhanced Raman Spectroscopy. *Journal of Agricultural and Food Chemistry* **67**, 12642–12651 (2019).
37. Tang, J., Chen, W. & Ju, H. Rapid detection of pesticide residues using a silver nanoparticles coated glass bead as nonplanar substrate for SERS sensing. *Sensors and Actuators B: Chemical* **287**, 576–583 (2019).
38. Qiu, H., Guo, J., Wang, M., *et al.* Reduced graphene oxide supporting Ag meso-flowers and phenyl-modified graphitic carbon nitride as self-cleaning flexible SERS membrane for molecular trace-detection. *Colloids and Surfaces A: Physicochemical and Engineering Aspects* **560**, 9–19 (2019).
39. Oliveira, M. J., Quaresma, P., Peixoto de Almeida, M., *et al.* Office paper decorated with silver nanostars - an alternative cost effective platform for trace analyte detection by SERS. *Scientific Reports* **7**, 2480 (2017).
40. De Oliveira, V. E., Castro, H. V., Edwards, H. G. M. & de Oliveira, L. F. C. Carotenes and carotenoids in natural biological samples: a Raman spectroscopic analysis. *Journal of Raman Spectroscopy* **41**, 642–650 (2010).

5 Pesticide Identification Using Surface-Enhanced Raman Spectroscopy and Density Functional Theory Calculations: From Structural Insights to On-Site Detection



Chapter 5 is reproduced from *Andrea Hermsen, Florian Hertel, Dominik Wilbert, Till Gronau, Christian Mayer & Martin Jaeger (2023) Pesticide Identification Using Surface Enhanced Raman Spectroscopy and Density Functional Theory Calculations: From Structural Insights to On-Site Detection, Applied Spectroscopy, DOI: 10.1177/00037028241236501* with permission from Sage.

5.1 Abstract

Pesticides play an important role in conventional agriculture. Yet, their harmful effects on the environment are becoming increasingly apparent. The occurrence of pesticides is hence being monitored worldwide. For fast, easy, yet sensitive identification, surface enhanced Raman spectroscopy (SERS) is a powerful tool. In this study, a method is introduced which may be amended to in-field detection of pesticides. Gold and silver nanoparticles were synthesized, size-tailored and characterized. The herbicide paraquat and the fungicide thiram served as model compounds. The preparation yielded reproducible SERS spectra. Using quantum chemical computation, Raman and SERS spectra were calculated and analyzed. The interpretation of vibrational modes in combination with SERS enhancement and attenuation allowed to identify compound specific bands. The assignment was interpreted in terms of the orientation of paraquat and thiram on the gold and silver nanoparticle surface. Paraquat preferred a co-planar arrangement parallel to the gold nanoparticle surface and a head-on orientation on the silver nanoparticle. For thiram, breaking of the disulfide bond was recognized, such that interaction with the surface occurred via the sulfur atoms. Successful detection of the pesticides after recollection from vegetable leaves demonstrated the method's applicability for pesticide identification.

5.2 Introduction

The use of pesticides is a common tool in worldwide agriculture. The environmentally harmful character of these substances has become more and more apparent. Hence, their monitoring has been required and the number of monitored compounds is ever increasing since.¹ Meanwhile, some of these pesticides are banned by various public authorities or their use is restricted to greenhouses.^{2,3} Pesticide residues of about 0.34 $\mu\text{g/g}$ can be expected after harvest, while the persistency in different vegetables and on-site was reported to last up to at least 60 days.^{4,5} One of the most recent methods for detecting pesticides takes advantage of mobile surface enhanced Raman spectroscopy (SERS) allowing high-throughput and simple protocols.⁵ In principle, pesticides can be detected directly in the field. SERS detection generally requires a Raman spectrometer and a SERS active substrate.⁶ Such substrates often consist of nanoparticles made of silver or gold. Yet, the variety is large. Substrates were made of simple filter paper or textiles, other substrates were produced by more complex, yet more reproducible methods such as laser ablation and gas deposition.^{7,8} The simplest type of SERS active substrate is a nanoparticle suspension to which the dissolved analyte is added.⁹ Comprehensive overviews of substrates used for SERS and numerous resulting spectra have been given.¹⁰⁻¹³ Since SERS spectra vary with substrates and experimental conditions, spectra obtained in different studies or by different groups often show high variability and lack comparability and reproducibility. As to analytes, thiram is one of the most studied pesticides by SERS, while paraquat is investigated less frequently.¹²

To overcome the difficulty that SERS spectra vary with the substrate used, computational chemistry may assist in spectral analysis.¹⁴ Due to technical progresses, computational chemistry is gaining more and more importance also in environmental chemistry, providing methods such as structure-property relation prediction by conductor-like screening model for real solvents, which further improve quantitative structure-activity relationship (QSAR) analysis.^{15,16} In this respect, density functional theory calculations can predict physical properties of environmentally relevant substances, such as polar surface areas, molecular conformations and also vibrational spectra. Most chemical property calculations require the molecular structure as starting point. Since molecules often possess several degrees of freedom, the conformational distribution needs to be examined first. Subsequently, a geometry optimization may follow yielding the geometry corresponding to the lowest energy, from which physical properties are calculated.

In this study, the two pesticides paraquat and thiram were investigated comprehensively. Experimental Raman and SERS spectra were recorded using gold and silver nanoparticles as SERS active substrates. DFT calculations were applied to simulate and analyze the Raman spectra of the two compounds. Thiram and paraquat were applied to plants, recollected and transferred onto substrates to record SERS spectra. Based on DFT calculations, the influence of the cationic character of paraquat and the affinity of the sulfur of thiram to the nanoparticle on the interaction between compound and nanoparticle were investigated.

5.3 Materials & Methods

Paraquat and thiram were purchased from Pestanal[®] Series. Stock solutions were prepared to yield final concentrations of thiram 0.125 mM and paraquat 0.1 mM. All other chemicals were purchased from Sigma Aldrich, Darmstadt, Germany, and used without further purification.

Gold nanospheres were prepared following a synthesis route based on previously established methods.¹⁷⁻¹⁹ Thus, 1.25 mL of hydrotetrachloroauric acid (10 mmol/L) and 450 μ L of 1% trisodium citrate solution were successively added to 50 mL deionized water at 80 °C and stirred at 500 rpm. The solution was kept at 80 °C, with the color changing from yellow to red. After another 5 minutes, it was cooled down to ambient temperature while stirred. The entire synthesis was carried out under a nitrogen atmosphere.

Silver nanospheres were prepared using a modified route of Lee & Meisel.^{20,21} D-mannitol (5 g) was added to 50 mL of deionized water under nitrogen atmosphere, stirred at 800 rpm, and heated to 95 °C. When the temperature was constant at 95 °C, 9 mg of silver nitrate were added. After one minute, 1 mL of a 3% trisodium citrate solution was added. The mixture was stirred for one hour at 95 °C. After one hour, the color changed from yellow to greenish-gray. Nanoparticles were characterized using absorption spectra. The size distribution was determined from transmission electron micrographs. The absorption spectra were recorded in a 10 mm quartz glass suprasil cuvette (Hellmann), using a UV5Nano (Mettler Toledo) with a resolution of 1 nm and a spectral range from 200 nm to 1100 nm. Transmission electron

micrographs were recorded on a carbon lacey copper grid using an H-7100FA (Hitachi). The software IC Measure (version 2.0.0.161, The Imaging Source Europe) was used to determine the size distribution.

Raman and SERS measurements were performed on Raman readers (Ocean Insight) equipped with lasers of 532 nm and 785 nm excitation wavelength providing 45 mW and 70 mW, respectively. For SERS measurements in solution, samples were transferred into 2 mL vials (Glass Vials). Subsequently, 1 mL of the nanoparticle solutions, gold or silver, 0.5 mL deionized water, 100 μ L of the thiram or paraquat solution, and 100 μ L 1 M hydrochloric acid were added into the vial.

As model samples, lettuce leaves, zucchini and sugar peas were used. The plants were grown on a bioorganic field under bioorganic conditions, i.e. no pesticides were applied during or prior to growth. The soil and the seeds corresponded to the current organic quality requirements of the EU directives. Firstly, the vegetables were harvested, stored separately and brought to the laboratory. They were rinsed with deionized water. After this cleaning step, 15 μ L of pesticide stock solution were applied by dropwise pipetting onto the lettuce leaves, the zucchini and sugar peas. A scheme of the sample preparation is given in Figure 5.11. The expected amount of pesticide on the vegetable was 0.45 μ g for thiram and 0.39 μ g for paraquat. After allowing the solvent to evaporate, the pesticide remaining on the vegetable was re-uptaken. Firstly, 15 μ L of deionized water was pipetted onto the pesticide residential spot.²² Secondly, the solution was collected using a pipette and transferred into a 2 mL quartz vial. Nanoparticle solution, deionized water and hydrochloric acid were added to the sample and mixed by vigorously shaking as described above.

Sixteen spectra were accumulated and averaged using Ocean View software (Ocean Insight). Spectra were smoothed through a Savitzky-Golay filter over 11 points and a polynomial of grade 3 in MATLAB v.R2019b, update 3, (The MathWorks Inc.).²³ Baseline correction was performed within MATLAB using the algorithm of Schulze et al. for Raman baseline correction.²⁴ As the SERS enhancement was strong enough, no background subtraction was required. Also further processing was unnecessary.

The computations for conformational searching were performed using the xTB software package including the CREST package from the Grimme group.^{16,25-27} Energy windows for cut-off values were default settings with 6 kcal/mol and 12 kcal/mol. The conformers obtained from xTB/CREST optimization were ranked with respect to their energy. Conformers above a threshold of one percent were subjected to further quantum chemical computations using Gaussian 16 software package.²⁸ To the remaining conformers Boltzmann averaging was performed. For preoptimization, the density functional theory B3LYP and basis-set 6-21G were used to exclude the conformers below 1%.²⁹⁻³¹ The hybrid functional PW6B95D3 and basis-set aug-cc-pVTZ with a (99,590) Lebedev grid for final optimization and frequency calculations were applied.^{32,33} The convergence thresholds were chosen as follows: maximum force per atom smaller than 4.5×10^{-1} Ha \AA^{-1} , RMS force per atom smaller than 3.0×10^{-4} Ha \AA^{-1} maximum atomic displacement smaller than 18.0×10^{-4} \AA , and RMS displacement smaller than 12×10^{-4} \AA . During frequency calculation, no imaginary frequencies

were obtained. A Lorentz broadening of 4 cm^{-1} half-width at full-maximum was applied to the calculated modes. To take all conformers above 1% into account, Boltzmann-weighted averaging was performed to calculate the total spectrum from the individual conformer spectra. Simulated spectra were scaled with a factor of 0.97.³⁴ For the assignment of the vibrational modes, VEDA software package was used.³⁵

5.4 Results & Discussion

At the beginning of the study, gold and silver nanoparticles were successfully prepared. The synthesis yielded spherical gold nanoparticles, cf. Fig. 5.1a. A size of 40 nm was obtained after synthesis and successive purification of the nanoparticle solutions through centrifugation. The size distribution, cf. Fig. 5.1b, had an average diameter of 39.6 nm with a polydispersity of ± 5.5 nm. The spherical character of the gold nanoparticles in combination with the size of about 40 nm led to a plasmon band in the range of 530 nm, cf. Fig. 5.1c). Agglomeration by hydrochloric acid caused a second plasmon band whose maximum occurred at 780 nm, cf. Fig. 5.1c), allowing SERS experiments to be performed at a laser wavelength of 785 nm. This finding was consistent with previous studies.⁵ While aggregation might be caused by the analytes, in particular the cationic paraquat, only minor signal enhancement was observed, which was interpreted in terms of absence of favorable agglomeration as was the case with hydrochloric acid. In a previous investigation, agglomeration by salt and acid was investigated.⁵ The signal enhancement was reported less strong for salt induced agglomeration than when using acids. Yet, the resonance frequencies appeared identical in both cases.

The silver nanoparticle synthesis of Lee & Meisel, that was modified in using D-mannitol, yielded spherical nanoparticles similar to the gold nanoparticle, cf. Fig. 5.1d).^{20,21} The resulting silver nanoparticles had a mean diameter of 49 nm, cf. Fig. 5.1e) and a polydispersity of ± 3 nm. The diameter was hence larger than the one of silver nanoparticles commonly used for SERS. The extended size can be explained as due to the use of a weak reducing agent such as D-mannitol.²¹ In absorption spectra, the synthesized silver nanoparticles showed a maximum of 412 nm after synthesis and one of 550 nm after agglomeration by hydrochloric acid, cf. Fig 5.1f). The size and hence the absorption maximum rendered them suitable for SERS experiments using a laser wavelength of 532 nm. Subsequently, SERS experiments were conducted for the detection of paraquat and thiram, whose formulae, geometry optimized structures, and electronic potential surfaces are represented in Fig. 5.2.

The geometry optimized structures were eventually used to calculate the Raman spectra to infer the possible vibrations and the corresponding vibrations in the SERS spectra. Firstly, a conformer search for paraquat yielded three conformers that transitioned into one after optimization. The three initial structures were also found by Ferreira to have the same energy barriers related to the rotation about the bond connecting the two rings.³⁶ The final stable structure had a dihedral angle C4-C5-C10-C11 of 36.77° , the angles C4-C5-C11 and C5-C10-C11 were 121.04° and 121.05° , respectively. The dihedral angle between the two ring

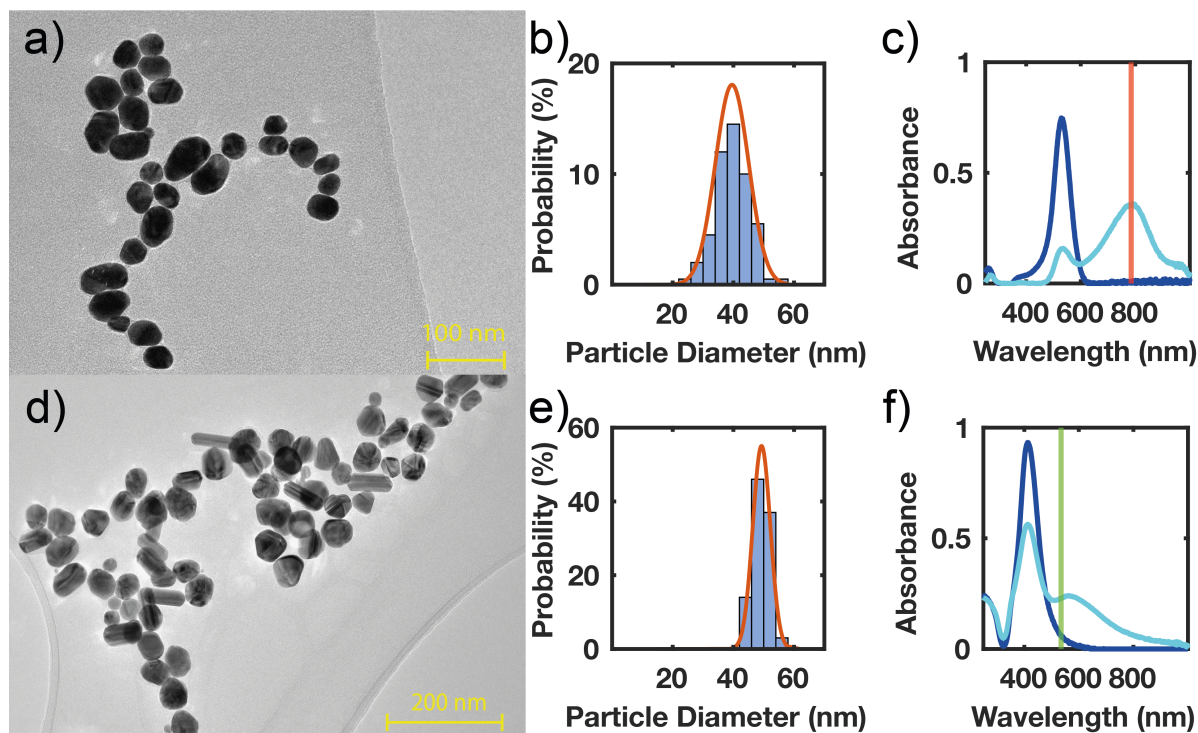


Figure 5.1 – Synthesized gold (top) and silver (bottom) nanoparticles: TEM images a) and d), size distribution b) and e), and absorption spectra, c) and f), of nanoparticles (dark blue line), nanoparticles agglomerated through hydrochloric acid addition (light blue line), and Raman excitation wavelengths at 785 nm (red line) and 532 nm (green line).

systems was 40° for the energy-minimized structure. This conformer structure results from a compromise between the sterically favorable geometry due to repulsive forces of the ortho-hydrogens and the electronically favorable π -conjugation. Thus, the angle of 40° reflects the optimum between steric hindrance and conjugation.³⁷ For thiram, no conformer search has been conducted in prior studies. Our search resulted in twelve conformers, four structures of which were found stable, cf. Table 5.1. The four conformers were further optimized with the high set PW6B95D3/aug-cc-pVTZ. Inspection of the electrostatic potential (ESP) of both molecules, cf. Figure 5.2, allowed to hypothesize on the pesticide-nanoparticle interaction. Paraquat possesses the most electronegative potential at the methyl groups C1 and C18, while the positive charges are distributed over the ring systems.³⁸ The electronegative potential of thiram was found at the sulfur atoms S4 and S8. The optimized structure showed that the negative potentials resided on the same site of the molecule. As a consequence, paraquat molecules may hence be assumed to adhere to the nanoparticle surface through the methyl groups, while thiram molecules are associated preferentially via the sulfur atoms due to their high negative potential.

Based on the optimized molecular structures, Raman spectra were computed. The spectra for paraquat are displayed in Fig. 5.3 and the corresponding modes are sketched in Fig. 5.4. The first band for paraquat at 640 cm^{-1} is caused by mode (1) which is a ring deformation oscillation. Bending of the atom groups C3-C4-C5, N2-C7-C6, C14-C12-C11 occurred. This band was observed both in the experimentally recorded and the simulated Raman spectrum.

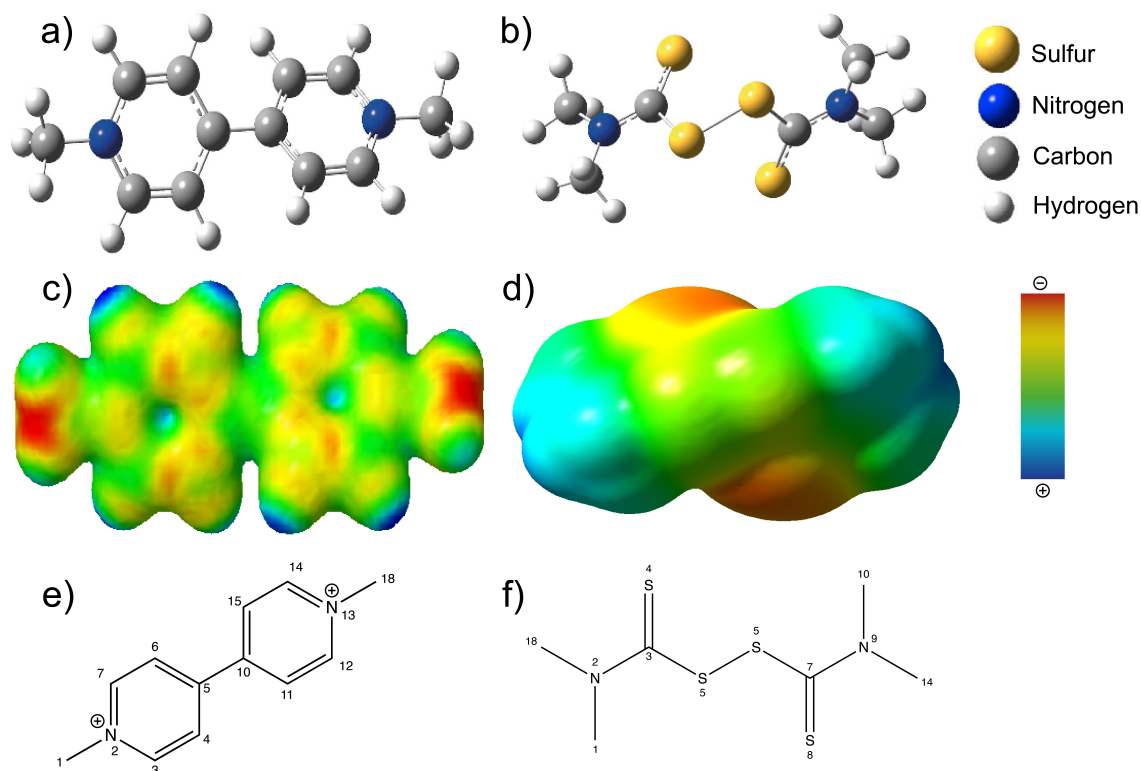


Figure 5.2 – Optimized structural geometries of paraquat (a), and thiram (b), their ESP mapping surface (c) and (d), and the chemical drawings with numbering e) and f), respectively.

A peak at 640 cm^{-1} was also detected in the gold nanoparticle SERS spectrum, albeit attenuated in intensity, but was not observed in the silver nanoparticle SERS spectrum. This was seen indicative of a different mode of association and hence interaction between paraquat and the nanoparticles.

The second band at 832 cm^{-1} was caused by mode (2). This mode is a ring breathing oscillation which is composed of stretching, bending, and torsion oscillations, cf. Table 5.2. This band was found in the experimental and simulated Raman spectra as well as in the SERS spectra. Yet, surprisingly this band grew to the most intense one in the silver nanoparticle SERS spectrum. In other words, this band was most enhanced by silver nanoparticles. It may be assumed that coordinative binding between the paraquat molecule and the silver nanoparticle was the reason. Such binding should result in a change in polarizability, thus increasing the transition probability of the corresponding vibration, which is a consequence of the intensity of the vibrational band. Since the number of particles in the gold and silver colloidal solutions were different and different pesticide molecule-to-particle ratios occurred, different loadings and surface arrangements may result. In case of the silver particles, paraquat may be oriented more upright, maybe even head-on to the nanoparticle. In case of the gold nanoparticles, the paraquat molecule may be arranged more parallel or co-planar on the nanoparticle. The angle between the molecule and the nanoparticle would depend on the number of binding sites on the nanoparticle and the surface loading. A further influence

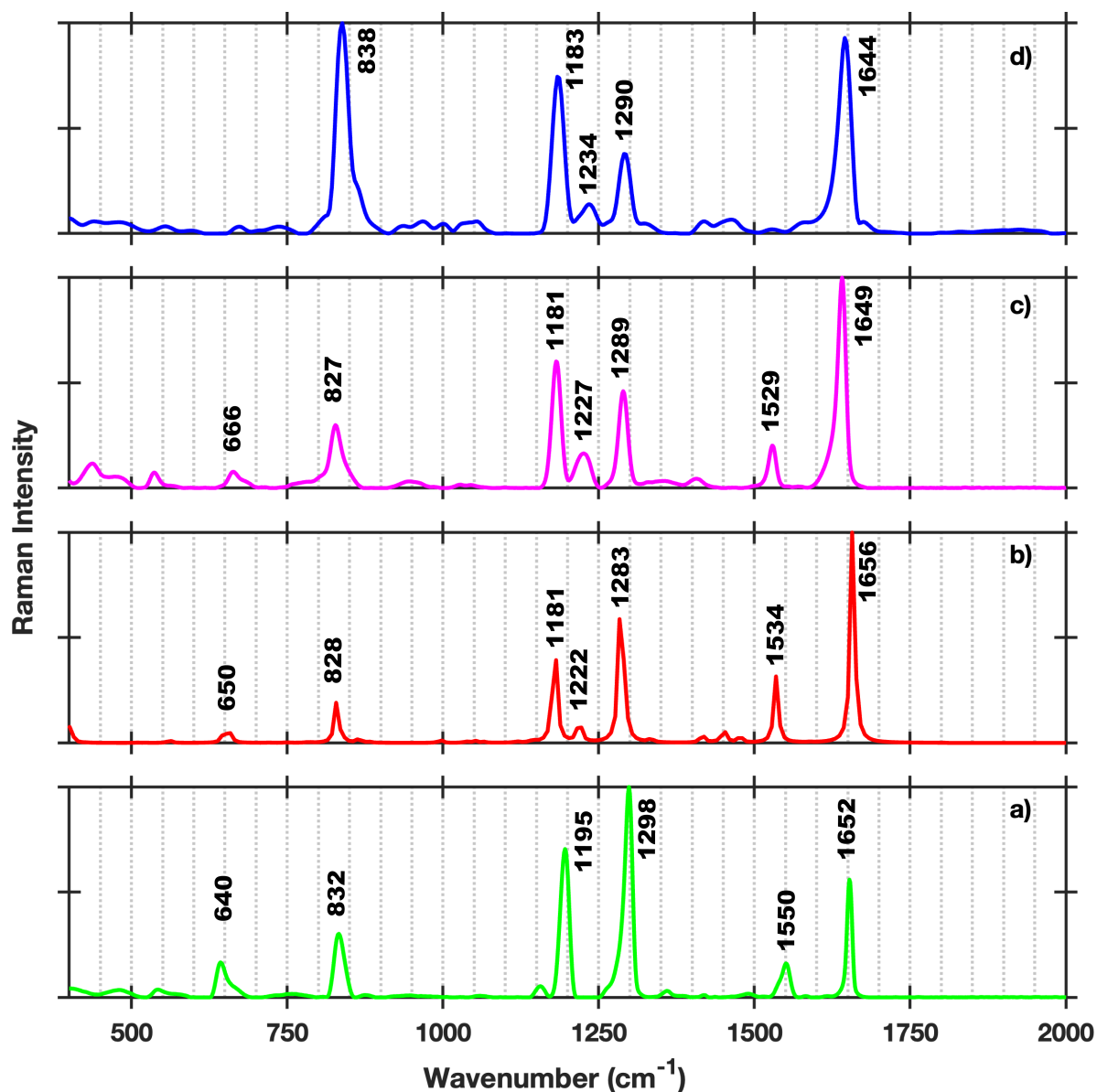


Figure 5.3 – Paraquat: Raman spectra a) experimental, b) simulated, and SERS spectra from c) gold nanoparticles, d) silver nanoparticles.

on the orientation and interaction might arise from the crystal structure of the nanoparticles, leading to band enhancement as well.^{39,40} The vibration at 1195 cm^{-1} was observed in the experimental, the computed and the SERS spectra with similar intensity. Its mode (3) consisted of stretching and bending vibrations. The C-N bonds exercised stretching, while the C atoms within the ring system bending. A band that was expected from the computations could not be detected by conventional Raman spectroscopy. The simulation showed that the band at 1222 cm^{-1} was mode (4), consisting of stretching vibrations of the ring system, where the C-C bonds around the ring were stretched. Yet, this band was detected in gold and silver particles induced SERS spectra with the same intensity. Admittedly, the conventional Raman spectra were only obtained from solids due to the poor solubility in aqueous liquids. It might therefore be possible that this vibration could only be observed in solution. This

hypothesis is supported by the fact that in the solution spectra of Leo et al. the peak at 1222 cm^{-1} is also detected for paraquat in SERS spectra, but just as weak as in the solid spectrum of paraquat.³³ Looking at mode (4), it can also be concluded that the H atoms on the ring system cannot vibrate as strongly as in a solution in the solid crystal packing. Looking at the displacement vector of the vibration resulting in the stretching of the C-C bond, this can be much more limited, which would result in a reduction of the already weak intensity.

The fifth peak in the spectra was observed at 1298 cm^{-1} , caused by a stretching of the ring system as shown by mode (5). Predominantly the bonds C3-C4, C6-C7, C11-C12, and C14-C15 were stretched by the deflection of the H atoms on the ring. The bond C5-C10 between the two ring systems was also stretched, yet to a much lesser extent. The band at 1298 cm^{-1} was the most intense band in the experimental Raman spectrum. It experienced a minor enhancement in the SERS experiments with gold and silver nanoparticles.

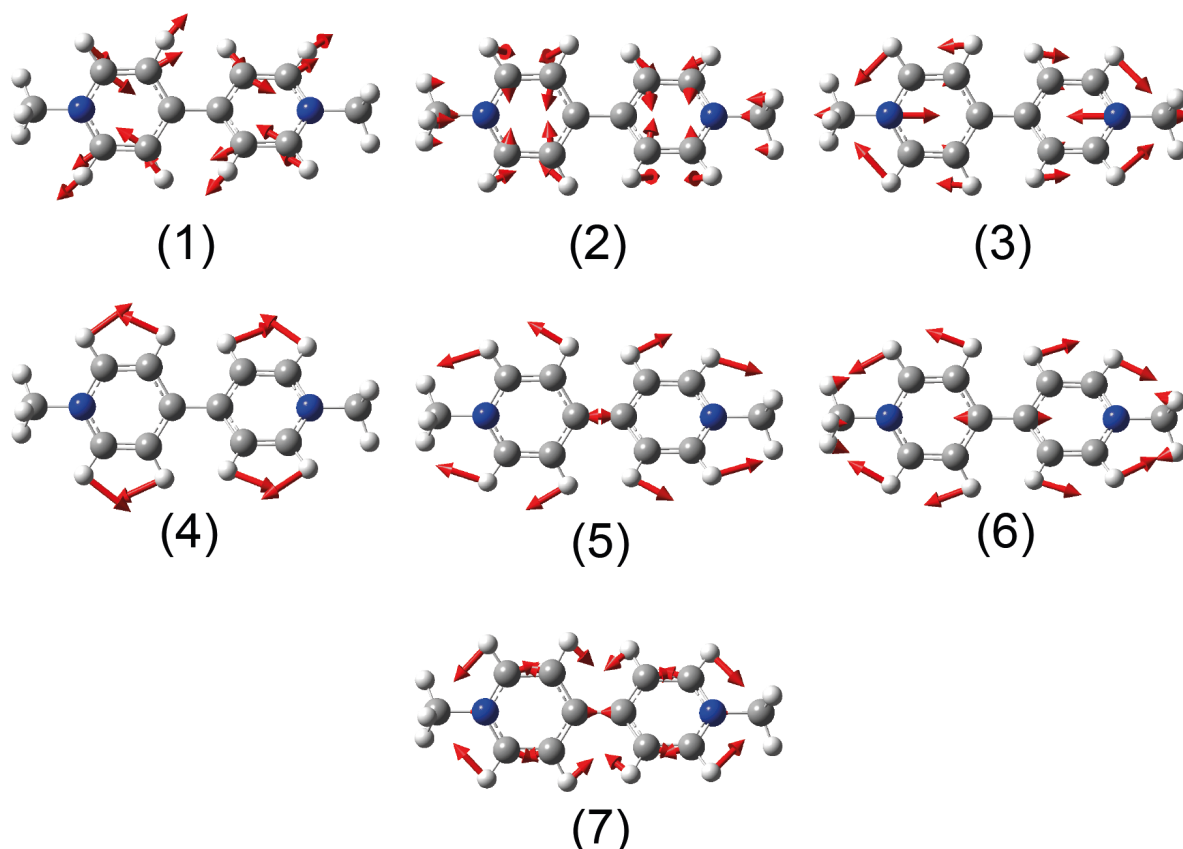


Figure 5.4 – Vibrational modes for paraquat. Mode (1) at 650 cm^{-1} ; (2) at 828 cm^{-1} ; (3) at 1181 cm^{-1} ; (4) at 1222 cm^{-1} ; (5) at 1283 cm^{-1} ; (6) at 1534 cm^{-1} ; and mode (7) at 1656 cm^{-1} with the displacement vectors (red).

The following peak at 1550 cm^{-1} showed a relatively weak intensity caused by the vibrational mode (6). This is a strong stretching vibration of the atoms C5 and C10, pulling the bond between the two ring systems apart. A deflection of the ring systems results, which leads to bending of the two methyl groups at C1 and C18. The highest energy band in the

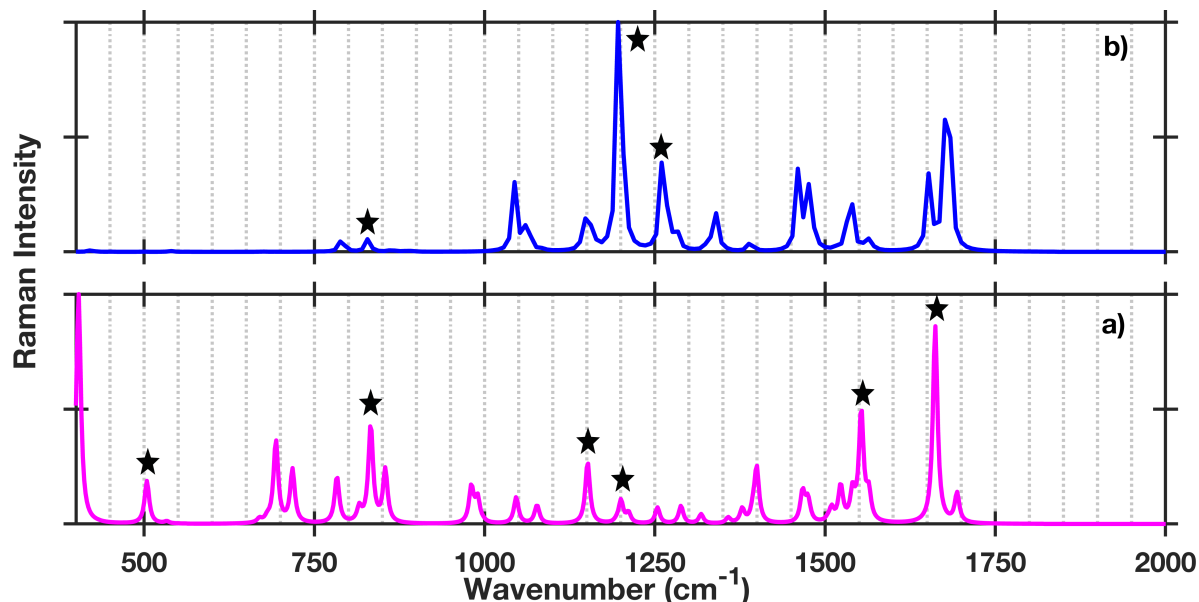


Figure 5.5 – Simulated SERS spectra: Paraquat orientation to gold atoms a) head-on via methylene group, b) parallel. Stars (*) indicate bands occurring in SERS spectra, cf. Figure 5.3. Spectral simulation was achieved using the procedure described in Materials & Methods. Twenty gold atoms were additionally included using the LanL2DZ basis set.

paraquat spectrum was observed at 1652 cm^{-1} , which had significantly higher intensity in the simulated and the SERS spectra than in the experimental Raman spectrum. As the computation showed, mode (7) consisted only of stretching oscillations. As expected for this wavenumber range, the C-N bond was strongly deflected by the vibration of the neighboring H atoms. A strong deflection also occurred at the C=C bonds in the ring system. These modes, with the exception of mode (1), were also calculated by Kreisig et al.³⁸ They reported additional modes at 1361 cm^{-1} and 1492 cm^{-1} . While these modes appeared in the simulated spectrum of our study, they were associated with minimal Raman activity. The calculated activity was most likely related to the functional used for the calculation, i.e. the hybrid-functional PW6B95D3. As it is often recommended for thermochemistry and thermochemical kinetics, it proved also suitable for this study.⁴¹ In contrast, Kreisig et al. used a Hartree-Fock based method. Nevertheless, the SERS signals detected in that study are in agreement with those reported in Table 5.1 of this work.

A parallel arrangement is more likely for paraquat on gold nanoparticles as it may bind to two gold atoms. This would lead to a damping of the vibration at 1652 cm^{-1} and a reduction of the C-C valence oscillation. The binding to the gold atoms is mediated by the charges of paraquat. Preliminary results from spectral simulation, cf. Figure 5.5, indicated that the spectrum corresponding to a parallel or co-planar arrangement most closely resembled the spectrum of the simulation of paraquat in the gas phase. Hence, coordinative binding would seem unlikely. In addition, the charge was delocalized over the entire ring system, which would not account for a single point attraction. Spectra resulting from silver nanoparticle enhancement showed uneven amplification, indicating asymmetry. Examples are the bands at 832 cm^{-1} and 1298 cm^{-1} . While the latter was decreased, the previous was amplified.

The computation of SERS spectra resulting from paraquat on gold and silver nanoparticles is currently being studied and will be published elsewhere. In the SERS experiments with paraquat in solution, the band at 640 cm^{-1} was detected when using gold nanoparticles but was not observed when using silver nanoparticles. The latter amplified the band at 832 cm^{-1} much more intensively due to the crystal structure of the particles. The band at 1652 cm^{-1} experienced one of the strongest amplifications in both SERS experiments.

All mode oscillations from Figure 5.4 are summarized in Table 5.2. Lin et al. detected paraquat using gold nanostars in green tea, using vibrational assignments by Tsen et al.^{42,43} Tsen et al. assigned the vibrations themselves in the course of the detection of paraquat by SERS in adzuki beans.⁴³ Tsen et al. concluded that the band at 846 cm^{-1} is caused by C-N stretching, the band at 1197 cm^{-1} by C=C bending vibrations, the band at 1293 cm^{-1} by structural distortion, and the band at 1648 cm^{-1} by C=N stretching. It should be noted that Lin et al. work with gold particles and Tsen et al. with silver particles. However, the SERS spectra obtained from both groups have the same intensity distribution, unlike our study, where the SERS spectrum differs from the gold and silver experiments. From the work of Kreisig et al., who conducted SERS experiments and DFT calculations of paraquat, it could be seen that at a charge of -0.2 V of the surface the intensity of the peaks changed significantly with respect to each other.³⁸ Thus, the SERS spectra of Botta et al. showed a considerably higher agreement with the intensity patterns of our SERS spectra obtained by means of silver nanoparticles. Yet, they utilized gold nanoparticle substrates.⁴⁴ Thus, it could be assumed that the charge of the SERS substrate and the metal significantly influence SERS spectra. Both have a considerable effect on the geometry arrangement of the molecules on the surface. For thiram, 8 characteristic modes were identified, cf. Fig. 5.6. The first band laid at 426 cm^{-1} , which was observed for thiram in the experimental Raman, the simulated and the SERS spectra. The next band was found at 545 cm^{-1} and was the most intense one in the experimental and simulated Raman spectra. In contrast, the band displayed reduced relative intensity in the two SERS spectra. Subsequently, a very weak band at 841 cm^{-1} was found in the experimental Raman spectrum and could also be seen in similar intensity in the other spectra.

The next band of interest 1141 cm^{-1} was rather weak in both experimental and simulated Raman spectra but was enhanced in the SERS spectra. Further clear differences appeared in the pattern of the higher wavenumber region. The band at 1369 cm^{-1} was detected only with weak to medium intensity in the experimental Raman spectrum, but with very strong intensity in the SERS experiments. In the simulation, this band proved very weak. The next band at 1392 cm^{-1} was again observed having similar intensity in all four spectra. The highest energy band in the thiram spectra was observed at 1455 cm^{-1} and had a rather large peakwidth with weak intensity in the experimental and simulated Raman spectra. However, it appeared with much higher intensity in the SERS spectra. An overview of the bands and their intensities is given in Table 5.3. It should be noted that silver nanoparticles amplified the band at 1455 cm^{-1} much more than gold nanoparticles. Otherwise, the SERS spectra induced by gold and silver nanoparticles did not differ in the case of thiram. The pattern of

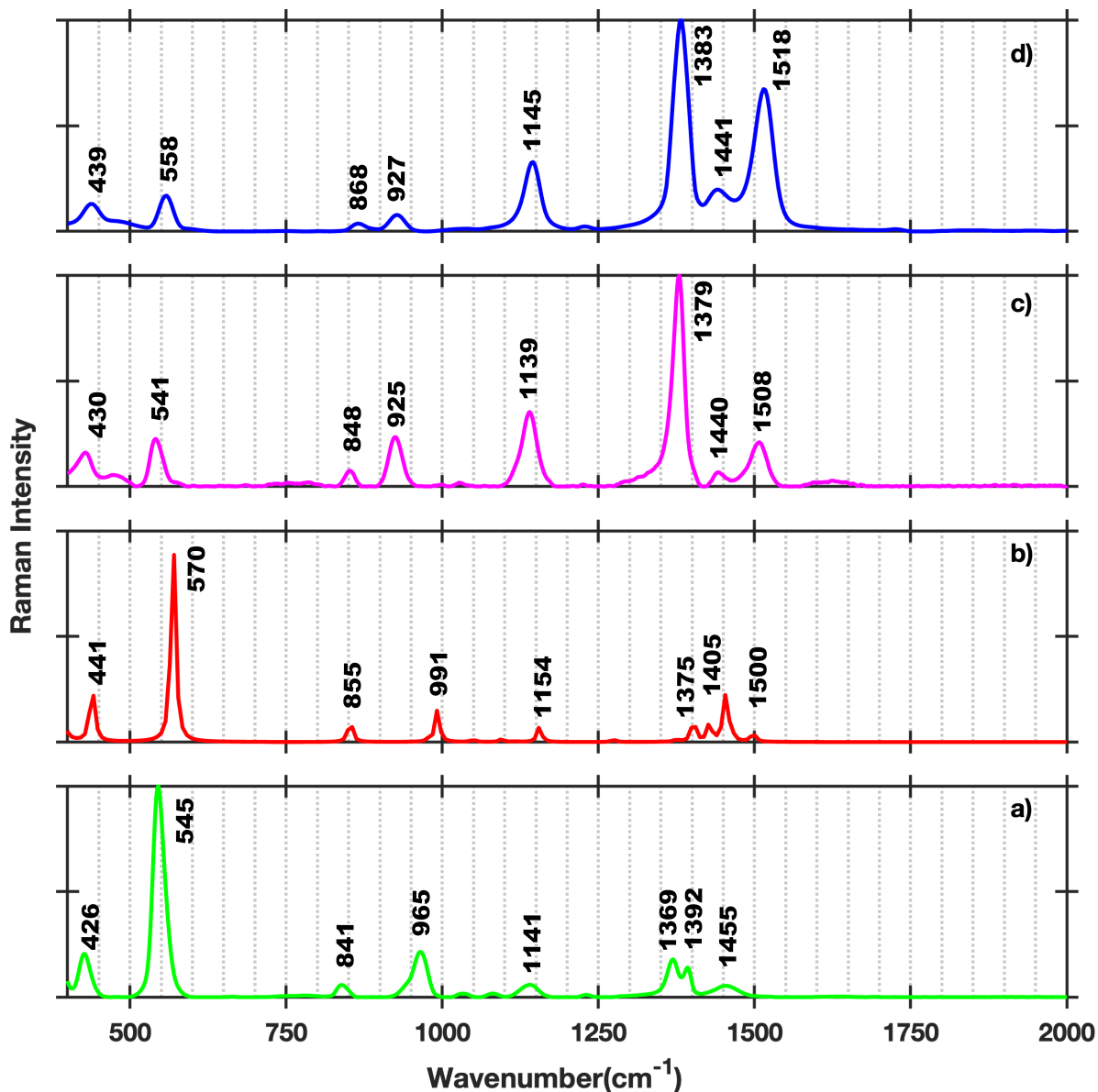


Figure 5.6 – Thiram: Raman spectra a) experimental, b) simulated, and SERS spectra from c) gold nanoparticles, d) silver nanoparticles.

the Raman spectrum of thiram indicates that the disulfide bridge is cleaved upon contact of the thiram molecule and the gold nanoparticle. This is also shown in a study by Kang et al.⁴⁵

As the vegetables were planted and raised under bioorganic approved conditions, prior contamination with pesticides could be excluded. The use of organic seeds also implied the absence of residues from pesticide bleaching. Lettuce leaves, zucchini and sugar snap peas were used as model vegetables. Paraquat and thiram could be detected on vegetables after application as solution, solvent evaporation and recovery using SERS in combination with agglomerated both gold or silver nanoparticle solution, cf. Fig. 5.8.

Hence, the identification of the two pesticides applied on vegetables was possible using the described method, since the recorded SERS spectra showed good agreement with the ones from stock solutions. Only the spectrum of paraquat on sugar peas using gold nanoparticles

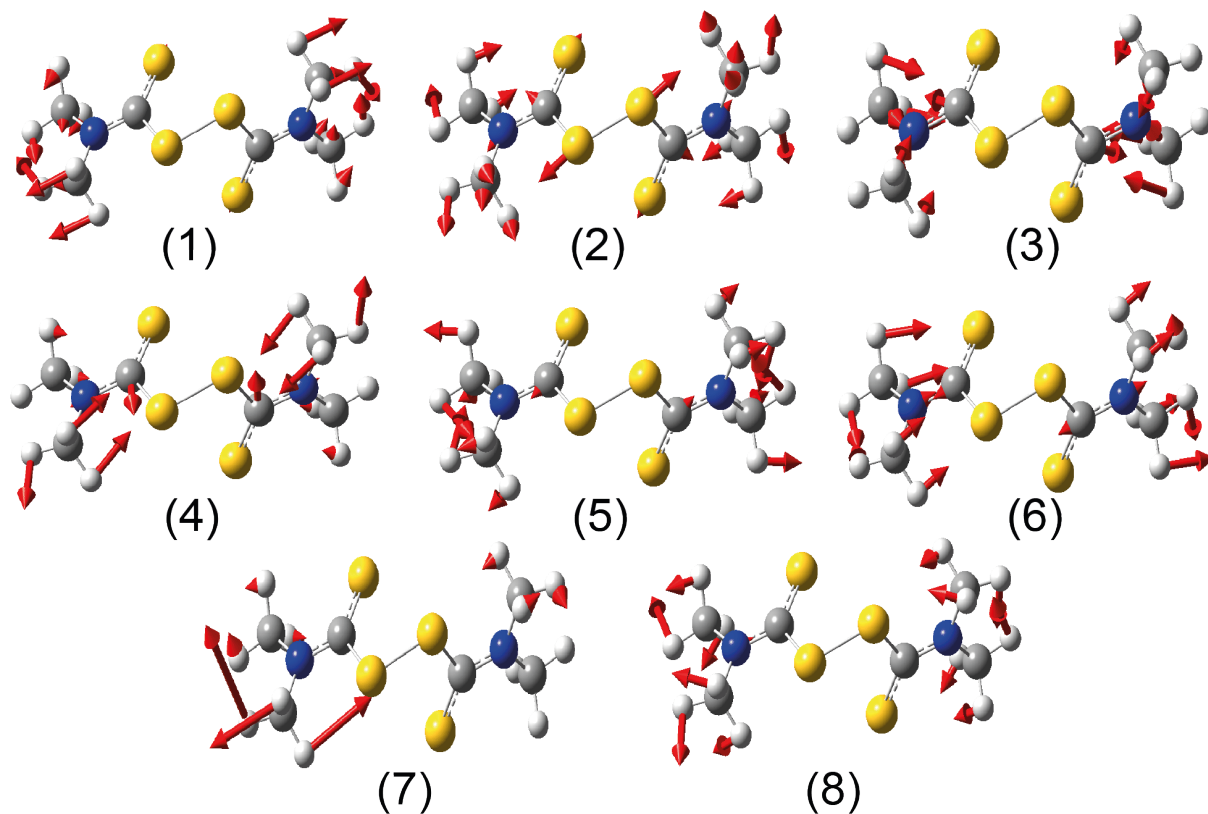


Figure 5.7 – Vibrational modes for thiram: (1) at 426 cm^{-1} ; (2) at 545 cm^{-1} ; (3) at 841 cm^{-1} ; (4) at 965 cm^{-1} ; (5) at 1141 cm^{-1} ; (6) at 1369 cm^{-1} ; (7) at 1392 cm^{-1} ; (8) at 1455 cm^{-1} . Displacement vectors are indicated in red.

showed deviations from the series of paraquat spectra. Insufficient recovery of the pesticide was assumed, although repetition yielded the same negative result. Thus, the presented method may be amenable to fieldable environmental analysis when a handheld or portable Raman spectrometer is used. Using computational chemistry to elucidate SERS spectra helps to identify spectral signals and to correlate bands which undergo frequency shifting in SERS spectra as compared to conventional Raman spectra. In this respect, it also permits to explain on a molecular level potential difference in SERS spectra resulting from using different metals for the nanoparticle substrates as was demonstrated for paraquat.

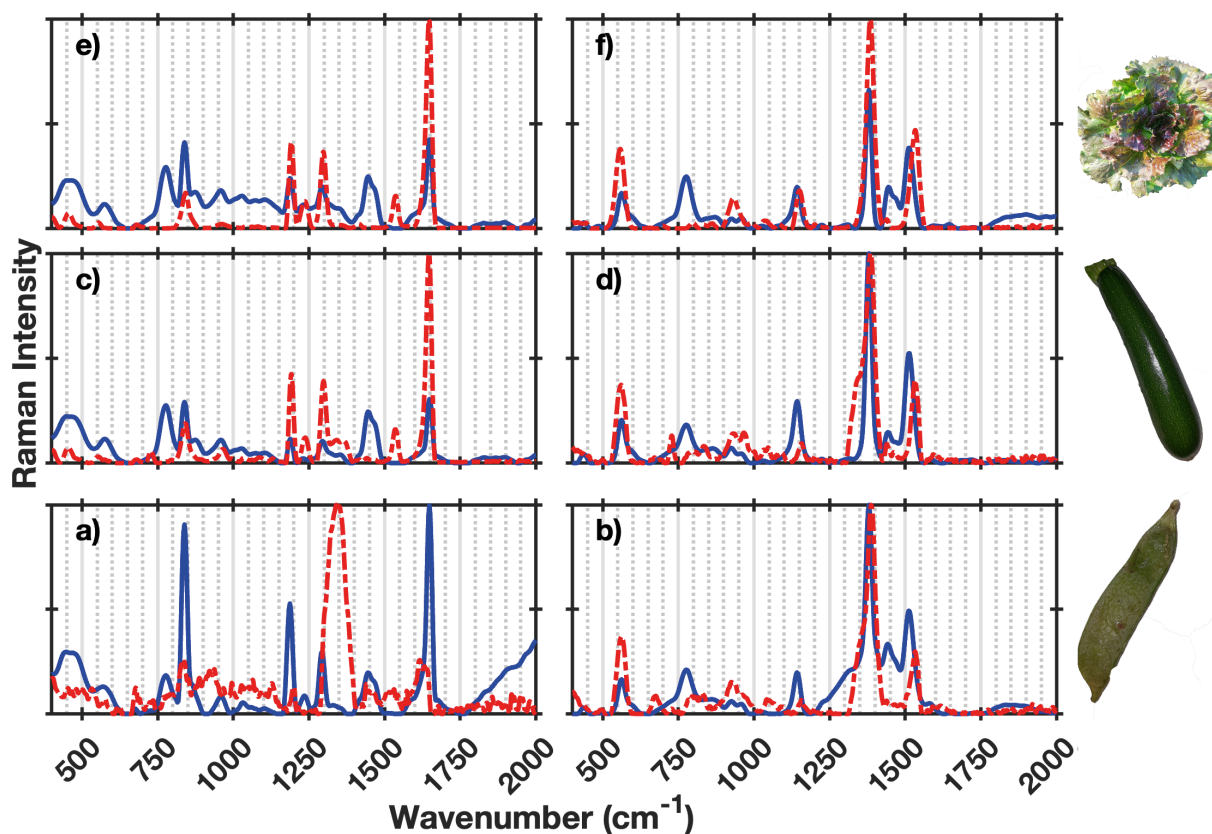


Figure 5.8 – Experimental SERS spectra of paraquat (left) and thiram (right) recollected from sweet pea, a) and b), from zucchini, c) and d), and from lettuce leaves, d) and f), with silver nanoparticles (blue) and gold nanoparticles (red).

5.5 Conclusion

Gold and silver nanoparticles were successfully prepared and used for SERS identification of the pesticides paraquat and thiram. Gold nanoparticles were tailored for a laser wavelength of 785 nm, whereas silver nanoparticles were tuned to 532 nm excitation. Differences were observed in the SERS spectra of each pesticide depending on the nanoparticle metal. This was traced back to the metals inducing different interactions with the pesticides. Careful analysis of enhanced and diminished bands allowed structural interpretation of the pesticide-nanoparticle surface association. Paraquat was assumed to be oriented co-planar onto the gold and head-on on the silver nanoparticle surface. Thiram was interpreted as interacting via the sulfur atoms both to the gold and silver particle surface after disulfide bond cleavage. The spectra could be computed using quantum chemical calculations and good agreement was obtained. The simulated spectra helped simplify the interpretation of the vibrations and thus recognizing specific bands for identification. When using a fieldable Raman spectrometer, the identification of paraquat and thiram applied onto vegetables proved feasible. The method has potential to be amended for fast and easy in-field identification of pesticides.

5.6 Supplemental Information

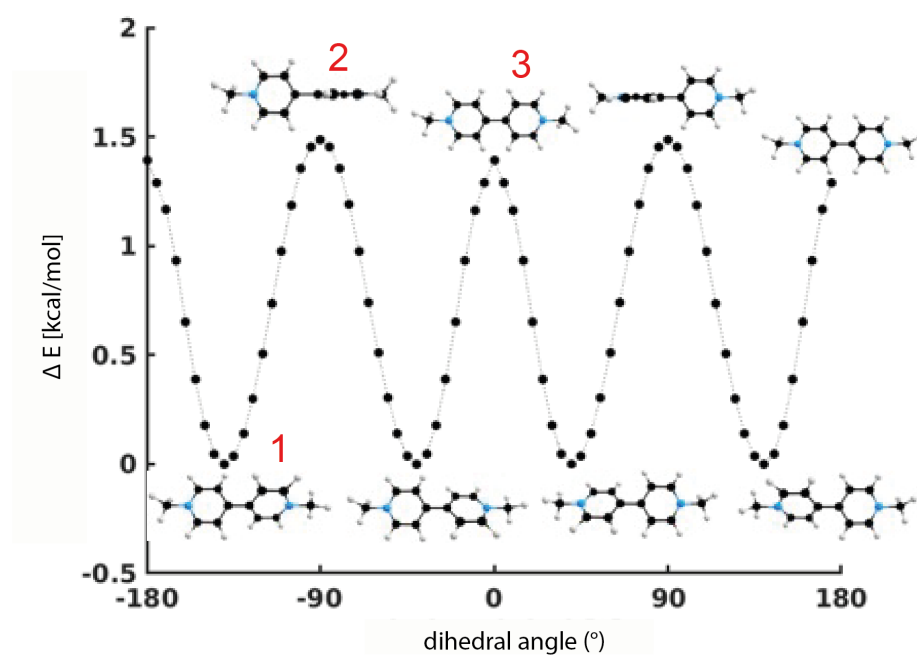
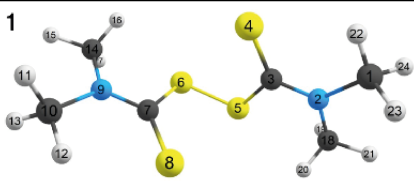
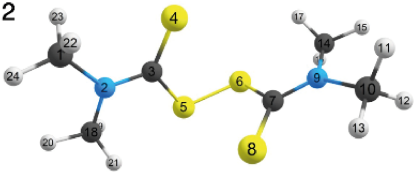
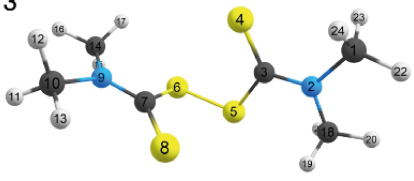
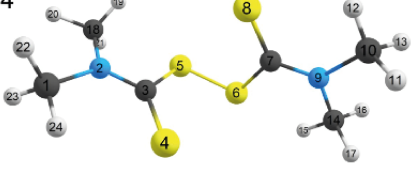
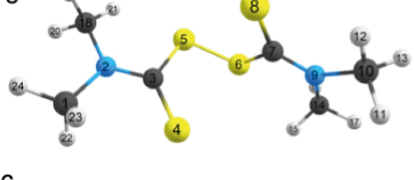
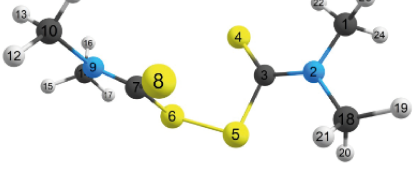
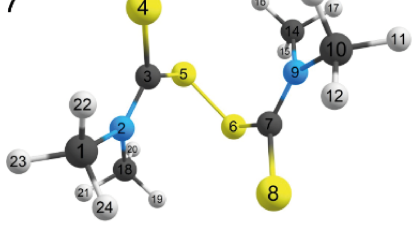


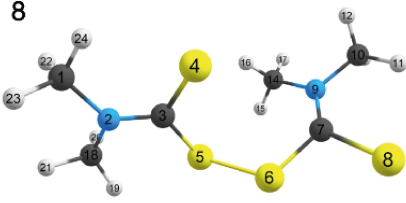
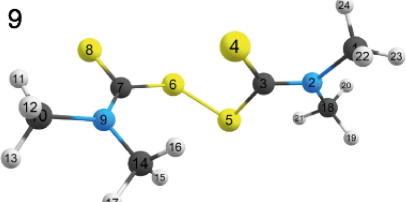
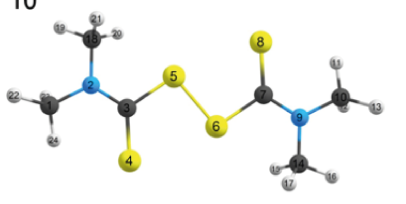
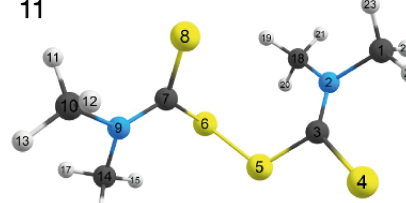
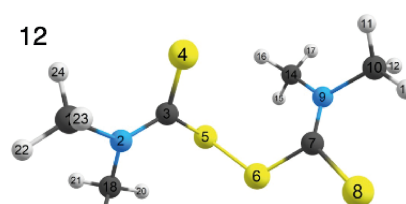
Figure 5.9 - Dihedral scan of paraquat

Table 5.1 – Conformers of thiram and their respective energy difference to the conformer with the lowest energy and the quota.

Conformer	ΔE /kJ/mol	quota
	0.0000	16.27%
	0.4230	13.68%
	0.4390	13.59%
	0.5110	13.19%
	0.6040	12.70%
	0.6100	12.67%
	2.9340	4.88%

...

Table 5.1 – Conformers of thiram and their respective energy difference to the conformer with the lowest energy and the quota. (*continuation*)

Conformer	ΔE /kJ/mol	quota
8 	3.9920	3.16%
9 	4.2150	2.89%
10 	4.4700	2.60%
11 	4.8740	2.20%
12 	4.8850	2.19%

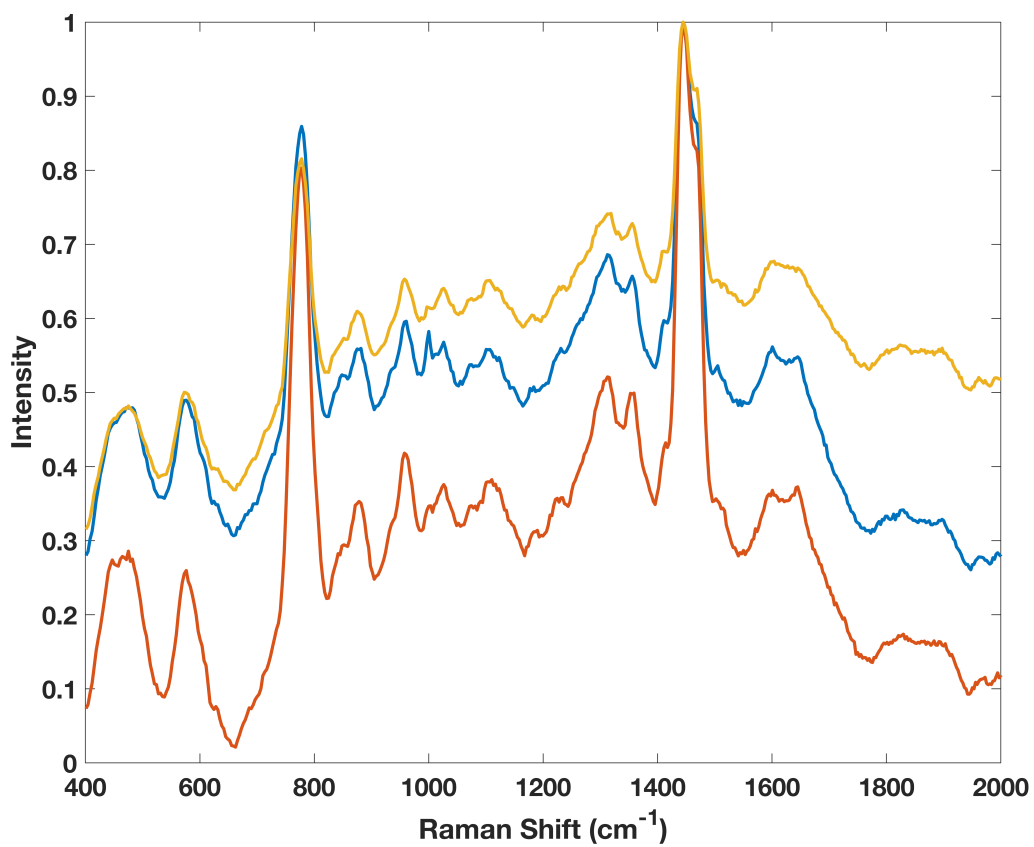


Figure 5.10 – Background spectra of sweet pea (red), zucchini (blue), and lettuce leaves (yellow) for SERS-Experiments.

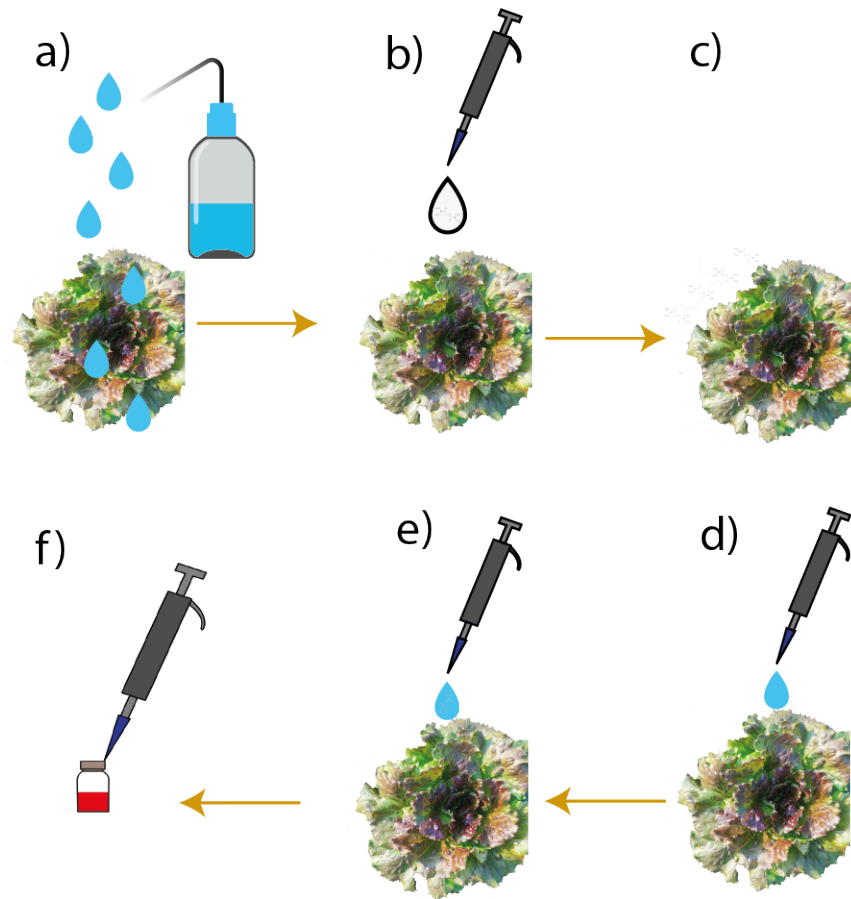


Figure 5.11 – Scheme of the sample preparation.

Table 5.2 – Vibrations of paraquat: Values from experimental (exp.), simulated (sim.) Raman spectra and from SERS spectra induced by gold and silver nanoparticles. v = very, w = weak, m = middle, s = strong, asym. = asymmetric, ν = stretching, β = bending τ = torsion.

Mode	Raman exp.	Raman sim.	SERS gold	SERS silver	Assignment
1	640 (w)	650 (vw)	666 (vw)	–	β C3-C4-C5; β N2-C7-C6; β C10-C15-C14; β N13-C12-C11
2	832 (m)	828 (m)	827 (m)	838 (vs)	ν C1-N2; ν C18-N13; β C3-N2-C7; β C4-C5-C6; β C11-C10-C5; β C12-N13-C4; τ H25-C3-C4-H24; τ H9-C6-C7-H8; τ H17-C14-C15-H16; τ H23-C11-C12-H22
3	1195 (s)	1181 (m)	1181 (s)	1183 (s)	ν C1-N2; ν C18-N13; β C4-C5-C6; β C11-C10-C15
4	–	1222 (vw)	1227 (w)	1234 (w)	ν C3-C4; ν C6-C7; ν C11-C12; ν C14-C15
5	1298 (vs)	1283 (s)	1289 (m)	1290 (m)	ν C5-C10; ν C3-C4; ν C6-C7; ν C11-C12; ν C14-C15
7	1652 (m)	1656 (vs)	1649 (vs)	1644 (vs)	ν C3-C4; ν asym. C5-C6; ν asym. C11-C12; ν sym. C14-C15; ν asym. N2-C3; ν asym. C2-C7; β asym. H8-C7-N2; β H17-C14-N2; β H23-C11-C10; β asym. H24-C11-C10

Table 5.3 – Vibrations of thiram: Values from experimental (exp.), simulated (sim.) Raman spectra and from SERS spectra induced by gold and silver nanoparticles. v = very, w = weak, m = middle, s = strong, asym. = asymmetric, ν = stretching, β = bending τ = torsion.

Mode	Raman exp.	Raman sim.	SERS gold	SERS silver	Assignment
1	426 (w)	441 (w)	430 (w)	439 (w)	ν S8-C4; β C1-N2-C18; asym. β C10-N9-C14; β asym. N9-C7-S6; β asym. C7-S6-S5; β C10-N9-C14; β asym. C1-N2-C18; asym. β C3-N2-C18; asym. β N9-C7-S6
2	545 (vs)	570 (vs)	541 (m)	558 (m)	ν S5-C3; ν N2-C1; ν S6-C7; ν S5-C3; ν S5-S6; ν S4-C3; ν S8-C7; β C1-N2-C3; β asym. C1-N2-C18; β C7-N9-C10; β C1-N2-C3
3	841 (vw)	855 (vs)	848 (vw)	868 (vw)	ν N9-C10; ν asym. S6-C7; ν N2-C1; ν asym. S5-C3; ν N9-C14; ν N2-C18; ν N2-C13; ν N9-C7
4	965 (w)	991 (w)	925 (m)	927 (w)	ν S4-C3; ν asym. S8-C7; ν asym. N2-C18; ν asym. N9-C7
5	1141 (vw)	1154 (vw)	1139 (m)	1145 (m)	ν asym. C1-H27; β H16-C14-H13; β asym. H15-C14-H17; β asym. H15-C14-H16; β asym. H11-C10-H13
6	1369 (w)	1375 (vw)	1379 (vs)	1383 (vs)	ν N9-C7; ν N2-C3; ν asym. N2-C1; β asym. H12-C10-H13; β H11-C10-H12

...

Table 5.3 – Vibrations of thiram: Values from experimental (exp.), simulated (sim.) Raman spectra and from SERS spectra induced by gold and silver nanoparticles. v = very, w = weak, m = middle, s = strong, asym. = asymmetric, ν = stretching, β = bending τ = torsion. (*continuation*)

Mode	Raman exp.	Raman sim.	SERS gold	SERS silver	Assignment
7	1392 (w)	1405 (vw)	1440 (w)	1441 (m)	β H15-C14-H16; β H15-C14-H17; β H16-C14-H17; β asym. H12-C10-C-H13; β asym. H11-C10-H13
8	1455 (w)	1500 (w)	1508 (m)	1518 (s)	ν N2-C3; ν asym. N9-C7; ν asym. N2-C1; β H19-C18-H21; β H23-C1-H24; β H22-C1-H24; β asym. H15-C14-H17

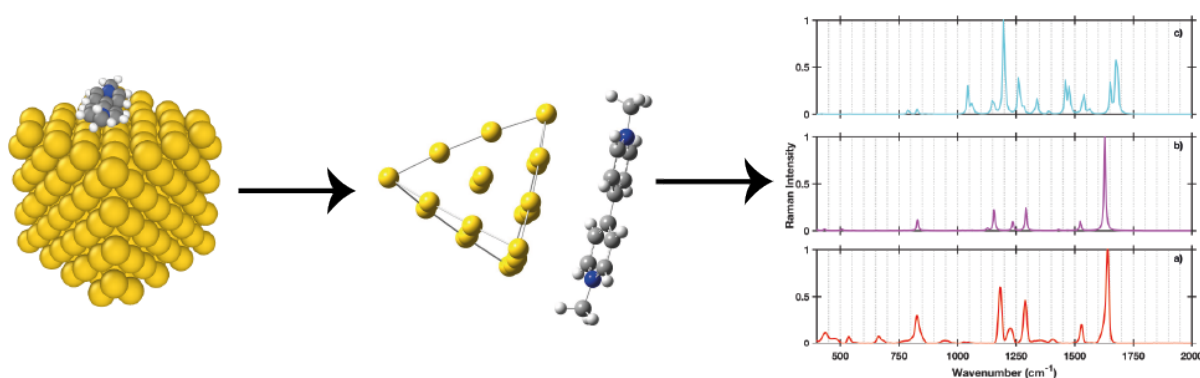
References

1. Tsagkaris, A. S., Uttl, L., Pulkrabova, J. & Hajslova, J. Screening of Carbamate and Organophosphate Pesticides in Food Matrices Using an Affordable and Simple Spectrophotometric Acetylcholinesterase Assay. *Applied Sciences* **10**, 565 (2020).
2. Authority, E. F. S. Evaluation of the data on clothianidin, imidacloprid and thiamethoxam for the updated risk assessment to bees for seed treatments and granules in the EU. *EFSA Supporting Publications* **15**, 1378E (2018).
3. Agency, U. E. P. Guidance for Assessing Pesticide Risks to Bees. *Health Canada Pest Management Regulatory Agency (PMRA), and California Department of Pesticide Regulation* (2014).
4. Ding, Z., Lin, M., Song, X., Wu, H. & Xiao, J. Quantitative Modeling of the Degradation of Pesticide Residues in Wheat Flour Supply Chain. *Foods* **12**, 788 (2023).
5. Hermsen, A., Lamers, D., Schoettl, J., Mayer, C. & Jaeger, M. In-field detection method for imidacloprid by surface enhanced Raman spectroscopy. *Toxicological & Environmental Chemistry* **104**, 36–54 (2022).
6. Moskovits, M. Surface-enhanced Raman spectroscopy: a brief retrospective. *Journal of Raman Spectroscopy* **36**, 485–496 (2005).
7. Hermsen, A., Schoettl, J., Hertel, F., *et al.* Green Textile Materials for Surface Enhanced Raman Spectroscopy Identification of Pesticides Using a Raman Handheld Spectrometer for In-Field Detection. *Applied Spectroscopy* **76**, 1222–1233 (2022).
8. Atanasov, P. A., Nedyalkov, N. N., Fukata, N., Jevasuwan, W. & Subramani, T. Surface-enhanced Raman spectroscopy of neonicotinoid insecticide imidacloprid, assisted by gold and silver nanostructures. *Spectroscopy Letters* **53**, 184–193 (2020).
9. Potts, J. C., Jain, A., Amabilino, D. B., Rawson, F. J. & Perez-Garcia, L. Molecular Surface Quantification of Multifunctionalized Gold Nanoparticles Using UV-Visible Absorption Spectroscopy Deconvolution. *Analytical Chemistry* **95**, 12998–13002 (2023).
10. Bharati, M. S. S. & Soma, V. R. Flexible SERS substrates for hazardous materials detection: recent advances. *Opto-Electron Advances* **4**, 210048 (2021).
11. Jiang, L., Hassan, M. M., Ali, S., *et al.* Evolving trends in SERS-based techniques for food quality and safety: A review. *Trends in Food Science & Technology* **112**, 225–240 (2021).
12. Pang, S., Yang, T. & He, L. Review of surface enhanced Raman spectroscopic (SERS) detection of synthetic chemical pesticides. *Trends in Analytical Chemistry* **85**, 73–82 (2016).
13. Pilot, R., Signorini, R., Durante, C., *et al.* A Review on Surface-Enhanced Raman Scattering. *Biosensors* **9** (2019).
14. Madzharova, F., Heiner, Z. & Kneipp, J. Surface Enhanced Hyper-Raman Scattering of the Amino Acids Tryptophan, Histidine, Phenylalanine, and Tyrosine. *The Journal of Physical Chemistry C* **121**, 1235–1242 (2017).
15. Salthammer, T., Grimme, S., Stahn, M., Hohm, U. & Palm, W.-U. Quantum Chemical Calculation and Evaluation of Partition Coefficients for Classical and Emerging Environmentally Relevant Organic Compounds. *Environmental Science & Technology* **56**, 379–391 (2022).

16. Grimme, S., Bannwarth, C. & Shushkov, P. A Robust and Accurate Tight-Binding Quantum Chemical Method for Structures, Vibrational Frequencies, and Noncovalent Interactions of Large Molecular Systems Parametrized for All spd-Block Elements ($Z = 1-86$). *Journal of Chemical Theory and Computation* **13**, 1989–2009 (2017).
17. Frens, G. Controlled Nucleation for the Regulation of the Particle Size in Monodisperse Gold Suspensions. *Nature Physical Science* **241**, 20–22 (1973).
18. Kimling, J., Maier, M., Okenve, B., *et al.* Turkevich Method for Gold Nanoparticle Synthesis Revisited. *The Journal of Physical Chemistry B* **110**, 15700–15707 (2006).
19. Turkevich, J., Stevenson, P. C. & Hillier, J. A study of the nucleation and growth processes in the synthesis of colloidal gold. *Discussions of the Faraday Society* **11**, 55–75 (1951).
20. Lee, P. C. & Meisel, D. Surface-enhanced Raman scattering of colloid-stabilizer systems. *Chemical Physics Letters* **99**, 262–265 (1983).
21. Lee, P. C. & Meisel, D. Adsorption and surface-enhanced Raman of dyes on silver and gold sols. *The Journal of Physical Chemistry* **86**, 3391–3395 (1982).
22. Wang, P., Wu, L., Lu, Z., *et al.* Gecko-Inspired Nanotentacle Surface-Enhanced Raman Spectroscopy Substrate for Sampling and Reliable Detection of Pesticide Residues in Fruits and Vegetables. *Analytical Chemistry* **89**, 2424–2431 (2017).
23. Savitzky, A. & Golay, M. J. E. Smoothing and Differentiation of Data by Simplified Least Squares Procedures. *Analytical Chemistry* **36**, 1627–1639 (1964).
24. Schulze, H. G., Foist, R. B., Okuda, K., Ivanov, A. & Turner, R. F. B. A Small-Window Moving Average-Based Fully Automated Baseline Estimation Method for Raman Spectra. *Applied Spectroscopy* **66**, 757–764 (2012).
25. Grimme, S. Exploration of Chemical Compound, Conformer, and Reaction Space with Meta-Dynamics Simulations Based on Tight-Binding Quantum Chemical Calculations. *Journal of Chemical Theory and Computation* **15**, 2847–2862 (2019).
26. Pracht, P., Caldeweyher, E., Ehlert, S. & Grimme, S. A Robust Non-Self-Consistent Tight-Binding Quantum Chemistry Method for Large Molecules Computational Chemistry at Frustrated Lewis Pair Systems View Project. *ChemRxiv* **1-2**, 8326202 (2019).
27. Pracht, P., Bohle, F. & Grimme, S. Automated exploration of the low-energy chemical space with fast quantum chemical methods. *Physical Chemistry Chemical Physics* **22**, 7169–7192 (2020).
28. Frisch, M. J., Trucks, G. W., Schlegel, H. B., *et al.* *Gaussian 16 Revision C.01* Gaussian Inc. Wallingford CT. 2016.
29. Becke, A. D. Density-Functional Exchange-Energy Approximation with Correct Asymptotic Behavior. *American Physical Society* **38**, 3098 (1988).
30. Becke, A. D. Density-Functional Thermochemistry. III. The Role of Exact Exchange. *Journal of Chemical Physics* **37**, 5648–5652 (1993).
31. Lee, C., Yang, W. & Parr, R. G. Development of the Colle-Salvetti correlation-energy formula into a functional of the electron density. *Physical Review B* **37**, 785–789 (1988).

32. Woon, D. E. & Dunning Thom H., J. Calculation of the electron affinities of the second row atoms: Al–Cl. *The Journal of Chemical Physics* **99**, 3730–3737 (1993).
33. Kendall, R. A., Dunning Thom H., J. & Harrison, R. J. Electron affinities of the first-row atoms revisited. Systematic basis sets and wave functions. *The Journal of Chemical Physics* **96**, 6796–6806 (1992).
34. Johnson, R. D. I., Irikura, K. K., Kacker, R. N. & Kessel, R. Scaling Factors and Uncertainties for ab Initio Anharmonic Vibrational Frequencies. *Journal of Chemical Theory and Computation* **6**, 2822–2828 (2010).
35. Jamroz, M. Vibrational Energy Distribution Analysis (VEDA): Scopes and limitations. *Spectrochimica Acta Part A: Molecular and Biomolecular Spectroscopy* **114**, 220–230 (2013).
36. Ferreira, J. Theoretical Study of the Reduction Reaction and Conformational Analysis of Paraquat by Density Functional Theory. *Archives of Chemistry and Chemical Engineering* **3**, 220–230 (2021).
37. Kleier, D. A. & Weeks, G. H. Electronic structure and conformational analysis of paraquat in three oxidation states. *Journal of Molecular Structure: THEOCHEM* **148**, 25–31 (1986).
38. Kreisig, S., Tarazona, A. & Koglin, E. The Adsorption of Paraquat on Silver Electrode Surfaces: A SERS Microprobe Study. *Electrochim. Acta.* **42**, 3335–3344 (1997).
39. Canamares, M. V., Pozzi, F. & Lombardi, J. R. Raman, SERS, and DFT Analysis of the Main Alkaloids Contained in Syrian Rue. *The Journal of Physical Chemistry C* **123**, 9262–9271 (2019).
40. Ngo, T. C., Trinh, Q. T., Thi Thai An, N., *et al.* SERS Spectra of the Pesticide Chlorpyrifos Adsorbed on Silver Nanosurface: The Ag₂₀ Cluster Model. *The Journal of Physical Chemistry C* **124**, 21702–21716 (2020).
41. Zhao, Y. & Truhlar, D. G. Design of Density Functionals That Are Broadly Accurate for Thermochemistry, Thermochemical Kinetics, and Nonbonded Interactions. *The Journal of Physical Chemistry A* **109**, 5656–5667 (2005).
42. Lin, M.-H., Sun, L., Kong, F. & Lin, M. Rapid detection of paraquat residues in green tea using surface-enhanced Raman spectroscopy (SERS) coupled with gold nanostars. *Food Control* **130**, 108280 (2021).
43. Tsen, C.-M., Yu, C.-W., Chuang, W.-C., *et al.* A simple approach for the ultrasensitive detection of paraquat residue in adzuki beans by surface-enhanced Raman scattering. *Analyst* **144**, 426–438 (2019).
44. Botta, R., Eiamchai, P., Horprathum, M., *et al.* 3D structured laser engraves decorated with gold nanoparticle SERS chips for paraquat herbicide detection in environments. *Sensors and Actuators B: Chemical* **304**, 127327 (2020).
45. Kang, J.-S. & Lee, M.-S. SERS of Dithiocarbamate Pesticides Adsorbed on Silver Surface; Thiram. *Bulletin of the Korean Chemical Society* **23**, 1604–1610 (2002).

6 MD and DFT Calculations to Analyze Raman and SERS Spectra of Paraquat—From Computer Aided Spectra Interpretation to Pesticide Identification



Chapter 6 is reproduced from *Andrea Hermsen, Florian Hertel, Dominik Wilbert, Christian Mayer & Martin Jaeger (2024) MD and DFT Calculations to Analyze Raman and SERS Spectra of Paraquat—From Computer Aided Spectra Interpretation to Pesticide Identification, Applied Research, DOI: <https://doi.org/10.1002/appl.202400182>*, with permission from Wiley.

6.1 Abstract

The use of pesticides is an important practice in today's agricultural and nutritional supply chain worldwide. Their potentially harmful effects require rapid and reliable monitoring. As an emerging technology, surface enhanced Raman spectroscopy (SERS) is paving its way through established methodologies. The Raman enhancing effect is based on the interaction of the analyte and nanoparticles prepared from noble metals. To better support and exploit analytical applications, the interaction between gold nanoparticles and the pesticide paraquat were studied. To this purpose, molecular dynamic calculations were performed with paraquat on single-crystal structures of gold at a distance of 3.4 Å and an intramolecular dihedral angle of 18.8° between the two paraquat ring systems. The molecular dynamic calculations showed that the two noble metal surface models exhibited only slight differences in their effects on paraquat. Experimental SERS spectra with gold nanoparticles were recorded and compared to the experimental Raman spectrum. The observed differences were further investigated using density functional theory calculations and reducing the gold cell to a gold cluster of twenty atoms. A co-planar orientation of paraquat to the gold cluster surface was thereby deduced. Based on an optimized paraquat geometry including a dihedral angle of 36.77° at a distance of 3.85 Å to the gold cluster, an excellent agreement between computed and experimental spectra was obtained. A head-on geometry was discarded due to spectral mismatch. This computational approach may help to analyze SERS spectra and make SERS further suitable for pesticide analysis.

6.2 Introduction

Pesticides are applied worldwide to increase agricultural yields. Yet, their environmentally harmful potential has long been known. Public interest and awareness have grown steadily. Environmental authorities have hence restricted the application and issued monitoring regulations.^{1,2} The requirements to monitor pesticide utilization in open fields and greenhouses have created a demand for more suitable mobile on-site methods to allow fast and cost-effective analysis procedures.^{3,4} SERS spectroscopy is among the most recent methodologies and is paving its way to a promising application.^{5,6} Its major advantage and expectation is its high sensitivity, its comparably inexpensive instrumentation, its ease of use and its sample throughput. As a prerequisite for quick and easy sample preparation, is the availability of suitable liquid matrices or solid-support substrates.⁶⁻⁸ To this purpose, noble metals such as gold and silver can be used, from which colloids and derived structures therefrom can then be prepared e.g., by wet chemistry.^{5,9,10} The noble metal colloids can further be transformed into liquid or solid substrates, either as colloidal solutions themselves or immobilized on various supports as SERS substrates. Analytes are then dissolved and transferred into the colloidal solutions or onto the substrates for analysis using Raman spectroscopy.^{10,11} The variety of substrates is very large, ranging from filter paper or textile material to substrates produced by laser ablation or gas deposition.^{7,12,13} Depending on the noble metals and sub-

strate structures, different spectra are obtained from the same analyte by SERS spectroscopy. Since the dependence of the analyte spectra on the SERS substrates renders identification and quantitation more difficult, it is important to understand the interdependence better. To this purpose, computational chemistry methods may be applied.⁸ These methods consist of simulations, molecular dynamics (MD) and density functional theory (DFT) calculations. As a general trend, computer chemistry is finding its way more and more into the field of environmental analysis, accelerated by the ever-advancing state of computer technology.¹⁴⁻¹⁶ MD calculations are suitable to investigate the behavior of a molecule on any surface, which can provide information about surface-molecule interactions. In contrast, DFT calculations allow to predict chemical properties of chemical substances, such as vibrational spectra.¹⁷⁻²¹ In a preceding study, the paraquat signal assignments were reported in great detail for the Raman and SERS spectra resulting from gold and silver nanoparticles.⁸ Computations also showed that the methylene groups of paraquat had electronegative potential. In this study, the system paraquat on a gold cell was investigated using molecular dynamics with particular attention to intramolecular dihedral angles, bond lengths, and the arrangement between the gold cell and the molecule. Density Functional Theory calculations were used to examine different orientations between the gold cluster and paraquat. The intramolecular angles obtained from MD and DFT calculations were compared. The orientations of paraquat on the gold surface were analyzed and translated into Raman spectra. Finally, the agreement between the computed and experimental Raman and SERS spectra was evaluated with respect to the potential applicability for paraquat identification by SERS.

6.3 Materials & Methods

Chemicals were purchased from Sigma Aldrich, Darmstadt, Germany, and used without further purification. Paraquat were purchased from Pestanal[®] Series, Sigma Aldrich. A stock solution of paraquat (0.1 mM) was prepared and used for all experiments. Gold nanospheres were prepared according to previously published methods.²²⁻²⁴ In brief, 1.25 mL of hydrochloric acid (10 mmol/L) and 450 μ l of 1% trisodium citrate were successively added to 50 mL of deionized water at 80 °C. The solution was stirred at 500 rpm and, after the color changed from yellow to red, kept at 80 °C. The solution was stirred for another 5 min, then cooled to ambient temperature while stirring. The entire synthesis was carried out under a nitrogen atmosphere. Characterization of the gold nanospheres and the size distribution were determined as described previously.^{6,8} Raman and SERS measurements were performed on Raman readers, Ocean Insight, Dunedin, FL, USA, equipped with a laser of 785 nm excitation wavelength with 70 mW. For SERS experiments in solution, samples were transferred into 2mL borosilicate glass vials, Glass Vials, Hannover, MD, USA. Subsequently, 1mL of the nanoparticle solution, 0.5 mL of deionized water, 100 μ L of paraquat, and 100 μ L of 1 M hydrochloric acid were added into the vial. For spectra processing, sixteen spectra were accumulated and averaged with Ocean View software, Ocean Insight, Dunedin, FL, USA. Spectra were smoothed using a Savitzky-Golay filter over 11 points and a polynomial

of grade 3 using MATLAB R2019b, Update 3, MathWorks, Natick, MA, USA.²⁵ Baseline correction was performed using the same software with the algorithm of Schulze et al. for Raman baseline correction.²⁶ Ab initio molecular dynamics (AIMD) simulations based on the Born–Oppenheimer scheme, as implemented in the VASP code,²⁷ were performed at the Brillouin point. Canonical ensembles (NVT ensembles) were imposed on the system using a Nosé–Hoover thermostat with target temperatures of 300 K. The simulations were run for a production phase of approximately 10 ps, using a simulation time step of 0.5 fs after an equilibration time of 1 ps. The forces for the AIMD simulation were also calculated using density functional theory. The PBE functional was utilized to treat electronic exchange and correlation effects.²⁸ The ionic cores were described by Projector Augmented Wave (PAW) potentials, as derived by Kresse and Joubert.^{29–31} The wave functions were expanded in a plane-wave basis set up to a cutoff energy of 400 eV for all four elements (i.e., Au, C, N, and H). To account for dispersion interactions, the Grimme D3 correction was added to the PBE exchange-correlation functional.^{32–34} The simulation cell consisted of a gold slab consisting of 8 layers in contact with a paraquat molecule. A vacuum region of 15 Å thickness above the gold surface was added in the z-direction in order to avoid the periodic interaction between the top and bottom of the slab. To cancel part of the electric field gradient in vacuum, a dipole correction in the z-direction was introduced.³⁵ Quantum chemical calculations were performed using Gaussian 16 software package.³⁶ For preoptimization, the functional B3LYP and basis-set 6-21G were used to exclude the conformers with cut-off values of 1%. The hybrid functional PW6B95D3 and the basis-set aug-cc-pVTZ with a (99,590) Lebedev grid was applied for final optimization of paraquat structures. The basis set LANL2DZ was used for gold and silver cluster simulations.^{37,38} The convergence thresholds were chosen as follows: maximum force per atom smaller than 4.5×10^{-1} Ha Å⁻¹, RMS force per atom smaller than 3.0×10^{-4} Ha Å⁻¹ maximum atomic displacement smaller than 18.0×10^{-4} Å, and RMS displacement smaller than 12×10^{-4} Å. During frequency calculation, no imaginary frequencies were obtained, such that the geometries represented a stable structure corresponding to a minimum of the potential energy surface. For Lorentzian broadening of the calculated modes, 4 cm⁻¹ half-width at full maximum was chosen. All simulated spectra were scaled using a factor of 0.97. The potential energy distribution of each vibration was used to analyze the simulation data of the vibration modes. For the simulation of the gold atom interactions with the paraquat molecule, AIMD simulation was used based on 256 gold atoms for a gold cell. For the spectral simulations using Gaussian, a gold cluster was used consisting of 20 gold atoms with a pyramidal arrangement. To calculate SERS spectra, two different orientations between the gold cluster and the paraquat molecule were chosen. The first orientation was a head-on arrangement, where the methylene group of paraquat was oriented towards the planar side of the gold pyramid. For the second co-planar orientation, the paraquat molecule was arranged in a co-planar manner with respect to the planar side of the gold pyramid.

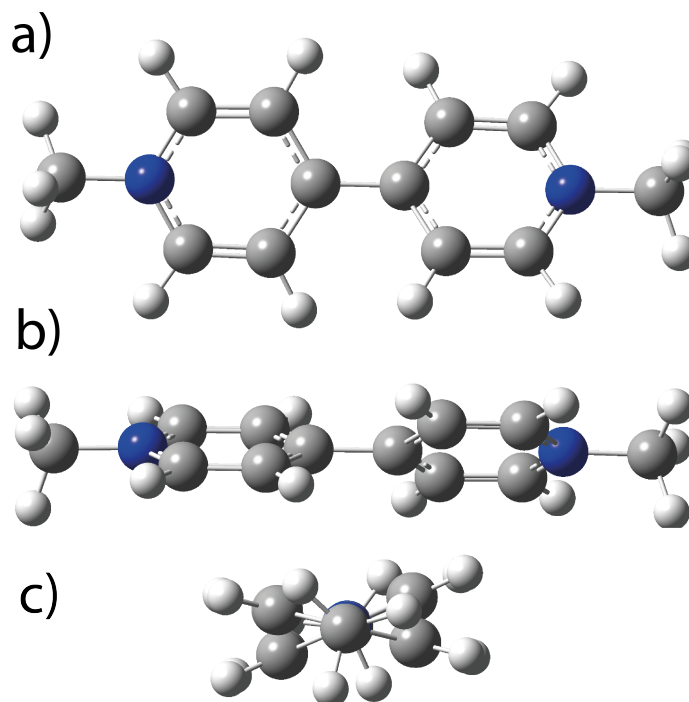


Figure 6.1 – Optimized structural geometry of paraquat, with its a) front, b) side and its c) perspective view.

6.4 Results & Discussion

The optimized structure of paraquat is shown in Fig. 6.1. All further calculations were carried out on the basis of this structure.

The optimized paraquat structure was taken to molecular dynamics calculations. A period of 10 ps was chosen. The intramolecular distances of paraquat, i.e. the C-C, C-N and C-H bond lengths, remained unaltered over the entire simulation period, cf. supplemental information 6.7. The molecule was centered on a single crystal of gold atoms as shown in Fig. 6.2. The single crystals represented a fraction of the gold nanoparticle. MD computations allowed to investigate the dynamic behavior of the paraquat molecule on the gold surface. As a results, the distance between the gold atoms and the paraquat molecule were about 3.4 Å on average.

For the paraquat molecule located on the gold cell, the bond lengths of the C-H were about 1.0967 Å, C-C 1.4086 Å and C-N 1.4036 Å, respectively. For the paraquat molecule on the gold cell the dihedral angle for C4-C5-C10-C11 was about 18.8°. So those dihedral angles differed from the dihedral angle found at our previous DFT study and the study of Ferreira et al., where a dihedral angle of 40° was reported.^{8,39} Proud and Murray-Rust determined the structure of paraquat by single-crystal X-ray diffraction.⁴⁰ Only in their study, a dihedral angle of 0° for C4-C5-C10-C11 was determined. This exceptional angle can be assumed due to the crystal packing effects and is likely not relevant for paraquat in solutions or interacting with nanoparticle surfaces. Since a detailed band assignment was reported in a previous study, only the most prominent bands relevant for the current study will be given here, cf. Fig. 6.3.⁸ The band at 832 cm⁻¹ stems from a breathing oscillation. This mode was visible both in the

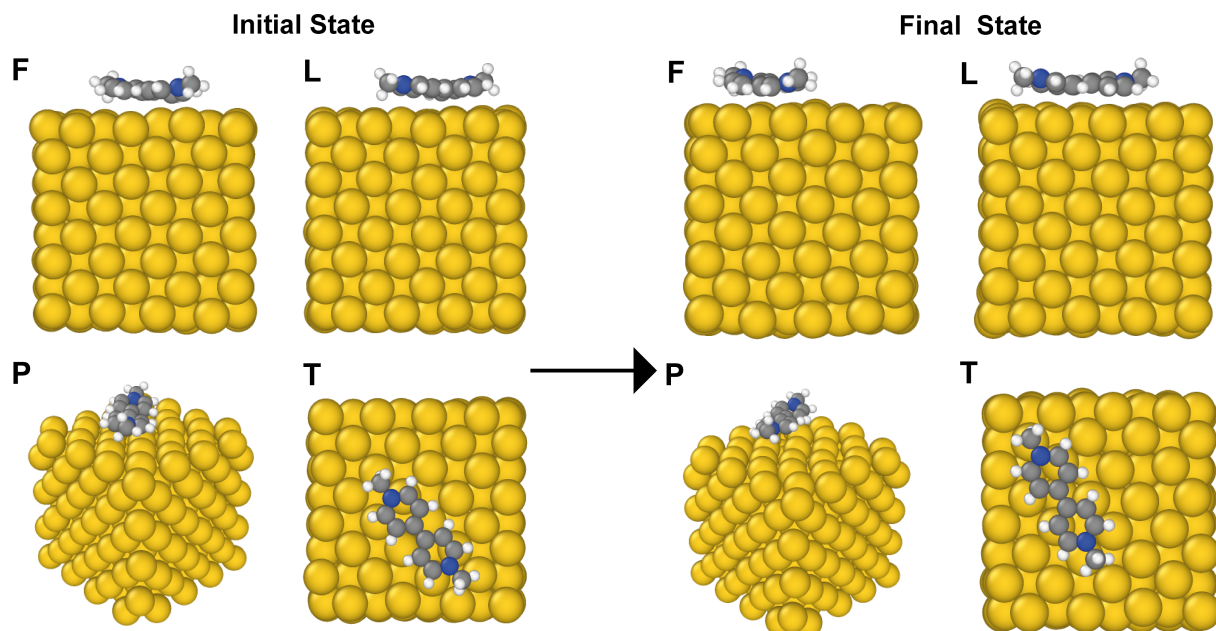


Figure 6.2 – Snapshot of initial and final arrangement (front (F) left (L), perspective (P), and top (T) views) between paraquat molecule and gold cell.

Raman and the SERS spectrum with gold nanoparticles. The band at 1195 cm^{-1} represents combination of stretching and bending vibrations as a result of the stretching of the C-N bond and the bending of the carbon atoms in the ring system. The mode at 1222 cm^{-1} could only be detected in the SERS spectra. It is tentatively assigned to a stretching oscillation of the ring system. The peak at 1550 cm^{-1} is caused by a strong stretching vibration of the atoms C5 and C10, affecting the bond between the two ring systems. The methyl groups undergo bending vibrations. The mode with the highest intensity was observed at a wavenumber of 1652 cm^{-1} and is caused by the vibrations of the C-N bond and the C=C bond in the ring system.

The previously reported orientation of paraquat on a gold surface could be further refined using the current results.⁸ A co-planar orientation of the molecules seemed most likely. The orientation has a significant effect on the physico-chemical properties of the system and hence on the resulting Raman spectra, as can be seen from the comparison of the computed spectra in Fig. 6.4. It can further be recognized that the co-planar arrangement led to an excellent agreement of the computed SERS spectrum with the experimental one. The peak at 1222 cm^{-1} was observed in the SERS spectrum but was not visible in the Raman spectrum with the head-on arrangement. In contrast, the computation based on the co-planar arrangement yielded this peak. This observation pointed towards the co-planar orientation of the paraquat molecule on the gold surface.

Easier and faster computations were achieved by replacing the gold cell through an Au-20 gold cluster. The different arrangements of the paraquat molecule with respect to the Au-20 cluster are shown in Fig. 6.5 and 6.6. The starting geometries for the optimization are shown on the left and the final optimized geometry on the right. For the head-on geometry, cf. Fig. 6.5, the paraquat molecule was orientated with its methylene group pointing to the

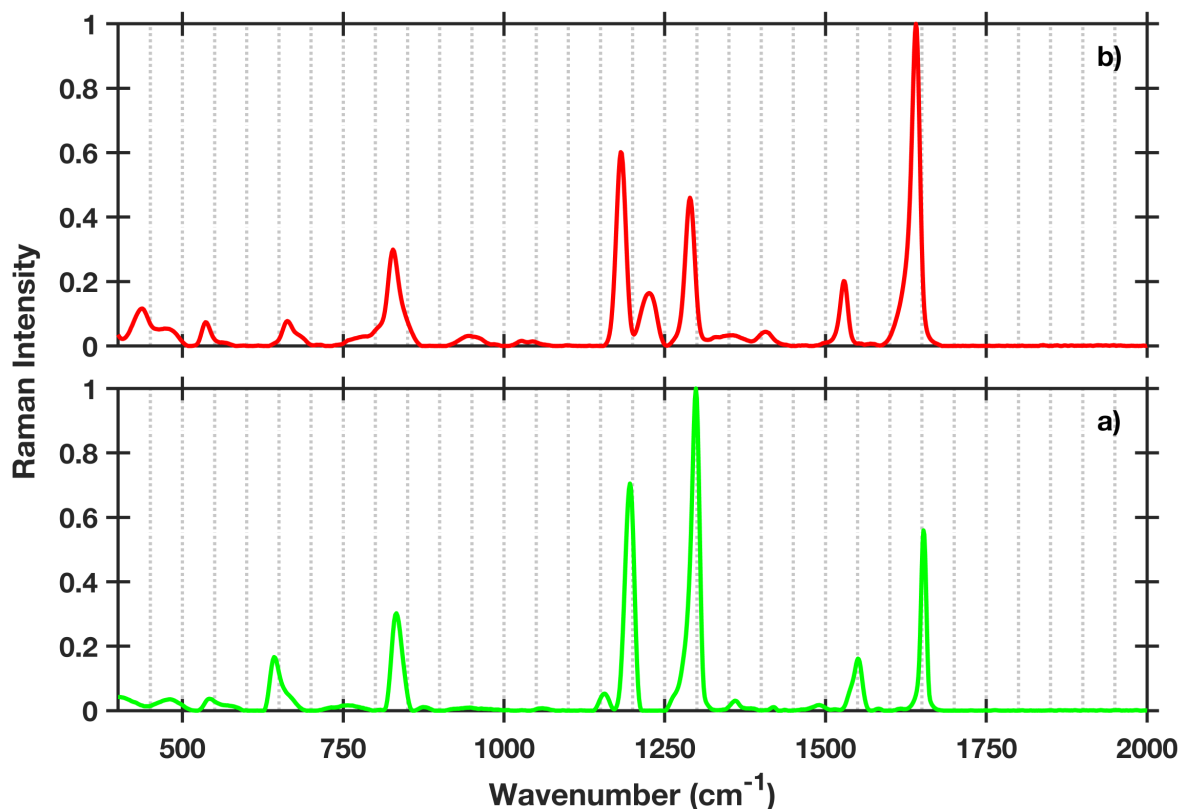


Figure 6.3 – Experimental Raman spectrum of Paraquat (a) and experimental SERS spectrum using gold nanoparticles (b).

Au-20 gold cluster. The distance between the paraquat molecule and the Au cluster was set to 1.4 Å between the gold atom at the center of the surface and the C1 atom of the paraquat molecule. After the geometry optimization the distance between the gold atom and the C1 atom changed to 3.62 Å. The dihedral angle of the atoms C4-C5-C10-C11 changed from 36.77° to 21.79°. The intramolecular bond distances did not change, as expected.

To achieve convergence faster, the paraquat molecule was placed to the Au-20 gold cluster at a distance of 3.62 Å between the centered gold atom and the C1 for the starting geometry, cf. Fig. 6.6. The dihedral angle represented by C4-C5-C10-C11 was 36.77°. After optimization, the distance between the gold atom and the C1 atom increased slightly to 3.85 Å and the dihedral angle changed to 34.29°. The distance between the gold cluster and the paraquat molecule was hence rather similar for both orientations, while the dihedral angle differed significantly. The dihedral angle of the planar arrangement was found close to that of the free molecule. In contrast, the head-on orientation led to a significantly different spectral prediction. Since the Raman spectrum matched the experimental SERS spectrum very well, a co-planar arrangement of paraquat towards the gold surface seemed likely. The spectral difference may be explained in terms of the significant differences in polarizability between the head-on and co-planar orientations due to the interaction of the gold orbitals with the aromatic system of paraquat or its methyl group.

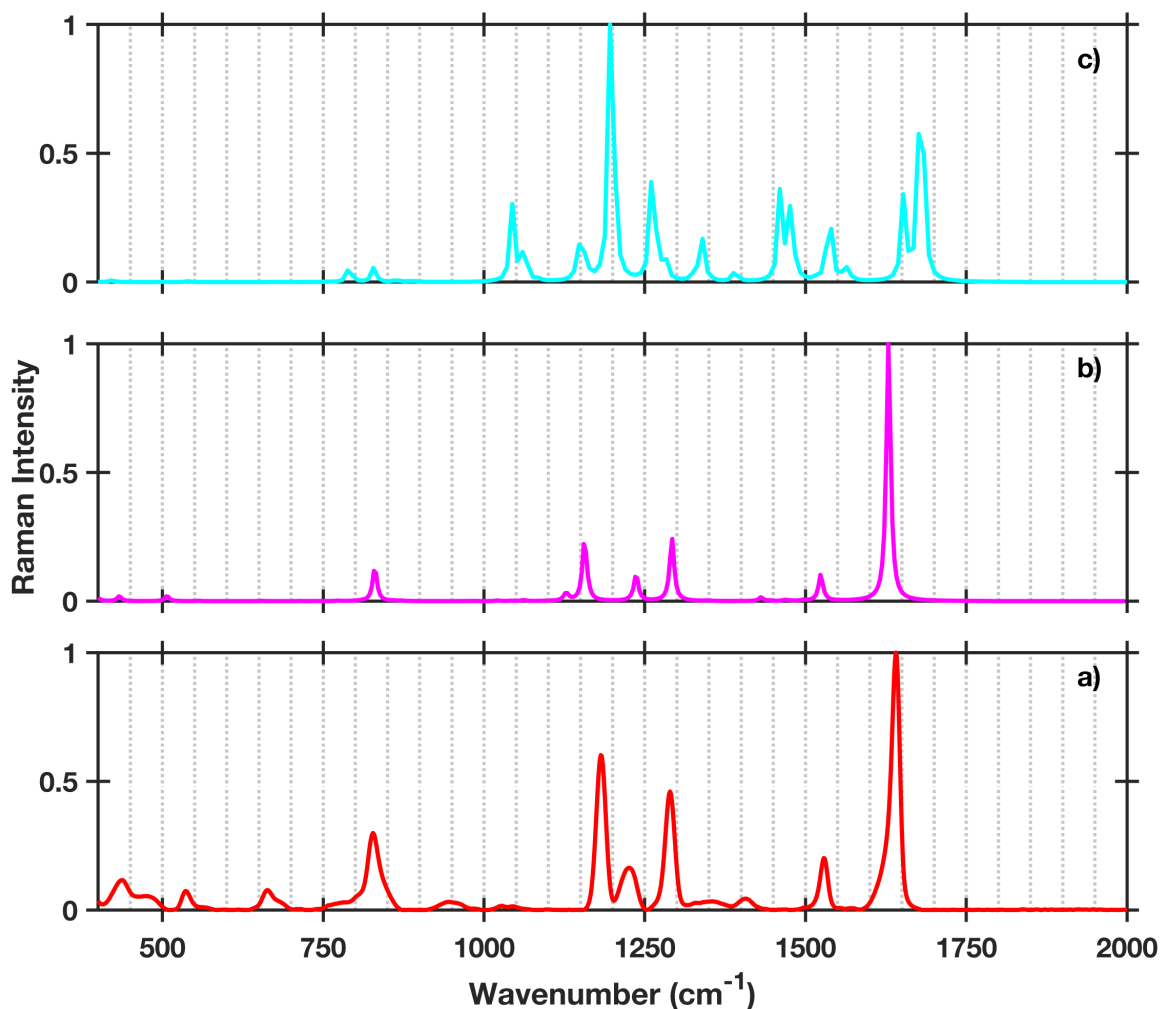


Figure 6.4 – Experimental a) SERS spectrum with gold nanoparticles and computed Raman spectra with b) co-planar and c) head-on orientations.

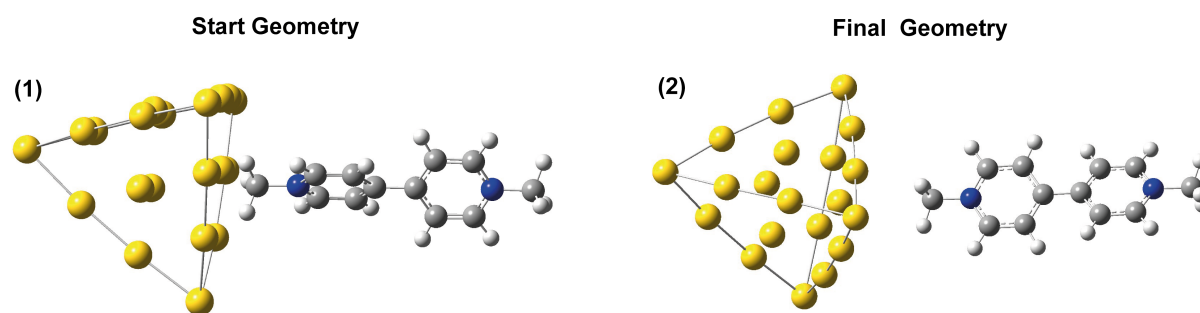


Figure 6.5 – Initial, (1) and final, (2) orientation of paraquat attached to the gold cluster with a head-on orientation.

Assuming the head-on arrangement, the methyl groups might favorably interact with the gold atoms electron shell. The altered electron distribution would hence increase the electronic contribution to the geometry and counteract the steric repulsion of the two aromatic pyridinium rings. As a result, the dihedral angle would decrease. The computation

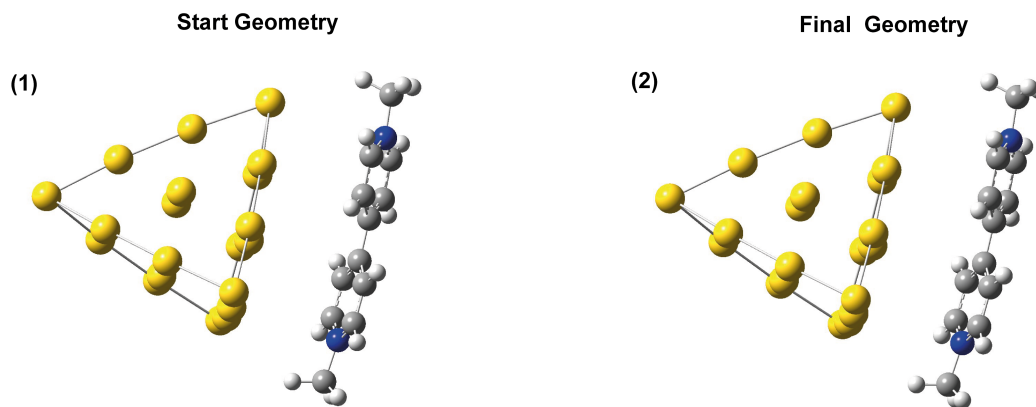


Figure 6.6 – Initial, (1) and final, (2) orientation of paraquat attached to the gold cluster with a planar orientation.

yielded a value of 21.79° . Due to the altered geometry, the simulated Raman spectra changed significantly, cf. Fig. 6.4c. The dihedral angle change would then alter the modes at 850 and 1550 cm^{-1} . The simulations revealed the influence of the geometry on the Raman spectra, where the orientation of the aromatic rings, i.e. the dihedral angle C4-C5-C10-C11, played a major role. The computation indicated further that a co-planar arrangement would allow a geometry more similar to the free species, while a head-on orientation would favor the formation a charge-transfer complex and thus enforce a significant geometry alteration. In contrast, the results of the computational simulations of the two orientations suggested that the co-planar orientation did not induce strong chemical interactions or only minimal interactions. The good agreement between the gas-phase like molecule and the SERS spectrum and the conserved dihedral angle C4-C5-C10-C11 might indicate the absence of a charge-transfer complex. The occurrence of a charge-transfer complex might have caused the appearance of signal shifts. With paraquat, signal wavenumbers were conserved, while intensities were enhanced by the electronic SERS effect due to the proximity of the molecule to the gold cluster. In consequence, the good agreement with the experimental SERS spectrum and the spectrum computed on the basis of a co-planar arrangement should be taken indicative for the co-planar orientation between paraquat and the gold nanoparticle surface.

6.5 Conclusion

The molecular dynamics simulations showed that paraquat on the gold surface of the single crystal assumed a dihedral angle C4-C5-C10-C11 of 18.8° , with the intramolecular bond lengths conserved over simulation time. The average distance between the gold single-crystal and the paraquat molecule was found about 3.4 \AA . Using DFT calculations for refinement, dihedral angles of 34° for the planar arrangement and 22° for the head-on arrangement were obtained. It was found that the co-planar arrangement with the larger dihedral angle led to an excellent agreement between computed Raman and experimental SERS spectra. Hence, the paraquat geometry on interaction with a gold surface may resemble

that of the free paraquat. Further to the structural insight, the presented computational approach may facilitate the analysis of SERS spectra and amend SERS towards mobile pesticide analysis. Especially the targeted combination of MD and ab-initio simulations can significantly simplify the evaluation of SERS spectra and their utilization in structural and analytical chemistry in the future.

6.6 Supplemental Information

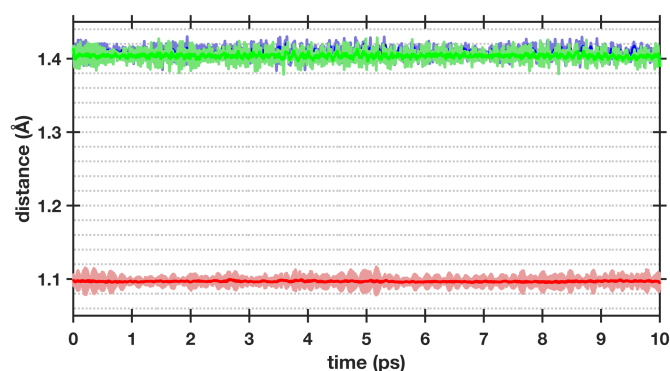


Figure 6.7 – Intramolecular bond lengths during the MD simulation of paraquat molecule on Au cluster with the bond length of C-N (green) with a mean of 1.4036 Å, C-C (blue) with a mean of 1.4086 Å and C-H (red) with a mean of 1.0967 Å

References

1. Authority, E. F. S. Evaluation of the data on clothianidin, imidacloprid and thiamethoxam for the updated risk assessment to bees for seed treatments and granules in the EU. *EFSA Supporting Publications* **15**, 1378E (2018).
2. Agency, U. E. P. Guidance for Assessing Pesticide Risks to Bees. *Health Canada Pest Management Regulatory Agency (PMRA), and California Department of Pesticide Regulation* (2014).
3. Tsagkaris, A. S., Uttl, L., Pulkrabova, J. & Hajslova, J. Screening of Carbamate and Organophosphate Pesticides in Food Matrices Using an Affordable and Simple Spectrophotometric Acetylcholinesterase Assay. *Applied Sciences* **10**, 565 (2020).
4. Yang, C., Fang, S., Tsai, H., Chen, J. & Liu, Y. Newly prepared surface-enhanced Raman scattering-active substrates for sensing pesticides. *Journal of Electroanalytical Chemistry* **861**, 113965 (2020).
5. Sitjar, J., Liao, J.-D., Lee, H., Liu, B. H. & Fu, W. SERS-Active Substrate with Collective Amplification Design for Trace Analysis of Pesticides. *Nanomaterials* **9**, 664 (2019).
6. Hermsen, A., Lamers, D., Schoettl, J., Mayer, C. & Jaeger, M. In-field detection method for imidacloprid by surface enhanced Raman spectroscopy. *Toxicological & Environmental Chemistry* **104**, 36–54 (2022).

7. Hermsen, A., Schoettl, J., Hertel, F., *et al.* Green Textile Materials for Surface Enhanced Raman Spectroscopy Identification of Pesticides Using a Raman Handheld Spectrometer for In-Field Detection. *Applied Spectroscopy* **76**, 1222–1233 (2022).
8. Hermsen, A., Hertel, F., Wilbert, D., *et al.* Pesticide Identification Using Surface-Enhanced Raman Spectroscopy and Density Functional Theory Calculations: From Structural Insights to On-Site Detection. *Applied Spectroscopy* **78**, 616–626 (2024).
9. Chen, D., Zhu, X., Huang, J., *et al.* Polydopamine@ gold nanowaxberry enabling improved SERS sensing of pesticides, pollutants, and explosives in complex samples. *Analytical chemistry* **90**, 9048–9054 (2018).
10. Creedon, N., Lovera, P., Moreno, J. G., Nolan, M. & O’Riordan, A. Highly sensitive SERS detection of neonicotinoid pesticides. Complete Raman spectral assignment of clothianidin and imidacloprid. *The Journal of Physical Chemistry A* **124**, 7238–7247 (2020).
11. Li, P., Chen, W., Liu, D., *et al.* Template growth of Au/Ag nanocomposites on phosphorene for sensitive SERS detection of pesticides. *Nanotechnology* **30**, 275604 (2019).
12. Atanasov, P., Nedyalkov, N., Nikov, R., *et al.* SERS of insecticides and fungicides assisted by Au and Ag nanostructures produced by laser techniques. *International Journal of Environmental & Agriculture Research* **3**, 61–69 (2017).
13. Atanasov, P. A., Nedyalkov, N. N., Fukata, N., Jevasuwan, W. & Subramani, T. Surface-enhanced Raman spectroscopy of neonicotinoid insecticide imidacloprid, assisted by gold and silver nanostructures. *Spectroscopy Letters* **53**, 184–193 (2020).
14. Silva, C. F., Borges, K. B. & Nascimento, C. S. Computational study on acetamiprid-molecular imprinted polymer. *Journal of molecular modeling* **25**, 1–5 (2019).
15. Bora, A., Avram, S., Funar-Timofei, S. & Halip, L. Computational electronic profile of the insecticide imidacloprid and analogues. *Revue Roumaine Chimie* **63**, 861–867 (2018).
16. Menard, K. J., Martens, J. & Fridgen, T. D. A vibrational spectroscopic and computational study of the structures of protonated imidacloprid and its fragmentation products in the gas phase. *Physical Chemistry Chemical Physics* **23**, 3377–3388 (2021).
17. Zhang, Y., Sun, S., Zhang, X., *et al.* Sulfate-ion-assisted galvanic replacement tuning of silver dendrites to highly branched chains for effective SERS. *Physical Chemistry Chemical Physics* **16**, 18918–18925 (2014).
18. Ngo, T. C., Trinh, Q. T., Thi Thai An, N., *et al.* SERS Spectra of the Pesticide Chlorpyrifos Adsorbed on Silver Nanosurface: The Ag₂₀ Cluster Model. *The Journal of Physical Chemistry C* **124**, 21702–21716 (2020).
19. Hieu, T. D., Chinh, N. T., Nhung, N. T. A., Quang, D. T. & Quang, D. D. SERS chemical enhancement by copper-nanostructures: Theoretical study of Thiram pesticide adsorbed on Cu₂₀ cluster. *Vietnam Journal of Chemistry* **59**, 159–166 (2021).
20. Wang, J., Wang, G. & Zhao, J. Structures and electronic properties of Cu₂₀, Ag₂₀, and Au₂₀ clusters with density functional method. *Chemical physics letters* **380**, 716–720 (2003).

21. Mohammed, A., Hu, W., Andersson, P. O., *et al.* Cluster approximations of chemically enhanced molecule-surface Raman spectra: The case of trans-1, 2-bis (4-pyridyl) ethylene (BPE) on gold. *Chemical Physics Letters* **581**, 70–73 (2013).
22. Frens, G. Controlled Nucleation for the Regulation of the Particle Size in Monodisperse Gold Suspensions. *Nature Physical Science* **241**, 20–22 (1973).
23. Kimling, J., Maier, M., Okenve, B., *et al.* Turkevich Method for Gold Nanoparticle Synthesis Revisited. *The Journal of Physical Chemistry B* **110**, 15700–15707 (2006).
24. Turkevich, J., Stevenson, P. C. & Hillier, J. A study of the nucleation and growth processes in the synthesis of colloidal gold. *Discussions of the Faraday Society* **11**, 55–75 (1951).
25. Savitzky, A. & Golay, M. J. E. Smoothing and Differentiation of Data by Simplified Least Squares Procedures. *Analytical Chemistry* **36**, 1627–1639 (1964).
26. Schulze, H. G., Foist, R. B., Okuda, K., Ivanov, A. & Turner, R. F. B. A Small-Window Moving Average-Based Fully Automated Baseline Estimation Method for Raman Spectra. *Applied Spectroscopy* **66**, 757–764 (2012).
27. Kresse, G. & Furthmüller, J. Efficient iterative schemes for ab initio total-energy calculations using a plane-wave basis set. *Physical Review B* **54**, 11169 (1996).
28. Perdew, J. P., Burke, K. & Ernzerhof, M. Generalized gradient approximation made simple. *Physical Review letters* **77**, 3865 (1996).
29. Blöchl, P. E. Projector augmented-wave method. *Physical Review B* **50**, 17953 (1994).
30. Kresse, G. & Joubert, D. From ultrasoft pseudopotentials to the projector augmented-wave method. *Physical Review B* **59**, 1758 (1999).
31. Kresse, G. & Furthmüller, J. Efficiency of ab-initio total energy calculations for metals and semiconductors using a plane-wave basis set. *Computational materials science* **6**, 15–50 (1996).
32. Grimme, S., Antony, J., Ehrlich, S. & Krieg, H. A consistent and accurate ab initio parametrization of density functional dispersion correction (DFT-D) for the 94 elements H-Pu. *The Journal of chemical physics* **132**, 154104 (2010).
33. Grimme, S. Density functional theory with London dispersion corrections. *Wiley Interdisciplinary Reviews: Computational Molecular Science* **1**, 211–228 (2011).
34. Grimme, S., Hansen, A., Brandenburg, J. G. & Bannwarth, C. Dispersion-corrected mean-field electronic structure methods. *Chemical Reviews* **116**, 5105–5154 (2016).
35. Neugebauer, J. & Scheffler, M. Adsorbate-substrate and adsorbate-adsorbate interactions of Na and K adlayers on Al (111). *Physical Review B* **46**, 16067 (1992).
36. Frisch, M. J., Trucks, G. W., Schlegel, H. B., *et al.* *Gaussian 16 Revision C.01* Gaussian Inc. Wallingford CT. 2016.
37. Woon, D. E. & Dunning Thom H., J. Calculation of the electron affinities of the second row atoms: Al–Cl. *The Journal of Chemical Physics* **99**, 3730–3737 (1993).
38. Kendall, R. A., Dunning Thom H., J. & Harrison, R. J. Electron affinities of the first-row atoms revisited. Systematic basis sets and wave functions. *The Journal of Chemical Physics* **96**, 6796–6806 (1992).

39. Ferreira, J. Theoretical Study of the Reduction Reaction and Conformational Analysis of Paraquat by Density Functional Theory. *Archives of Chemistry and Chemical Engineering* **3**, 220–230 (2021).
40. Prout, C. & Murray-Rust, P. Crystal and molecular structures of the N,N-dimethyl-4,4 bipyridylium (paraquat) salts with the chlorometallate anions. *Journal of the Chemical Society A: Inorganic, Physical, Theoretical* **0**, 1520–1525 (1969).

7 Concluding Remarks and Outlook

7.1 Conclusion

In this dissertation, a SERS method was developed and successfully applied to identify the pesticides imidacloprid, thiram, and paraquat. This work demonstrates the feasibility of using SERS for on-site pesticide identification with handheld Raman spectrometers, providing a rapid and cost-effective alternative to traditional laboratory-based techniques. In a first approach, the method was developed to detect imidacloprid on-site. For development of the method, Raman and SERS spectra were analyzed, leading to a hypothesis about the arrangement of imidacloprid on the surface. Imidacloprid likely orients its nitro group and pyridine ring towards the gold surface. Furthermore, a charge-transfer complex appears to be formed based on various band shifts. Moreover, a method using gold nanoparticles and different agglomeration agents was developed. Hydrochloric acid and various saline solutions were tested, with hydrochloric acid providing the best aggregation for SERS experiments. The LOD for detection with gold nanoparticles and hydrochloric acid was 30 $\mu\text{g/L}$. This method enables the direct detection of imidacloprid in the field using a handheld Raman spectrometer. Additionally, different solid supports were tested. The potential materials for SERS substrate supports are filter paper and PLA, which were evaluated. Its hydrophobic effect determined that PLA could concentrate the analyte on the spot, which led to better enhancement and lower detection limits than filter paper support, where the analyte interacted differently with the filter paper material. An LOD of 3 ng was determined for the SERS substrate made from PLA. Thus, textile fibers are more effective as a textile support than filter paper. Model calculations suggest a potential residue pesticide concentration of approximately $\sim 300 \mu\text{g/kg}$ in agricultural soil samples. This method has demonstrated that detection is feasible under real-world conditions.

PLA textile was compared with the textile support PET/PA. The gold nanoparticles were first characterized by size and distribution for an accurate comparison. TEM measurements revealed that the synthesized gold nanoparticles have a diameter of 39.60 nm after purification, with a polydispersion of 5.52 nm. The concentration of the nanoparticles was estimated to be 8.04×10^{11} particles/mL. Both textiles were prepared with varying amounts of nanoparticles and different numbers of textile layers. As a result, the best SERS spectra were recorded on both textiles using the highest concentration of nanoparticles at 8.04×10^{11} particles/mL. For the PLA substrate, a double-layer pressed substrate showed the best enhancement. For PET/PA, the single-layer substrate performed best. The PET/PA substrates with a double-layer showed the same quality spectra but no improvement over the single-layer substrate. Considering environmental and resource efficiency, the single-layer substrate was favored.

Inter- and intra-substrate reproducibility were also investigated. PLA with its double-layer pressed substrate yielded a relative standard deviation of 7.5 % for intra-substrate reproducibility and 23.35 %

for inter-substrate reproducibility. For PET/PA, the single-layer substrate had a relative standard deviation of 6.5 % for intra-substrate reproducibility and 14.7 % for inter-substrate reproducibility.

The method developed for imidacloprid was then extended for thiram and paraquat. Thiram and paraquat were also tested on both SERS substrates to extend the method to various analyses. The limits of detection were used for evaluation. Imidacloprid had a LOD of 3 ng for PLA and 600 pg for PET/PA. Thiram had an LOD of 3 ng and 1,100 pg, and paraquat had an LOD of 2 ng and 960 pg, respectively. Tests were also conducted with all three pesticides on model samples, with lettuce leaves chosen as the model. All pesticides could be detected on the lettuce leaves with a good signal-to-noise ratio.

The method was expanded to include silver as precious metal nanoparticles, using thiram and paraquat pesticides. Initially, different SERS spectra were recorded. The conformers of the individual structures were examined with the help of computational chemistry to enable a detailed vibrational assignment. Twelve conformers were identified for thiram and three for paraquat. The geometry of the most energetically favorable and stable conformers was optimized, and their Raman spectra were predicted using quantum chemical calculations. The individual vibrational modes were determined based on these calculations. By comparing the vibrational modes with the experimentally recorded spectra, assumptions about the orientation of the molecules on the nanoparticles were made. It was found that thiram interacts similarly with both gold and silver nanoparticles, with the disulfide bridge splitting so the molecular parts can bind to the nanoparticles via the sulfur atoms. For paraquat, slight differences were observed in the SERS spectra when using gold versus silver nanoparticles, suggesting different orientations on each type of nanoparticle.

Model simulations were performed for the SERS experiments to investigate the paraquat arrangement further. Molecular dynamics calculations on a gold cluster showed that paraquat maintains an approximate distance of 3.4 Å from the surface. This value is in agreement with the distances derived from DFT calculations, which averaged 3.62 Å. A head-on geometry between the nanoparticle cluster and the paraquat molecule was observed to lead to a significant shift in the internal charge, as the dihedral angle of the two ring systems changes drastically from the ground state structure. Specifically, the dihedral angle in the most energetically favorable structure is 36.77°, which changes to 21.79° in a head-on orientation. However, if the paraquat molecule is oriented parallel to the gold cluster, the dihedral angle changes only slightly to 34.29°. This suggests that the head-on geometry leads to an electronic interaction between the gold cluster and the paraquat molecule, possibly forming a charge transfer complex. This would typically result in a significant change in the SERS spectrum compared to the Raman spectrum, but this was not observed. Therefore, the parallel orientation is likely, as the Raman and SERS spectra show apparent similarities. Due to this orientation, there are minimal or no differences between the free paraquat molecule in the Raman measurements and the paraquat molecule oriented at the gold cluster in the SERS measurements.

In conclusion, this research has contributed significantly to the field of pesticide detection by providing a robust and flexible SERS method that can be applied under real-world conditions. The LODs of the method for the individual pesticides were significantly lower than the pesticide residues in the soil commonly found in agriculture, as a model calculation showed. It was also possible to make assumptions about the three pesticides as to how they could be arranged on the nanoparticles. The method's sensitivity, portability, and ease of use makes it to a valuable tool for environmental monitoring and agricultural safety. By demonstrating its applicability to multiple pesticides and sub-

strates, this work lays the foundation for further development and optimization of SERS technologies for on-site chemical analysis.

7.2 Outlook

Future research based on this thesis could explore several areas. One area is optimizing the developed SERS substrates to improve their enhancement factors, detection limits, and quantification limits. This improvement could be achieved by creating more uniform substrate structures. Laser ablation or metal evaporation can be used, etching or other structures as templates.

Additionally, nanoparticles with more complex shapes, such as nanostars instead of nanospheres, could be considered. Research could also focus on achieving more uniform hot-spot formation on the substrates. A research field could also be about the optimal distance for enhancing hot spots or the best agglomeration agent concentration. Another possibility is the use of hybrid nanoparticles. Combining different precious metals and coating processes could enhance the method's sensitivity and selectivity.

Another potential research direction is extending the developed method to detect other pesticides, which would increase the method's versatility. This method can also detect other important environmental structures, such as pharmaceuticals. Further work could also enhance the robustness and user-friendliness of the method for direct application in field trials.

Numerical simulations could be conducted with nanoclusters and pesticide molecules regarding quantum chemical investigations. For instance, the orientation of paraquat on a silver cluster could be studied. The calculations could also take into account electromagnetic enhancement. Computational chemistry combined with machine learning opens the opportunity to do molecular dynamics calculations much faster. With this method, more orientations on different materials for the nanocluster may be investigated because it is drastically more efficient than classical molecular dynamics calculations.

Databases and machine learning could also be employed to create a comprehensive database that can be expanded to include various classes of substances in environmental analysis, such as pharmaceuticals. Machine learning could then quickly and automatically evaluate these spectra. Neural networks can also uncover connections and relations between different SERS spectra in complex matrices.

Additionally, the method could be expanded into a multi-residue approach, allowing for the simultaneous detection and analysis of several different pesticides or environmentally relevant substances in a single measurement. Machine learning and neural networks can even be integrated to extract more relevant information from the spectra and enable the detection of several different substances in complex matrices side by side.

The substrates' environmental compatibility and degradability could be investigated. Integration into automated monitoring systems is also an option. It is conceivable to use integrated systems like robots or drones that autonomously take samples and analyze them using the developed method.

List of Peer-Reviewed Publications

1. **A. Hermsen**, F. Hertel, D. Wilbert, C. Mayer & M. Jaeger. MD and DFT calculations to analyze Raman and SERS spectra of paraquat - from computer aided spectra interpretation to pesticide identification. In Print. 2024.
2. Feng, H., Linders, J., Cantore, M., Fabrizi, J., Kirsten, A., Myszkowska, S., Hillen, E., Uteschil, F., Buchholz, S., **Hermsen, A.**, Davila Garvin, M., Ferez, K. B., Mayer, C. Cross-linked Triblock Peptide Capsules as Potential Oxygen Carriers. *ChemistryOpen*. 2024. **13** e202300282
3. **A. Hermsen**, F. Hertel, D. Willbert, T. Gronau, C. Mayer & M. Jaeger. Pesticide identification using surface enhanced Raman spectroscopy and Density Functional Theory Calculations: From structural insights to on-site detection. *Applied Spectroscopy*. 2024. x (y): zz.
4. Karakaya, Y., Somnitz, H., **Hermsen, A.**, Gonchikzhapov, M., Kasper, T. Applications in Energy and Combustion Science. Revisiting the initial reaction rates for TMS combustion and a new evidence for metastable silica nanoparticles in the gas-phase synthesis. 2023. **14** 100152
5. Schmiemann, D., Hohenschon, L., Bartels, I., **Hermsen, A.**, Bachmann, F., Cordes, A., Jaeger, M., Gutmann, J. S. & Hoffmann-Jacobsen, K. Enzymatic post-treatment of ozonation: laccase-mediated removal of the by-products of acetaminophen ozonation.. *Environmental Science and Pollution Research*. 2023. **30** 53128-53139
6. **Hermsen, A.**, Schoettl, J., Hertel, F., Cerullo, M., Schlueter, A., Lehmann, C., Mayer, C. & Jaeger, M. Green Textile Materials for Surface Enhanced Raman Spectroscopy Identification of Pesticides Using a Raman Handheld Spectrometer for In-Field Detection. *Applied Spectroscopy*. 2022. **76** 1222-1233
7. Hermes, P., **Hermsen, A.**, Jaeger, M., Gutmann, J. S. & Strehmel, B. Challenges and limits of upconversion nanoparticles for cationic photopolymerization with UV initiators excited at 980 nm. *Polymer Chemistry* 2022 **13** 4879-4886
8. **Hermsen, A.**, Lamers, D., Schoettl, J., Mayer, C. & Jaeger, M. In-Field Detection Method for Imidacloprid by Surface Enhanced Raman Spectroscopy. *Toxicological and Environmental Chemistry* 2021 **104** 36-54

Curriculum Vitae

Der Lebenslauf ist in der Online-Version aus Gründen des Datenschutzes nicht enthalten.

Affidavit of Affirmation

Andrea Hermsen

wohnhaft in: in der Online-Version aus Gründen des Datenschutzes nicht enthalten.

Ehrenwörtliche Erklärung zu meiner Dissertation mit dem Titel:

Towards pesticide identification in open fields by Surface-enhanced Raman spectroscopy: A preparative, spectroscopic, and quantum chemical route

Hiermit erkläre ich, dass ich die beigefügte Dissertation selbstständig verfasst und keine anderen als die angegebenen Hilfsmittel genutzt habe. Alle wörtlich oder inhaltlich übernommenen Stellen habe ich als solche gekennzeichnet.

Ich versichere außerdem, dass ich die beigefügte Dissertation nur in diesem und keinem anderen Promotionsverfahren eingereicht habe und, dass diesem Promotionsverfahren keine endgültig gescheiterten Promotionsverfahren vorausgegangen sind.

Ort, Datum

Unterschrift (A. Hermsen)

Acknowledgements

I would like to take this opportunity to thank everyone who has supported and motivated me on this journey.

First of all, I would like to express my gratitude to Prof. Dr. Martin Jäger, my supervisor. I thank him for his excellent support and the many constructive discussions. The lively discussions have contributed significantly to the success of this thesis. I had plenty of room for my own research ideas and the opportunity to implement them at any time during my PhD.

I would also like to thank Prof. Dr. Christian Mayer for his supervision. I was always very welcome in his working group in Essen. I also have to thank the members of the working groups in Krefeld and Essen, especially Dr. Jürgen Linders and Dr. Maria Davila Garvin. They both have always supported me with tips and ideas.

Furthermore, I want to acknowledge my co-authors (The Boys)! I thank David Lamers, Justus Schöttl, Dominik Wilbert and Florian Hertel for their support with the SERS experiments. Till Gronau and Raphael Schaffarzyk have to be thanked for their support with the quantum chemistry simulations. The support of the boys also contributed significantly to the success of this work. Thank you, for many enjoyable hours in the laboratory and office, as well as the activities outside university. It was a pleasure working with you, you are awesome!

In addition, Dr. Gerrit Renner and Dr. Amir Hossein Omranpoor also actively supported me with their ideas. I would like to thank Dr. Gerrit Renner for the endless hours he took to help me get started with programming. There was no single question he could not help me with. Thank you to Dr. Amir Hossein Omranpoor for the information and constructive discussions about the simulations.

Thank you to Heinz Sprünken for providing the IT resources and for always taking care of my technical problems and questions – even when he was quite busy. Also thanks for his infinite patience with my questions.

I would also like to thank my friends and family. I have always received support and motivation from my friends.

Thank you very much for all that support!